UCLouvain

École polytechnique de Louvain

Technical challenges linked to the grid dynamics in the context of energy islands

Author: **Baptiste Laterre**
Supervisor: **Emmannuel De Jaeger**
Readers: **Virginie Kluyskens, Bruno Dehez**
Academic year 2023–2024
Master [120] in Electrical Engineering

Abstract

In the context of the development of energy islands that harvest the power produced by wind farms, a hybrid link was introduced in the second modular offshore grid designed by the Belgian transmission system operator *Elia*. This hybrid link refers to the parallel use of an AC and a DC transmission link. Regarding the power flow, this link raises questions associated to the active power losses and to the reactive power generated by offshore cables.

This thesis addresses the design of an active power dispatch controller with the goal of minimizing active power losses, and covers the development of reactive power compensators through the use of shunt reactors, so as to mitigate the effects of a reactive power imbalance (namely the rise of the cable voltage and the increase of the active power losses). In a wider scope, this work deals with the reasons behind the existence of limits of cable length and it assesses the robustness of the future second modular offshore grid.

The outcome of this work demonstrated that the DC part of the hybrid link should be preferred to the AC one so as to minimize active power losses. Regarding the shunt reactors, it has been shown that an equal compensation at both cable ends provides the best results in terms of voltage and current increase. The limitation in cable length has been explained via the active power losses, rising along with the distance of transmission. Finally, from the robustness point of view, it has been shown that the future grid could not ensure a zero power outage in case of some particular faults.

Acknowledgements

In these few lines, I want to express my gratitude and to extend my warmest thanks to every single person that helped me to carry out this month-long work.

To my Supervisor, Professor Emmanuel De Jaeger, for sharing with me his interests in topics related to electrical systems, and for allowing me to achieve this master thesis. Thanks for his helpful and priceless advice, his enthusiasm and his reliability.

To my first Reader, Virginie Kluyskens, and to Guy Wanlongo Ndiwulu, for their availability, their precious assistance and their support. Thanks for their patience, their motivation and their determination during our meetings. A special thanks to Guy for taking the time to troubleshoot my simulations.

To my second Reader, Professor Bruno Dehez, for agreeing to review this work and for joining Pr. De Jaeger and Mrs. Kluyskens in my final jury. Also, thanks for having developed my interest and my curiosity in electromechanical converters.

To Quentin Delhaye, for his readiness to answer my questions, for his benevolence during our discussions and for his relevant comments.

To my parents, for allowing me to pursue these wonderful studies, for their support and comfort throughout.

To my brother for his help and time, to my sister, to my friends and my roommates.

Contents

List of Figures

List of Tables

List of Symbols

AC Alternative Current

DC Direct Current

DFIG Doubly-Fed Induction Generator

HVDC High-Voltage Direct Current

IGBT Insulated-Gate Bipolar Transistor

LCC Line-Commutated Converter

MMC Modular Multilevel Converter

MOG Modular Offshore Grid

PI Proportional-Integral

PLL Phase-Locked Loop

PMSG Permanent Magnet Synchronous Generator

SCR Short-Circuit Ratio

TSO Transmission System Operator

VSC Voltage Source Converter

Chapter 1

Introduction

Our century is subject to plenty of paradigm shifts. Amongst one of them is the energy transition, with the aim of converting a part of our energy needs into low-emission electrical energy. This transition is the outcome of various political plans. Two important ones are the 2015 *Paris Agreement* that seeks to limit the rise of the world mean temperature bellow $+2°C$ before pre-industrial era [1], and the 2020 *European Green Deal*, a set of policy initiatives whose target is to reach net zero emissions of greenhouse gases by 2050 [2].

This energy transition leads to various challenges: instead of fitting the production to the demand, the need of demand-side management will be developed in function of the renewable electricity production. Grid operators need to reinforce their network and re-think it as a meshed grid, with multi-directional loadflows to replace the existing vertical, uni-directional loadflow, for a better renewable electricity penetration. To cope with these challenges, new technologies are used, such as power electronics with High-Voltage Direct Current (HVDC) transmission lines, allowing for more flexibility and control in the electricity transmission field, and more energy trading between countries.

In the context of the development of a new $3.5GW$ offshore wind farm, the Belgian Transmission System Operator (TSO) *Elia* elaborated a second Modular Offshore Grid (MOG II), in parallel with the existing one, the MOG I. This new offshore grid includes an energy hub (or energy island) that has AC and DC transmission capabilities: the situation is depicted in Figure 1.1. Located $45km$ away from the Belgian coast, this island is called “Princess Elisabeth Island”, after the Princess Elisabeth Zone in which it will be built. The use of AC/DC power converters should make it possible to exchange power between the United Kingdom ($1.4GW$), Denmark ($2GW$) and Belgium (2x$2GW$), via HVDC transmission links. Along with DC connection capabilities, 6 AC transmission links connect the energy island to Belgium, with a total rated power of $2.1GW$ [3].

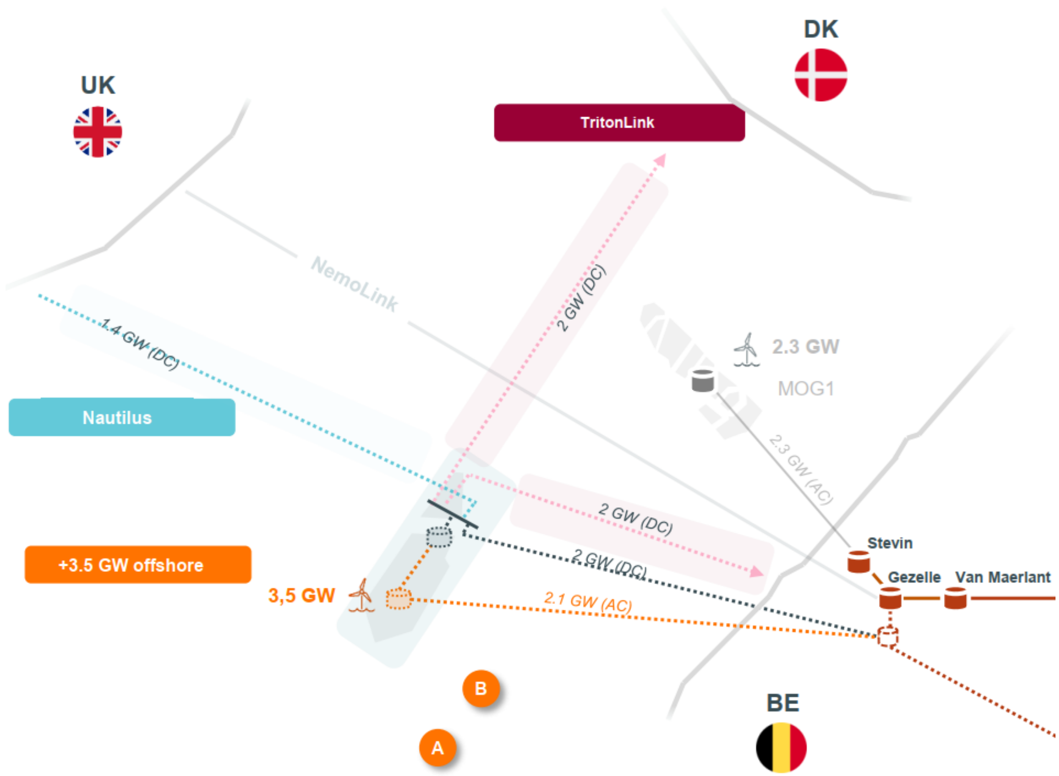

Figure 1.1: Illustration of the Princess Elisabeth Island project with the existing infrastructure (in grey). Reproduced from [3].

This future system can be studied from different perspectives: power quality and stability (frequency, voltage, congestion, harmonics), interactions with the Belgian grid, utility as ancillary services (power exchange between energy islands, hydrogen production, ...) or even social, economic and environmental impacts of the project (price of electricity, energy production outlooks, direct environmental impact on the sea wildlife, Life Cycle Analysis, ...). In the scope of this work, a first study on the power loadflow is carried out: the goal is to analyze the way the power produced by the wind farm is sent to the onshore electrical grid and to raise challenges linked to this new offshore grid.

1.1 Research Question, Objectives and Challenges

The central research question of this master thesis is to study the way the power produced by the wind farm is brought back on the Belgian onshore grid. In this work, the main element of interest of the offshore grid is referred to as “hybrid interconnection”, which is the parallel use of AC and DC cable links between the same start and end points.

Knowing that the DC power of the hybrid link is controllable, one objective is to know the part of the produced power that should flow in the DC link so as to minimize active losses caused by the hybrid link. This objective is translated into the development of an external active power dispatch controller, acting on AC/DC power converters. In a wider scope, the benefits and drawbacks of using a hybrid interconnector are also studied.

Another challenge brought by this offshore grid is the use of submarine cables. Compared to overhead lines, they present a high capacitive effect, which influences two quantities: it affects the reactive power measured at cable ends and it limits the maximum AC active power transmissible by a cable. This limitation is analyzed and quantified, and a solution is brought to the reactive power issue, via the use of shunt inductors as reactive power compensators. An analytical model is used to design the shunt reactors: their positive impacts on the MOG II are assessed through the simulation of this analytical model.

One last objective linked to the power flow in this system is the robustness assessment, with the aim of approving or rejecting a criterion based on the acceptable number of unavailable elements in the offshore grid, due to faults or maintenances, without disturbing or reducing the total power flow.

1.2 Main Contributions

Analysis of active power losses on the hybrid link shows that the DC link should be loaded in priority to the AC one: considering the same active power exported, AC power losses are more than ten times higher than the DC ones. Therefore, the dispatch controller aims to detect variations of generated power and load the DC link accordingly, up to its rated power.

The maximum active power transmissible on an AC cable is explained by the rise of the active power losses, caused both by the rise of the cable resistance and by the increase of the line current magnitude. The latter is caused by the capacitive effect of the cable.

After the shunt reactors have been tested in three different scenarios, the best results are obtained by an equal repartition of the reactive power to be compensated at both onshore and offshore busbars: this configuration provides an effective tradeoff between the need of keeping the line current below the rated one, and the rise of the offshore busbar voltage.

Regarding the robustness of the offshore grid, the criterion could not be fulfilled, due to important overloads on transformers and to power outages under fault conditions on DC elements of the network.

1.3 Methodology

The procedure applied to answer questions and to fulfill objectives mentioned in Section 1.1 starts with an overview and with comparisons of existing AC and DC transmission system technologies. After choosing specific technologies, AC and DC elements of the studied grid are modeled, considering steady state phenomenons. These elements can be cables, AC/DC power converters or an aggregated model of a wind farm. Control strategies of power converters are also discussed.

After the system model is developed, an analysis on the maximum active power transferable in an AC cable is carried out, along with the quantification of active power losses. The latter leads to the development of an active power dispatch controller, integrated into the global controller strategy. Simulations of the global model are then carried out to confirm that the dispatch controller strategy is valid.

To achieve this work, a significant part of information is extracted either from earlier publications (articles, thesis, books), from websites or from technical brochures: whether it is a concept, an idea, a picture or numbers that were not found, realized or obtained by the author, a bibliographical reference is placed as close as possible to the item.

Simulations are performed by either of the two softwares: *DIgSILENT PowerFactory* or *MATLAB Simulink*. *DIgSILENT PowerFactory* allows to use models of elements of a grid, and to achieve various types of simulations (Loadflows, Root-Mean-Square (RMS), Electro-Magnetic Transients (EMT), ...) on a designed grid. In this work, only a loadflow study is achieved. Also, the *MATLAB Simulink* software is used to simulate transfer functions that use the *Laplace* variable.

This work is carried out in English. Some words, sentences or parts of them may have been translated or rephrased by two online tools: *DeepL* or *QuillBot*.

The use of *ChatGPT* is, in any case, not used to find technical ideas, data or piece of information.

1.4 Thesis Structure

The structure of this document matches the methodology chosen to answer the central and subsidiary research questions.

This first chapter is an introduction to the research question and to the context in which it emerged. It also features the methodology applied throughout this work and its final contribution.

Chapter 2, entitled "State Of The Art" is an overview of existing AC and DC transmission system technologies. It allows to compare them and justify the chosen technologies for the electrical grid to be studied. Also, a simplified wind turbine model is analyzed.

Chapter 3 is dedicated to the analytical modeling and the theoretical analysis of the electrical grid. It contains models for the AC and DC transmission systems and for the wind farm. These models are then used to assess the grid robustness, to develop the active power dispatch controller that minimizes active power losses, and to design shunt reactors, used to mitigate the reactive power produced by cables.

The fourth chapter aims to validate analysis and models made in the previous chapter. The effect of the shunt reactors and the accuracy of the steady-state wind turbine model are evaluated, through the simulation of these models. Also, the control strategy of the dispatch controller is assessed.

Finally, Chapter 5 summarizes this work, starting from the research questions to the results obtained. Contributions taken out of these results are also outlined and future perspectives of work are suggested.

Chapter 2

State Of The Art

In this chapter, a review of existing AC and DC technologies in the field of power transmission is made, with a development of their specifications, advantages and disadvantages. It allows to compare these technologies and to justify technical choices made for the new Modular Offshore Grid (MOG II). Also, a simplified wind turbine model is introduced to model generation units in this grid.

Section 2.1 compares the benefits and the limitations of AC and DC transmission links. HVDC systems differ in two main aspects: the distance between terminals and the terminal topology. Based on these criteria, a classification of the different HVDC systems is presented in Section 2.2. Also, two types of power converter exist to turn AC into DC or vice-versa: Section 2.3 develops their respective abilities and drawbacks. Section 2.4 lists the interests of using a hybrid AC and DC link and motivates the reason why *Elia* plans to use such a link in its future offshore grid. Last, Section 2.5 presents a simplified steady-state model of wind turbines, valid for two specific types of wind turbines.

2.1 Comparison of AC and DC Transmission Links

Back in the late 1880s, the choice between AC and DC for electric power transmission was already discussed: George Westinghouse and Thomas Edison fought to impose respectively AC or DC transmission systems to supply their lightning equipment. At that time, DC voltages could not be easily increased or decreased, as an AC transformer would do. The outcome of the war of currents is well-known: AC equipment was preferred to DC one, such that AC transmission grids are now spread all over the world [4]. But recently, DC systems made their come back in the field of transmission links: new technical challenges related to the distance of transmission made DC more interesting than AC for several reasons developed here below [5–8].

Two main factors are used to compare AC and DC transmission links: the maximum active power transmissible on a link (influenced by active power losses and reactive power) and the initial cost of the system.

In AC links, the maximum active power transmissible is affected by two effects: the skin effect and the capacitive effect. These two factors are developed in Section 3.1.2. The skin effect is related to the repartition of currents at the surface of a conductor: due to the alternating magnetic field generated by the AC current flowing in the link, Eddy currents are induced. These currents are in opposite direction to the main current, which cancels a part of it (see Figure 2.1).This effect mainly occurs at the center of the conductor, which results in an effective cross-section (called "skin depth" and written δ) smaller than the physical line or cable cross-section (as depicted in Figure 2.2), leading to a greater resistance than the one due to the conductor resistance, thus leading to greater Joule losses. The longer the line, the greater the resistance, the greater the active power losses.

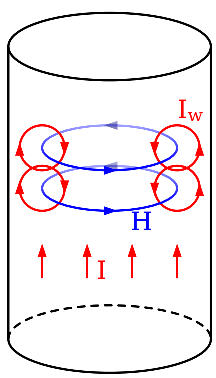

Figure 2.1: Illustration of the skin effect in a conductor. I is the main AC current, H is the magnetic field caused by the flow of current I and I_W is the Eddy current induced. Reproduced from [9].

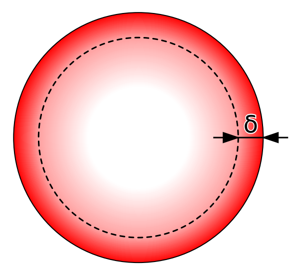

Figure 2.2: Illustration of the skin depth δ, *i.e.* the effective cross-section resulting from the skin effect. Reproduced from [9].

The second effect that reduces the maximum active power on a link is the capacitive effect of the line. It is due to the presence of capacitances $C/2$ between the AC terminals and the ground (see Figure 2.3). Due to a higher dielectric permittivity and a smaller distance between the core and the sheath in cables, compared to the dielectric permittivity and the distance between the conductor and the ground in overhead lines, capacitances of cables are greater than the ones of lines. Also, these capacitances increase with the cable length. As a result, since the voltage at one link end increases due to the rise of the line series impedance linked to the resistance R and the inductance

L, the current flowing in the capacitance at that end increases as well. An additional effect that reduces the maximum active power transmissible is the rise of terminal voltages. In order to increase the amount of active power to transfer without increasing the line current, the transmission link voltage is risen. However, a greater voltage generates greater capacitive currents. This results in a greater line current amplitude, resulting in greater Joule losses. Above a certain distance, both skin effect and capacitive currents are so important that all the initial active power is dissipated in heat.

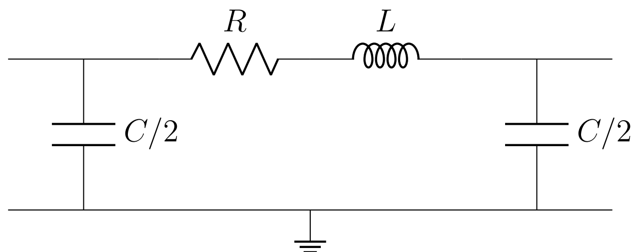

Figure 2.3: Pi-section model for one phase of an AC cable or AC overhead line.

As a result of these losses and limitations, there is an acceptable maximum length of AC cables, depending on the rated power and rated voltage. This length is often around $100km$. In order to enhance the maximum active power and to reduce side-effects caused by the reactive power generation, shunt reactors (or any reactive power compensator) can be placed at line or cable ends to absorb this reactive power. If the link is too long, mid-way reactive power compensators need to be placed. Connecting those compensators might not be an issue for overhead lines and land cables, but it is for offshore cables. Even a simple shunt reactor represents a challenge in terms of technical difficulties and financial costs.

Figure 2.4 illustrates the aforementioned active power limitations: two single-phase AC cable of respective rated voltages $275kV$ and $400kV$ are operated with different repartitions of reactive power compensation at cable ends. For example, the red curve shows the maximum active power that can be transmitted over a $400kV$ single core cable with a reactive power compensation repartition of 100% of the total reactive power to be compensated at one end, and 0% at the other end. Following the aforementioned explanations, the higher the power, the higher the voltage, but the shorter the acceptable cable length, seen the reduction of maximum active power transmissible. This limitation represents a certain cost: active power is generated but only a part of it can be valuable, which represents a financial loss. The positive effect of reactive compensators can also be noticed, relatively to the acceptable cable distance.

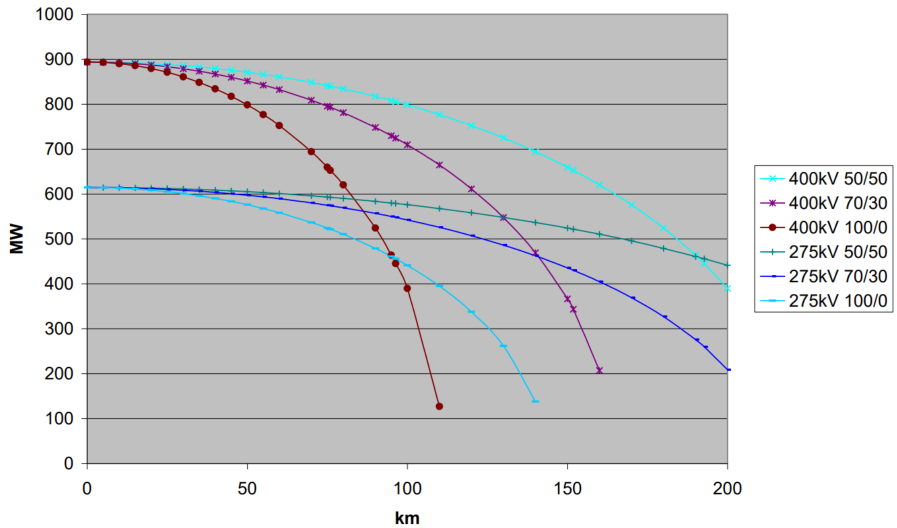

Figure 2.4: Comparison of the maximum active power transmission between $275kV$ and $400kV$ single core AC cables, with different repartitions of reactive power compensation. Reproduced from [8].

In contrast, HVDC links do not suffer from skin effect, nor capacitive currents. Even at high power, high voltage and over long distances, only Joule losses happen on the link: they are due to the resistivity of the conductive material, generating a small voltage drop between line or cable ends, resulting in a small active power loss. Power converters also generate losses but, beyond a certain distance, these converter losses are much smaller than the ones caused by the AC link. For comparison purposes, Figure 2.5 depicts the evolution of the maximum active power transmissible in AC and DC cables relatively to the distance of the link, with various voltage ratings and cable sections. It is clear that DC cables are far more efficient in terms of active power losses at high distance, compared to AC cables.

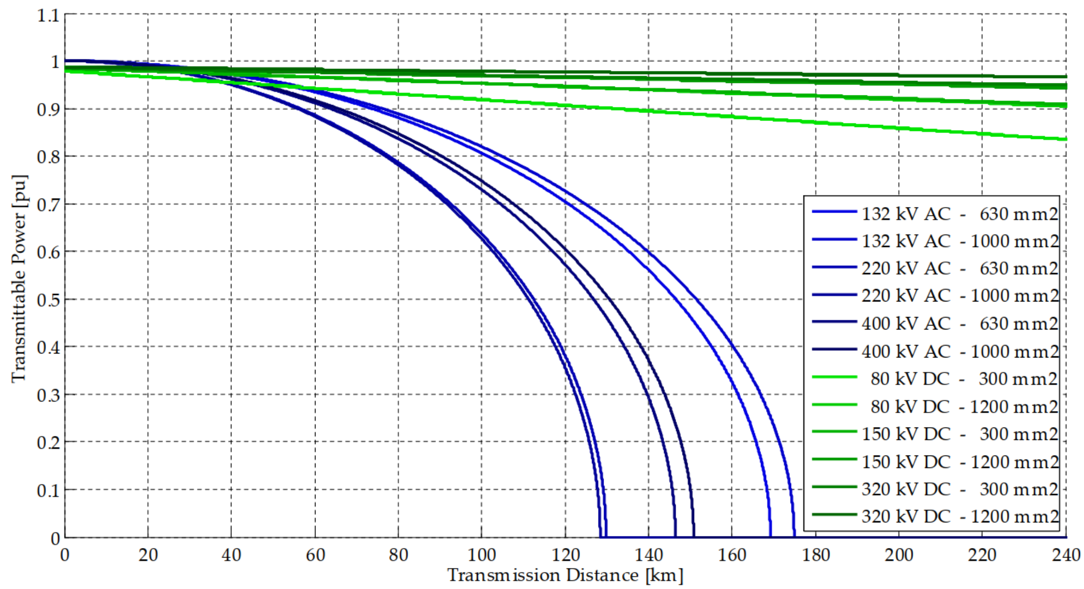

Figure 2.5: Comparison of the maximum active power transmissible for single-phase AC cables and DC cables with different voltage ratings and cable cross-sections. Reproduced from [10]. The observation that the maximum active power transmissible in DC cables is not $1 p.u.$ at zero length could be explained by the fact that converter losses are taken into account.

The second factor of comparison is the initial cost of AC and DC systems. For the same rated power, in the present scenario of the MOG II, the AC equivalent of two HVDC cables is six three-phase cables. However, since HVDC links need expensive converters and other DC-specific equipment, the initial cost of DC links is usually higher than the one of AC links.

Putting the initial cost and the cost of active power losses together, Figure 2.6 is obtained. Although representing the line scenario, the situation is the same for cables. As mentioned, the initial cost of DC links is higher than the one of AC links. Beyond a break-even distance, the cost of AC links overcomes the one of DC links because the maximum active power transmissible in AC decreases more with respect to cable length than in DC. Also, the maintenance cost of DC equipment can be discussed, compared to the AC ones: *Hualei Wang et al.* [11] suggest that AC costs of maintenance are usually greater than DC ones, but this statement is questionable, considering the high maintenance frequency of equipment needed for HVDC systems (arc extinguishing system of breakers, replacement of submodules, ...). For example, *Elia* plans 8 days per year of maintenance for offshore and onshore converters, which represents a logistic challenge and a financial cost, along with the cost linked to the reduced capacity of the DC link during maintenance [12]. Typically, break-even distances in the specific case of offshore cables vary between $50 km$ and $120 km$.

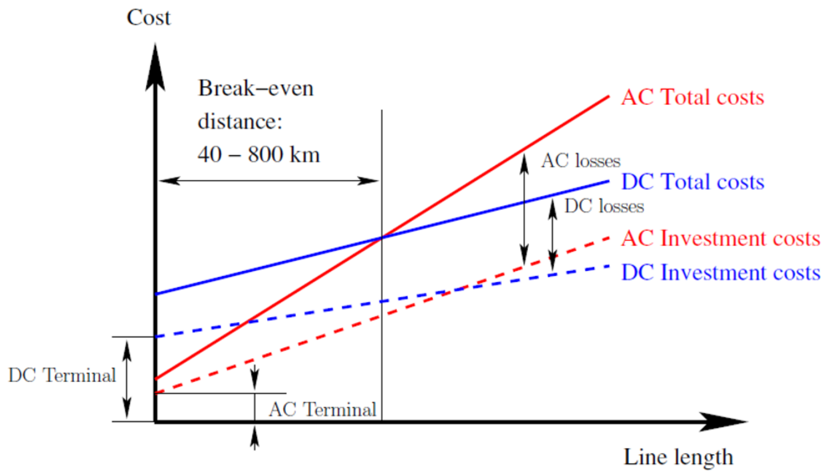

Figure 2.6: Comparison of costs of AC and DC transmission line in function of line length. Reproduced from [5]. The total cost corresponds to both investment costs and the cost of power losses.

Other advantages are granted to HVDC, such as the ability to control the active power transmitted onto it via converters, while AC links are subject to network conditions and a loadflow is established spontaneously.

Concretely, two useful applications of HVDC transmission links are the energy trading between countries or regions (thanks to the active power control offered by converters) and the integration of renewable energy units in the grid, since offshore wind parks are located away from continents. If this distance exceeds the break-even distance, HVDC cables is a better choice than AC to transmit the generated active power.

So, depending on the distance of transmission, DC can be preferred to AC. In the present scenario of the Princess Elisabeth Island, this distance might correspond to the break-even distance, since export cables are $45km$ long: both AC and DC technologies can be legitimately exploited.

2.2 HVDC System Classification

Since AC is the most popular way of electricity production and transmission around the world, a HVDC transmission system is always based on two AC/DC power converters at least, and one (or more) conductor(s). These power converters can be of two types: Line-Commutated Converters (LCC) or Voltage Source Converters (VSC). These two technologies are compared in Section 2.3. Also, different types of converters can be used within the same transmission system, leading to different topologies (*e.g.* terminal-hybrid, pole-hybrid, series converter-hybrid or parallel converter-hybrid [13]).

Considering the same converter technology, HVDC systems can be classified based on two criteria: the distance between terminals and the way these terminals are configured, *i.e.* the terminal topology.

2.2.1 Classification by Distance Criterion

Depending on the distance between terminals, the link is either back-to-back or point-to-point. Back-to-back refers to HVDC links whose purpose is to connect two asynchronous grids (different frequencies or phase angles), separated because of regional limits or to reduce the Short Circuit Ratio (SCR) in case of fault. Practically, it consists of two terminals within a same substation. A real-life application is the 1989 $150MW$ *McNeill HVDC Back-to-Back Converter Station* that connects the two provincial grids of Alberta and Saskatchewan, in Canada [14, 15].

Vice-versa, point-to-point HVDC systems refer to two DC terminals several kilometers away from each other. The goal of such systems is to transmit power over long distances, as discussed in the previous section. One recent interconnexion project is the 2020 *ALEGrO*, the first HVDC transmission link between Belgium and Germany, capable of carrying up to $1GW$ via $90km$ of land cables [16].

Since the Princess Elisabeth Island is located $45km$ away from the Belgian coast, the HVDC system is obviously a point-to-point system.

2.2.2 Classification by Terminal Topology

Three main types of configurations exist [17]. Monopolar transmission (Figure 2.7a) has two conductors, with one pole, positive or negative. In some applications, the second cable may also be replaced by a ground or sea return to avoid installing a metallic return.

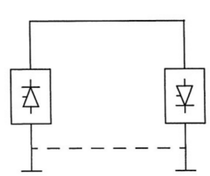
(a) HVDC Monopolar.

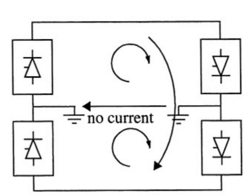

(b) HVDC Bipolar.

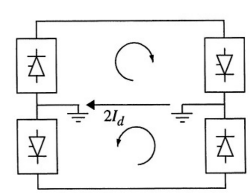

(c) HVDC Homopolar.

Figure 2.7: Types HVDC system topologies using the same power converters. Reproduced from [17].

Bipolar transmission links (Figure 2.7b) refers to the presence of two polarities: one positive and one negative. For this type, two converters in series are needed at each terminal, and the junction is grounded. In normal operation, the same current flows through each pole but in opposite direction, such that no current goes to the ground: the bipolar link acts as two symmetric monopolar links. It can also be operated as two asymmetric monopolar links, when two different active powers flow through the two converters in series. This could happen voluntarily, to carry out a maintenance on a converter or a cable, or as a consequence of a fault, limiting the available power per terminal. In that case, as a result to a difference in current magnitude in the two polarities, current must flow through the ground: to this end, a metallic return cable is sometimes added.

Homopolar transmission, depicted in Figure 2.7c, means that both poles have the same polarity. This type also requires two converters per terminal, in opposite-series, with a grounded junction. To close the circuit, either a line or cable return can be installed, or a ground return can be used. This type is not often used in real-life applications, due to the complexity of using a ground return carrying twice the rated current.

The choice between monopolar and bipolar topologies depends on the desired specifications of a project. Some of these specifications are [18]:

– Cost: bipolar configuration has twice more converters and possibly an additional return cable compared to monopolar that uses two converters and one or two cables. Also, voltage ratings of cables are higher for a bipolar configuration, which increases the total cost of the system. Bipolar is therefore more expensive than monopolar.

– Transmission capacity: thanks to the doubled apparent voltage for the same rated current, a bipolar terminal can transmit twice the rated power of a monopolar terminal.

– Robustness: bipolar presents redundancy, even more if a metallic return is available. If a fault occurs on a converter or a line, this topology is more robust than the monopolar one: the latter would ineluctably experience a complete power outage. This is known as the $N-1$ criterion, discussed in Section 3.4.

– Environmental impact: it is considered as being caused by the number of cables to install and the earth currents between terminals. The monopolar topology has low impact if only one cable is needed, but it has a great one because of the ground return current that disturbs soil or sea wildlife. Bipolar, on the other end, might have a bigger impact caused by the installation and the presence of two or three cables, but has very low earth currents thanks to the metallic return.

Beyond the total cost of the HVDC system, the bipolar configuration offers much more advantages than the monopolar one: this is the reason why that topology is used more and more in projects carried out in recent years, at the expense of the monopolar topology. In the specific case of the Princess Elisabeth Island, a bipolar topology is chosen, and a third metallic return is planned so as to increase the robustness of the HVDC transmission link.

2.3 AC/DC Power Converters

In the history of discoveries in power electronics, AC/DC converters might be the most revolutionary one, given their various utility. Typical applications are the generation of specific AC voltages (control of the position or the speed of electromechanical converters for robots, trains, industrial machines, ...), the rectification of AC into DC (to power large DC loads such as electrolyzers, to charge battery banks, ...) or the connection of two asynchronous AC grids (via back-to-back converters, as mentioned earlier).

Two technologies of AC/DC power converters have been co-existing these last two decades: Line-Commutated Converters (LCC) and Voltage Source Converters (VSC). Although they achieve the same task, in practice, they behave in an antagonistic way.

LCC aims to keep the DC-side current as constant as possible, with a series smooth inductance on the DC side. Its elementary component is the thyristor, a controllable diode: once a threshold voltage is reached, if the gate is triggered, the diode drives current and keeps on conducting it as long as the voltage switches of polarity. Formerly, mercury-arc valves were used, instead of thyristors: the last large-scale equipment using them was shut down in 2012 [19]. Up to now, the theoretical maximum power that a LCC installation can transmit is $10GW$. [19]. Figure 2.8 depicts a typical LCC, in an inverter configuration.

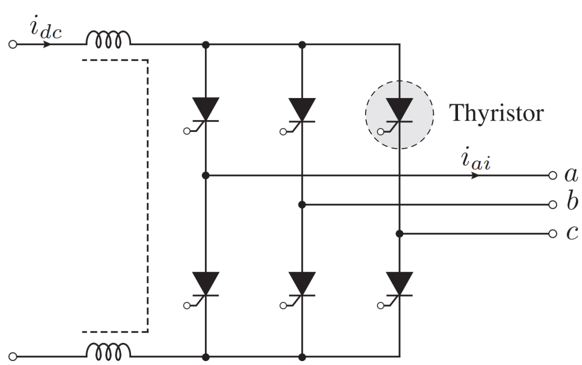

Figure 2.8: Three-phase Line-Commutated Converter. Reproduced from [20].

A real-life application making use of LCCs is the 2018 *Western HVDC Bipolar Link*, carrying a rated power of $2.25GW$ under $\pm 600kV$, on $400km$ of offshore cable between Western Scotland and North Wales. Today (2024), this HVDC link is considered as the most powerful in Europe, but LCC-based installations in China can have rated powers of $7GW$ or more [21].

VSC appeared in the late 1990s: the first one was able to carry $3MW$ under $\pm 10kV$[18]. Until the 2010s, LCC technologies dethroned VSC because of power limitations: at that time, VSC could carry no more than $500MW$ while LCC could withstand several gigawatts. Since then, technological advances have increased the VSC rated power up to $1GW$. Although this remains lower than the one of LCC, VSC is often preferred to LCC for its attractive technical capabilities, mentioned later in this section [22].

In contrast to LCC, VSC keeps the DC voltage as constant as possible with the help of a parallel smooth capacitance. The elementary component is the Insulated-Gate Bipolar Transistor (IGBT): while the control of a thyristor is limited to specific conditions, the IGBT valve can be selected as being conductive or non-conductive at any time, with no restriction [23]. According to desired performances, a VSC has different topologies. Two knowns are the two-level or three-level, in reference to their number of reachable AC voltage levels: the higher, the closer to a sine wave. Figure 2.9 illustrates a two-level VSC.

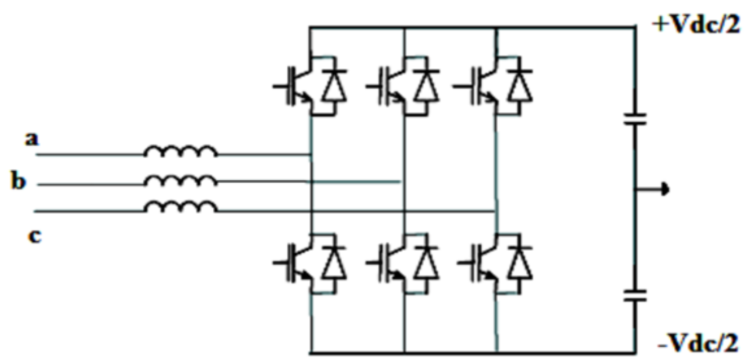

Figure 2.9: Three-phase two-level Voltage Source Converter. Reproduced from [24].

Recently, a new type of VSC emerged: the Modular Multilevel Converter (MMC). It consists of submodules, composed of IGBTs and a capacitance as energy reservoir, placed along three upper and three lower arms, as shown in Figure 2.10. Besides the great sine wave built (better for harmonic content), signals that triggers those submodules have a reduced frequency than those of two or three level VSC, which results in less power losses in the converter. Also, thanks to the large number of individually controllable capacitances, new control strategies including these energy buffers are studied (*e.g.* a dual-port grid forming MMC [25]).

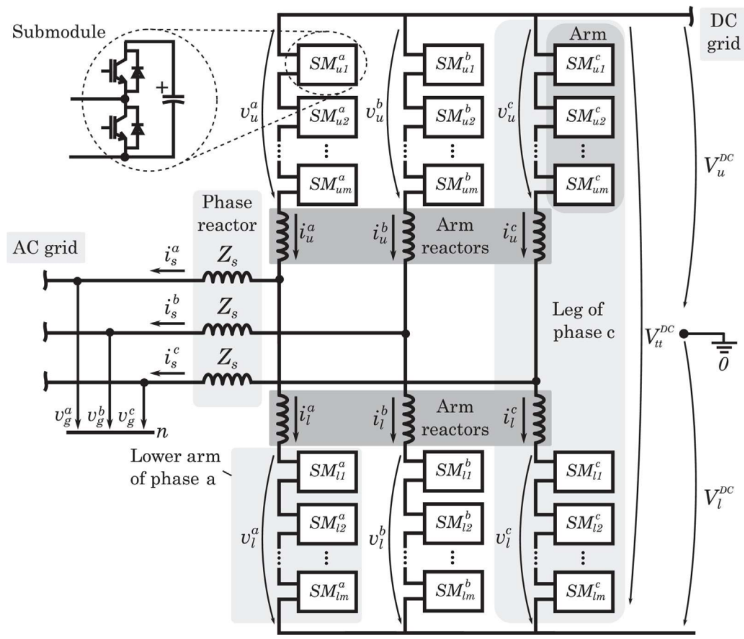

Figure 2.10: Three-phase Modular Multilevel Converter with half-bridge submodules. Reproduced from [25].

A great application of the VSC is the 2015 *INELFE* HVDC link, connecting France and Spain through $65km$ of land cable under $\pm 320kV$. Four VSCs are used: they are all of MMC type that uses half-bridge topology, and are operated as a bipolar transmission link (or two symmetrical monopolar links). It is the world's most powerful MMC-based HVDC system: the transported power capability reaches 2x1GW [26, 27].

In Belgium, the 2019 *Nemo Link* connects *Elia*'s grid to the United Kingdom via $130km$ of subsea cables. VSCs are also MMC type. The HVDC link, operating at $\pm 400kV$, is able to exchange up to $1GW$ between each country [28].

As mentioned, LCCs and VSCs are different technologies, offering advantages but presenting drawbacks [18]:

- Grid requirements: LCCs require a strong grid (Short Circuit Ratio (SCR)>3). Otherwise, voltage instability, commutation failure and a limited power transfer might occur. On the other hand, VSCs have no SCR requirements: they can operate in weak AC systems. Also, VSCs are able to modulate AC voltages in magnitude and frequency (grid former), while LCCs cannot and need a formed grid (voltage magnitude and frequency) to rely on, on both sides, to be able to work.

- Voltage range: DC voltage is limited to $\pm 600kV$ per VSC and can go beyond $\pm 1000kV$ per LCC.

– Voltage control: a VSC can specify either AC or DC voltage, whereas a LCC can only control DC voltage.

– Active power range: up to $1GW$ per VSC, and up to $2GW$ for a bipolar link. LCCs can handle up to $10GW$ per bipolar link, but present a minimum active power transmission: as the firing angle that triggers gates cannot be lower than a defined angle, a minimum active power is always transmitted. VSCs are not affected by this limitation.

– Active power control: a VSC offers a fast control of active power that can be achieved in both directions, since only the current needs to reverse direction. A LCC can also specify the active power at its terminals through DC voltage control. The power flow can thus be reversed by inverting the voltage polarity, but this operation cannot be instantaneous.

– Reactive power control: LCCs have no reactive power control at all. VSCs can either generate or absorb it.

– Reactive power: LCCs spontaneously consume reactive power and need capacitor banks to compensate it. VSCs do not need any compensators as they can generate or consume reactive power.

– Harmonics: LCCs generate voltages with high harmonic content: big filter banks are required. VSCs, above all with MCCs, reduce the harmonic rejection to a point where filters can even be unnecessary.

– Black start capabilities: since a LCC needs to rely on a formed grid and cannot control the magnitude and frequency of its output voltage, it has no black start capabilities. On the other hand, a VSC is able to rebuilt a grid from scratch.

– Losses: at $1GW$ rated power, they vary between 0.5% and 1% for a LCC and between 0.9% and 1.75% for a VSC.

– Commutation failures: if a sudden voltage drop of magnitude or a change of phase occurs, LCCs might experience commutation failures. As the expected AC voltage is not the same as the available one (due to the voltage drop or phase shift), active power can drop to 0 for a short time, and DC current can quickly rise to very high values during a short amount of time: this is caused by the fact that a thyristor stays conductive as long as its voltage stays above its respective threshold, and cannot be turned off. Since a VSC can be turned on and off at any time, voltage dips and phase changes are not an issue: a VSC does not present commutation failures.

– Short circuits: due to the fact that diodes of IGBT are always conductive in one direction, if a short circuit occurs in the AC or DC side of a VSC, the fault current can be very high. To prevent this, circuit breakers are opened, which requires the

HVDC link to be restarted. Since a LCC can control the amplitude of currents via their firing angle control, the fault current is limited, which reduces potential damages.

In light of all the advantages and technical capabilities of the VSC, although its power rating per submodule is limited and its fault current is high, it is often chosen in place of the LCC, even if it is more expensive compared to a LCC equivalent one.

Often, the rated power limitation is compensated by the use of bipolar topologies: by placing two VSC in series, the apparent voltage is doubled while maintaining the same line current, which doubles the transmitted active power. This is precisely what is done in the MOG II of *Elia*.

2.4 Motivations of Using Hybrid Links

The idea of using AC and DC parallel transmission links is not brand new. The very first one emerged in 1964 [29]. For four decades, the hybrid link has been considered as a way to improve power quality. Thanks to the apparition of the VSC, other improvements in power quality emerged, as well as transmission losses mitigation techniques.

This section aims to answer a part of the research question, related to the motivations of using a hybrid interconnector.

2.4.1 Hybrid Links with Line-Commutated Converters

As reported by *T. Machida* [30] in 1966, a parallel AC/DC transmission link is imagined, with a generator at one end and an external grid at the other end. Beyond the advantage of steady-state power transmission with fewer losses, the idea is to make use of the control of a LCC to adjust the active power locally to compensate for AC disturbances after a fault and to drastically reduce the voltage phase oscillations (or generator oscillations) resulting from the fault. Since the AC power modulation is fast, via a measure of the frequency deviation, firing angles are adjusted to control the active power output so that stability can quickly be recovered. In other terms, the DC link was used as an active power compensator. At that time, power converters could only be of LCC type, which has limited control capabilities, *i.e.* only the control of active power via Rectifier Current Regulators (see Section 2.3). Other authors studied the same idea in the following years (for example, *Li Wang et al.* [31] in 1993).

2.4.2 Hybrid Links with Voltage Source Converters

The birth of VSCs in the late 1990s gave rise to new possibilities. Since a VSC has reactive power control capabilities, a DC link in parallel to an AC one can now help with voltage regulation via the reactive power controller, along with the active power compensation.

In 1999, *Urban Axelsson et al.* [32] studied a hybrid transmission link, integrated in a small AC grid, with wind power production connected to one end-side. DC power flows through buried cables and AC via overhead lines. Two VSCs are used: one sets the DC voltage and the other one sets the active power. A voltage and a flicker controller are implemented at both VSC as well. If a voltage drop is detected, the reactive power controller instantaneously detects it and provides the right amount of reactive power.

Beyond power quality improvements, *Urban Axelsson et al.* [32] also introduce a transmission loss mitigation technique. According to the power to be transmitted, since active and reactive power can be controlled on the DC link, a repartition on both lines is made by a Supervisory Control And Data Acquisition (SCADA) system: active and reactive power references are then given to the *ad hoc* converter. A last argument in favor of this hybrid link is that it was a slightly cheaper installation than building another AC overhead line with the same capacity. This hybrid link was commissioned in December 1999 on the Swedish island of Gotland: it became the very first commercial HVDC link using VSC instead of LCC [33] (the Gotland island might also have been the place where the very first DC transmission line ($20MW$) using LCCs was installed, in 1954 [34]).

2.4.3 Princess Elisabeth Island Case

The MOG II features a hybrid interconnection between the Princess Elisabeth Island and the Belgian coast. This is the result of analysis of three proposed topologies, depicted in Figures 2.11a, 2.11b and 2.11c. They are discussed in a report of *Elia* from 2021 [12]: some details may have been modified since then.

The first variant is a pure AC interconnection with five $700MW$ platforms, the second is the hybrid interconnection with a unique energy island ($2.1GW$ in AC and $1.4GW$ in DC: since then, the capacity of the DC link was increased to $2GW$) and the third one consists in two distinct AC and DC transmission link with four platforms (three $2.1GW$ in AC and one $1.4GW$ in DC).

The choice of the second variant was selected for several reasons:

– Grid-forming issue: the AC interconnection is necessary in any case, whether there is a DC link or not. This can be justified from a grid-forming perspective. If it was not there, the DC link alone should have grid-forming capabilities: the voltage magnitude, frequency and phase angle should be set by offshore converters, which prevent them for transmitting active power at full potential, as a part of the power should be used to maintain the stability on the MOG II AC grid.

  Thanks to the presence of AC connections, the grid is already formed and power

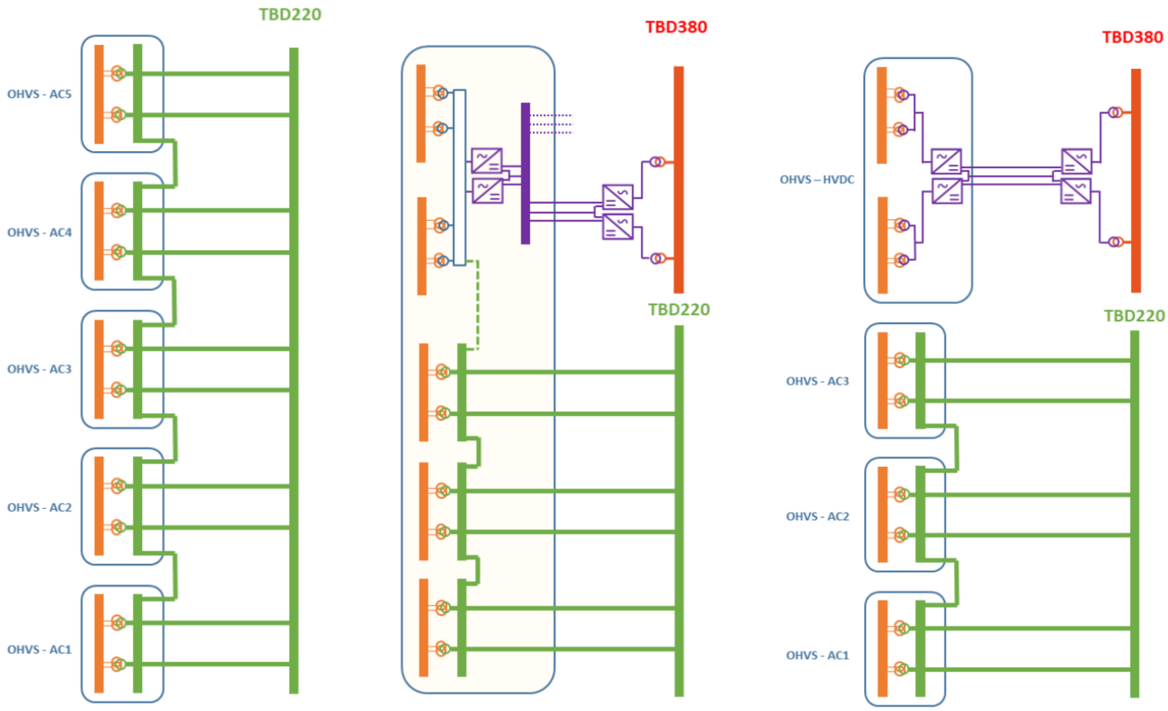

(a) Variant 1. (b) Variant 2. (c) Variant 3.

Figure 2.11: Variants of the MOG II proposed by *Elia*. Reproduced from [12].

converters can help in maintaining stability through a smaller control in terms of required power.

– Break-even distance and cumulated cable length: this link is about 45km long. From a cost point-of-view, it might correspond to the break-even distance, as mentioned in Section 2.1. Since the cost of an AC link is about the same as a DC one (at this length), mixing both represents an opportunity for the Belgian TSO *Elia* to gain knowledge and experience in the field of hybrid interconnectors.

  Also, from a cumulated length standpoint, variant 1 requires 990km (440km for inner cables and 550km for export cables), 980km for variant 2 (640km and 350km for inner and export cables) and 840km for variant 3 (440km and 400km for inner and export). Both AC and hybrid are justified according to these two criteria.

– Available space for cable landing: the Belgian coast is quite small. A part of it is already used for tourism, or preserved for ecological interest (polders). Based on the level of power to be transmitted, in variant 1, ten AC cables are needed. Practically speaking, a single landing zone would not be enough. Because of the available area for cable landing and the reluctance of local residents, it would be difficult to establish a second landing zone. With the DC alternative, only seven cables are needed, which solves this issue.

- Reactive power and resonance issues: as discussed in Section 2.1, AC cables generate reactive power, which has to be compensated to prevent voltage stability issues. Six AC cables already represent a challenge from the compensation point of view, and ten cables would be even more difficult. Also, analysis showed that these ten cables, along with their reactive compensator, would cause frequency issues, as the resonance frequency computed numerically (close to $100 Hz$) is a multiple of the base frequency (50Hz): such a grid configuration would present severe power quality issues due to these harmonics.

- Power quality: HVDC can support the AC grid from a power quality perspective, as discussed in this section. Also, the DC link ensures an electrical separation between wind turbines and the AC grid: direct interactions between wind turbines of different manufacturers could have had a negative impact.

- Future outlooks: due to the limited area of the exclusive economic zone of Belgium in the North Sea, a third wind farm might not be feasible. However, as the European Commission decided, in 2020, to increase the wind capacity from $12GW$ today to $60GW$ by 2030 and to $300GW$ by 2050, other countries will increase their installed wind power. For more flexibility, these countries are very likely to be interconnected in the next years, through HVDC cables, for energy exchanges.

  Instead of being directly connected to the Belgian grid, these cables could be gathered on a DC busbar located on the Princess Elisabeth Island to avoid additional cable length: if the wind farm does not produce enough power, the same hybrid link can be used to carry electricity imported in DC. Also, the DC busbar provides modularity: in addition to incoming HVDC cables from other countries, another DC link between the island and Belgium can be planned, which is not the case for variant 3. In the latter, the installed power cannot be modified.

  In the case of a pure AC export interconnection, no outlook for future interconnection is possible: at best, DC/AC power converters could be placed onto a fifth platform to convey imported electricity, and additional AC cables would be needed. In addition, it would be wise to connect a HVDC export cable if a power converter was to be installed, which leads to the idea of variant 2. So, this is a benefit from the economical point of view, as well as from an environmental one: a DC interconnection is thus welcome.

Although the HVDC part of variant 2 and 3 presents various advantages, HVDC links are usually less reliable than AC ones: power electronics equipment and their subcomponents are more prone to defaults than robust AC transformers. In case of a converter fault, the power outage would be more important than in the case of one out of ten AC cables.

In light of the arguments against variant 1, the latter can be excluded, and variant 2 seems to be the most promising configuration. The choice of variant 2 instead of variant

3 is also justified by two arguments. Having only one island should be better than four platforms, from an environmental point of view, as fauna and flora will be disturbed in a smaller effective zone. The reliability would also be increased, as no $220kV$ inner cables would be needed - which is better for maintenance - and spare parts could be stored on the energy island for a quick replacement, whereas large boats with enough space to transport equipment would be needed to go and replace equipment on one of the four platforms.

Thanks to this section, a part of the research question, concerning the benefits and drawbacks of using a hybrid interconnector, is now answered.

2.5 Aggregated Model of a Wind Turbine

In order to model the generation units of the MOG II, a steady-state model of a wind turbine can be used. This section introduces a wind model and an aggregated model of varying-speed wind turbines.

2.5.1 Wind Model

Wind refers to the movement of air molecules. Over a certain period of time and at a defined location, the axial wind speed can be split up in a deterministic part and a stochastic part [35]. The deterministic part is composed of an mean value $m(t)$, a ramp $r(a_w(t), t)$ characterized by a wind acceleration $a_w(t)$, and gusts $g(t, T, I)$ with various durations T and intensities I.

The stochastic part includes turbulences, coming from the imperfect nature of the wind speed vector field, or generated when wind travels through a wind turbine (wake loss at the blade, air flow deviation due to the presence of the tower, ...). These turbulences lead to a decrease of the power generated, as energy is harvested from the reduction of the axial wind velocity. In a simple model that approximates the power generated by wind turbines, turbulences are neglected.

In order to enhance the realism of the model and to consider high frequency variations, noise $n(B, t)$ can be added, with a bandwidth B corresponding to the one of the studied problem dynamics. At the end, the axial wind speed can be written as

$$v_w(t) = m(t) + r(a_w(t), t) + g(t, T, I) + n(B, t). \tag{2.1}$$

2.5.2 Wind Turbine Model

The goal of a wind turbine is to convert the kinetic power, contained in the wind speed, into active electrical power. It is composed of a rotor, catching the wind kinetic energy at a certain height, connected to an electromechanical converter that turns mechanical power into electrical power.

Depending on the rotational speed (constant or variable) and on the type of electromechanical converter used (synchronous or asynchronous), a wind turbine belongs to one of the four following types:

- Type 1 is a constant speed wind turbine, based on an asynchronous generator.
- Type 2 is an upgraded version of the Type 1, where variable rotor resistances are added to enable a small range of rotation speed.
- Type 3 refers to a Doubly-Fed Induction Generator (DFIG, see Figure 2.12), where both stator and rotor windings are excited: stator windings are directly connected to the grid and rotor windings are connected to a back-to-back power inverter, allowing for a dynamic slip control, resulting in a wide range of rotational speeds [36].
- Type 4 wind turbines use Permanent Magnet Synchronous Generators (PMSG, see Figure 2.13), connected to the grid through a full-scale power converter in order to maintain output voltages and currents at the same frequency as the one of the grid. This full-scale converter also allows for a large range of rotational speed, compared to Type 1 and 2.

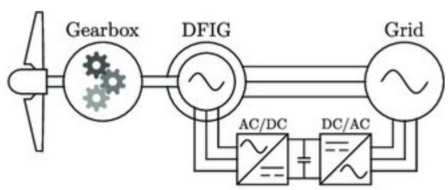

Figure 2.12: Type 3 Wind Turbine. Reproduced from [37].

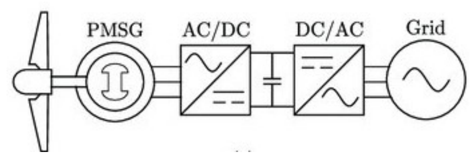

Figure 2.13: Type 4 Wind Turbine. Reproduced from [37].

For a wind turbine with rotor radius R, the mechanical power extracted from the wind is equal to

$$P_{mech} = \frac{1}{2}\rho \pi R^2 v_w^3 c_p(\lambda, \beta). \tag{2.2}$$

This result comes from the kinetic energy by wind mass unit multiplied by the mass flow through the area swept by the rotor blades. In Eq. (2.2), ρ is the air mass density. The performance coefficient, c_p, illustrates the amount of power extracted from the wind power. It depends on the blade pitch angle β and on the tip-speed ratio λ

$$\lambda = \frac{\omega R}{v_w}, \tag{2.3}$$

which is the ratio between the tangential speed at the tip of the blades (ωR) and the axial speed of the wind (v_w).

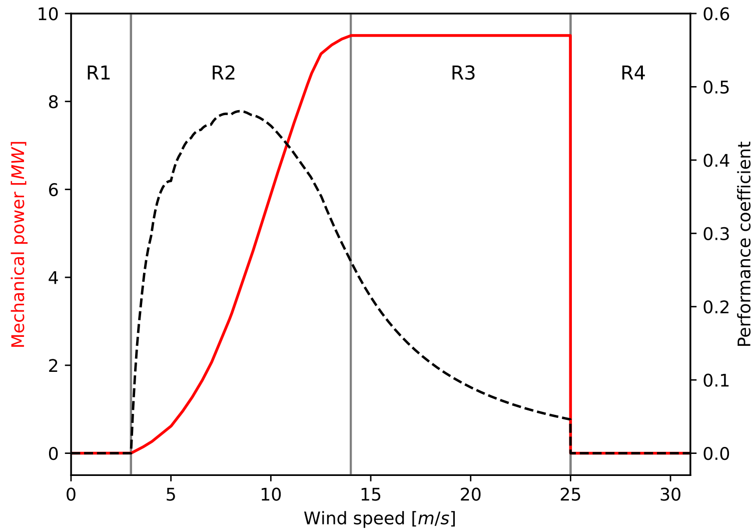

Figure 2.14: Characteristic power curve (solid line) and performance coefficient (dashed line) of the *Vestas V164* 9.5MW Type 4 wind turbine. Reproduced from [38].

Figure 2.14 shows a typical power curve in function of the wind speed v_w for Type 3 and Type 4 wind turbines. It can be divided into four regions:

- R1: v_w is not high enough to start the turbine rotational movement and to counteract the static resistive torque.
- R2: Once the cut-in speed is reached, the turbine starts rotating. A Maximum Power Point Tracking (MPPT) controller adapts the resistive electromagnetic torque based on the rotor speed ω. The blade pitch angle β is kept constant.
- R3: If the maximum power is reached, the wind turbine controller keeps the output power constant by reducing the aerodynamic efficiency, which is achieved by acting on the blade pitch angle β, while keeping the rotational speed ω constant.
- R4: Above the cut-out speed value, the wind turbine is stopped to prevent mechanical damage to the elements of the wind turbine.

These controllers, along with the behavior of electromechanical converters, generate a dynamic system. In order to neglect the transients linked to controllers and electromechanical converters, a simplified model can be used to approximate the electrical output, steady-state power generated by a Type 3 or Type 4 wind turbine. This aggregated model is depicted in Figure 2.15.

First, the wind is filtered: since wind may contain high order frequencies that do not affect the output power, this low-pass filter reduces the spectrum of the wind speed.

This filter is characterized by the time constant τ. Considering a maximum frequency of $10Hz$ affecting the output power, τ must be equal to $100ms$.

Then, the mechanical power is computed. It basically applies Eq. (2.2), where the performance coefficient c_p is kept at its maximum value, which is a rough approximation of the R2 region in Figure 2.14.

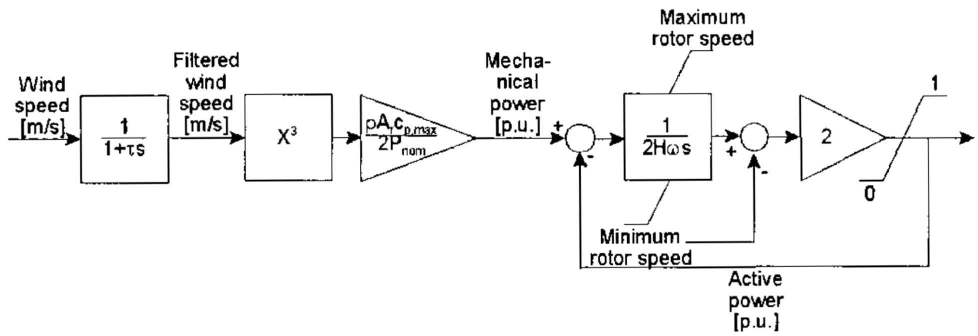

Figure 2.15: Simplified variable speed wind turbine model. Reproduced from [35].

In the R3 region, due to the reduction of the aerodynamic efficiency, c_p is supposed to decrease, so that the output active power is kept constant. Although there is no power limiter after the mechanical power computation in Figure 2.15, a maximum rotor speed boundary and a maximum electrical active power limit are added, in such a way that the output electrical power is kept at its maximum, even if the mechanical power keeps rising in the model but not in reality.

The *Swing Equation* computes the rotational speed ω, in function of the imbalance between mechanical and electromechanical torque [39]. It is written as

$$J\frac{\partial \omega}{\partial t} = T_m - T_e, \tag{2.4}$$

where J represents the moment of inertia, in $kg.m^2$, of the rotating mass system. The latter should properly be modeled by three masses: the flexible blades, the rigid blades with the central hub, and the rotor of the electromechanical converter, connected through two transmissions, each modeled by a damping coefficient and a stiffness coefficient. The assumption made here is that this whole rotating mass system is considered as one rigid rotating mass represented by J [40]. T_m and T_e are respectively the mechanical and electromechanical torque, in $N.m$. They are defined as positive in the generator convention.

By multiplying both sides of the equation by the rotational speed ω and rearranging terms, using the *Laplace* variable s for the derivative, the updated rotational speed ω_{i+1}

can be obtained via

$$\omega_{i+1} = \frac{P_m - P_e}{s.J\omega_i} \text{ [rad/s]}. \tag{2.5}$$

The relation linking the moment of inertia J with the inertia time constant H is expressed as

$$H = \frac{1}{2}\frac{J\omega_B^2}{S_B} \text{ [s]}, \tag{2.6}$$

where ω_B is the rated speed of the wind turbine and $S_B = \omega_B T_B$ is the rated apparent power. By using Eq. 2.6, the updated speed can also be expressed as

$$\omega_{i+1}^{pu} = \frac{P_m^{pu} - P_e^{pu}}{2H\omega_i^{pu}.s} \text{ [p.u.]}, \tag{2.7}$$

where rotational speeds and powers are now expressed in per unit $(p.u.)$.

The last step is the active power computation, based on the rotational speed ω. For the sake of simplicity, only the active power generation is considered in this model, although reactive power can also be produced either by a DFIG induction generator, or by the DC/AC power converter of a Type 4 wind turbine. Figure 2.16 shows a typical active power curve resulting from a controlled Type 3 wind turbine. The idea in the simplified model in Figure 2.15 is to approximate this curve by a linear relation: after the minimum rotor speed is subtracted to the rotor speed, a coefficient 2 is applied. According to the range of rotational speed of wind turbines, this coefficient can be adjusted, but it remains close to 2. As for a Type 3, Figure 2.17 depicts a typical active power curve resulting from a controlled Type 4 wind turbine: the characteristic curve is linearized and highlights the difference between it, the optimal MPPT curve, and the one achieved by the simplified model.

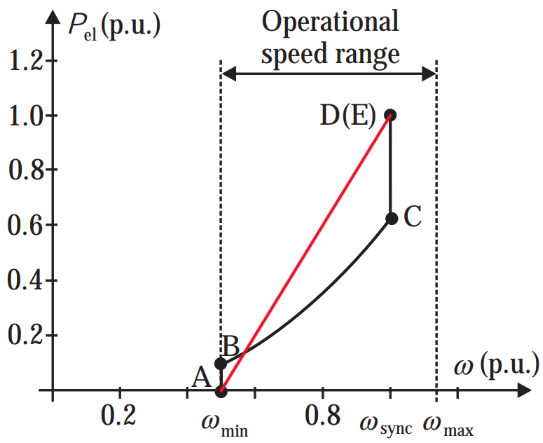

Figure 2.16: Active electrical power characteristic in function of rotor speed for a DFIG Wind Turbine with linearized characteristic (red line). Adapted from [40].

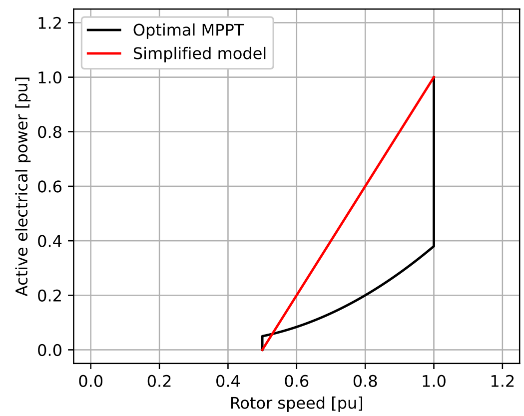

Figure 2.17: Active electrical power characteristic in function of rotor speed for a PMSG Wind Turbine with linearized characteristic (red line). Adapted from [41].

This wind turbine model is compared with a real characteristic power curve of an existing wind turbine, in Section 4.3.

2.6 Summary

In this section, an overview of existing technologies related to AC and DC power transmission is presented, and technological choices of the MOG II are justified. A simplified model of varying speed wind turbines is introduced so as to approximate generation units in the MOG II.

A comparison between AC and DC cables is presented. Two factors are used to compare both technologies: the maximum active power transmissible - that decreases with the distance - and the initial cost of the system. Over long distances, it is shown that AC cables suffer from huge active power losses. DC links, on the other hand, have an initial cost greater than the one of AC links. In the MOG II, both technologies are used as their length corresponds to the break-even distance, where both total costs are about the same.

Two technologies of AC/DC power converters exist: the LCC and the VSC. The latter presents better capabilities in terms of power and voltage control, generates AC voltages with a lower harmonic content and does not have commutation failures, compared to the LCC. However, it has a limited maximum rated power. The MOG II features 4 VSC: in order to compensate for this drawback, the terminal topology chosen is a bipolar one, so as to double the final power transmitted.

Given that both AC and DC links are used in parallel in the MOG II, motivations are developed to justify this technical choice. A hybrid link can help in power quality, regarding frequency deviations and voltage drops. Also, it cancels the need for a grid-forming converter. Other explanations regarding the available space for cable landing, financial costs and future outlooks for the MOG II justify this hybrid link.

Finally, an aggregated model of Type 3 (DFIG) and Type 4 (PMSG) wind turbines is presented, along with an axial wind speed model. The wind turbine model is based on two hypotheses: the approximation of the performance coefficient by its maximum value and the linearization of the electrical power curve in function of the rotor speed.

Since technological choices of the MOG II are made, each network element can be modeled. In Section 3, AC and DC cables and the VSC (with its controllers) are modeled. A wind farm model is also developed. These models are then used to develop an active power dispatch controller.

Chapter 3

Modeling and Theoretical Analysis of the Modular Offshore Grid II

Throughout this section, a grid composed of a wind farm, the MOG II with its hybrid interconnection and the onshore system is modeled. The aim of this model is to allow for steady state loadflow simulations, achieved throughout this chapter and Chapter 4.

The global model of the electrical system, with the MOG II, is depicted in Figure 3.1. Although this grid was subject to discussions and modifications, this configuration, most likely, represents the final design of the MOG II [3]. The power capacity of the $220kV$ AC export cables (in green) should reach $2.1GW$ and $2GW$ for the $525kV$ DC cables (in purple). Orange cables are the $66kV$ AC inner cables that convey the generated power towards the energy island.

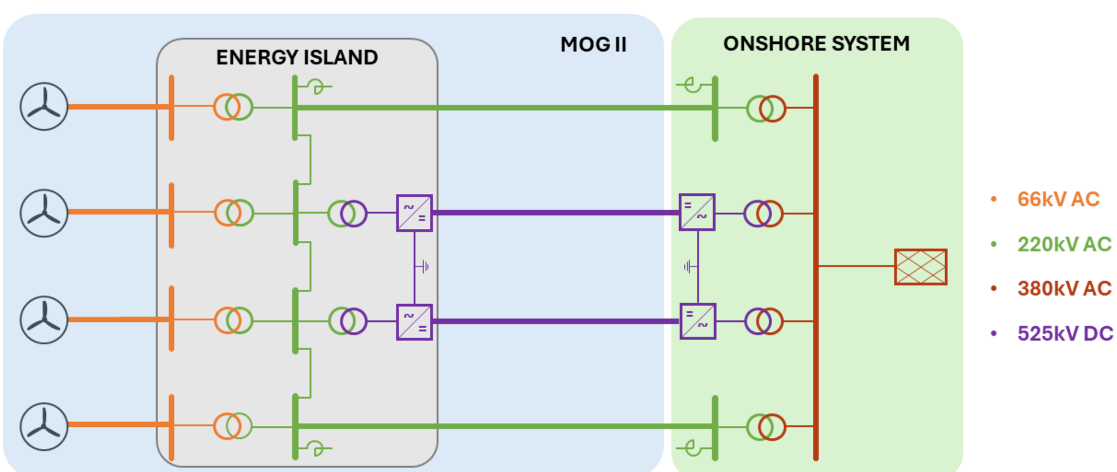

Figure 3.1: Global model of the electrical system with the MOG II.

Following Figure 3.1, from left to right, this global model contains:

- 4 wind parks: 2 of $1050MW$ and 2 of $700MW$ (Section 3.5).
- 50 $66kV$ AC inner cable of $4km$ to $19km$ long (Section 3.1).
- 4 sets of $66kV$ busbars (Section 3.4).
- 10 $66kV/220kV$ transformers (Section 3.4.2).
- 4 sets of $220kV$ busbars (Sections 3.4), with reactive power compensators (Section 3.1.3).
- 4 step-up transformers to rise the voltage - starting from $220kV$ - before the power converters. That voltage is *a priori* unknown, but is approximated in Section 3.2.1.4.
- 2 AC/DC converters connected in a bipolar topology, reaching a DC voltage of $\pm 525kV$ (Section 3.2.1).
- 2 $525kV$ DC export cable, one of positive and one of negative polarity (Sections 3.2.2 and 3.2.3).
- 6 $220kV$ AC export cables (Section 3.1).
- 2 DC/AC power converters (Section 3.2.1).
- $220kV/380kV$ transformers.
- 4 transformers to match the converter output voltage to the $380kV$ grid (Section 3.2.1.4).
- 1 Point of Common Coupling with the $380kV$ onshore grid.

As explained in Sections 1 and 2.4.3, *Elia* also plans to add a DC busbar for future interconnections with the United Kingdom (*National Grid Venture*), via the *Nautilus* link, and with Denmark (*Energinet*) via the *Triton* link, for electrical energy trading. A second HVDC connection to the center of Belgium is also scheduled.

This grid is designed to be modular: it has a certain level of redundancy for robustness purposes. This topic is covered in Section 3.4.

3.1 AC Transmission System

3.1.1 Active and Reactive Power Transmission Model

For loadflows simulations, AC cables are often modeled by a pi-section, with 3 lumped parameters per unit length and per phase: a resistance R, an inductance L and a capacitance C split in two capacitances of $C/2$, at both ends of the pi-section (see Figure 3.2). This model is valid for short cables (<50km) and overhead lines between 100km and 300km [42]. Given that the longest cables of the MOG II are export cables of 45km long, the hypothesis is valid and the pi-section can be used to model all cables of the MOG II.

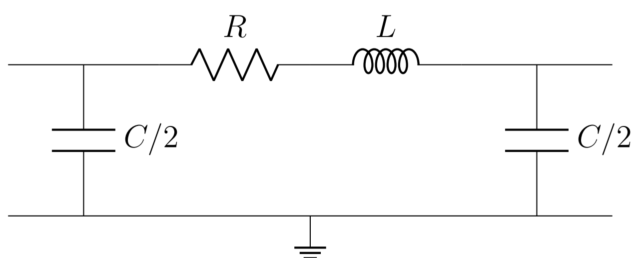

Figure 3.2: Pi-section model for one phase of an AC cable, or one polarity of a DC cable.

Depending on the balance situation of the network, those parameters are defined twice: one for the positive sequence (or direct component) and negative sequence (or indirect component), and one for the zero sequence (or homopolar component). Under the assumption that the three-phase variables of the network are always balanced, the homopolar component can be neglected. This hypothesis is valid as long as there is no path for the zero sequence, which can be guaranteed for cables (no neutral) and transformers, in case of $Y\Delta$ or $Yn\Delta$ connection scheme [43].

For short (<100km) high-voltage or extra-high voltage overhead lines, capacitances can be neglected such that the line model consists in a single complex impedance, as reactances linked to these capacitances reach hundreds of $k\Omega/km$. This model is called the “impedance line model” in the rest of this document. However, in cables, the value of these reactances reaches some $k\Omega/km$ such that they cannot be neglected when modeling cables [42]. In practice, the $C/2$ capacitance of an overhead line is about some nF/km, whereas the one of a cable reaches hundreds of nF/km.

Beyond the active power transmission model - which is the “useful” part of the apparent power -, reactive power must also be approximated. Due to the presence of the aforementioned capacitances that generate reactive power, the total reactive power at cable ends is highly affected. In a network, an excess of reactive power presents several drawbacks and concerns:

- Generation units produce more active power to compensate for this additional power which is, though useless, required. This results in a higher current, thus increasing losses and costs of maintenances.

- The power factor is degraded by the increase of reactive power, which results in a greater apparent power and a greater congestion in transmission lines. So, the grid ability to transmit useful active power is reduced, since cables are loaded with quadrature currents.

- Reactive power is at the heart of voltage stability issues: it causes voltage drops that can damage equipment.

- Power quality issues may also occur, especially due to harmonic distortions.

The Belgian grid is operated at a frequency of $50Hz$. By replacing inductive and capacitive elements by their equivalent impedance at this frequency, and by using conventions in Figure 3.3, the active and reactive power at sending and receiving ends can be computed.

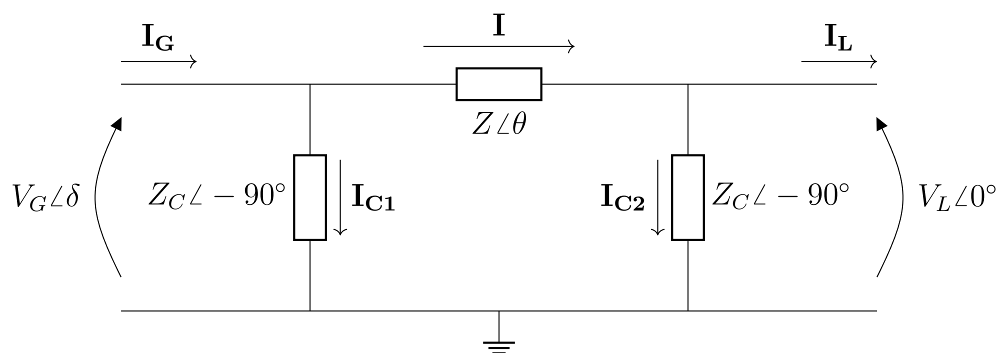

Figure 3.3: Conventions used in the pi-section to compute active and reactive powers. Voltages are labeled $\mathbf{V_G}$ for the generator side, and $\mathbf{V_L}$ for the load side. If the reference phase angle of the voltage is the load side, δ is the phase angle of the generator side voltage (also called "transmission angle"). Sending end and receiving end currents are labeled $\mathbf{I_G}$ and $\mathbf{I_L}$.

Let $\mathbf{Z} = Z\angle\theta = R + j\omega L$ be the complex impedance of the series elements, with $Z = \sqrt{R^2 + (\omega L)^2}$ and $\theta = \arctan(\frac{\omega L}{R})$. The current $\mathbf{I} = I\angle\phi$ flowing through it can be written as

$$I\angle\phi = \frac{V_G\angle\delta - V_L\angle 0}{Z\angle\theta}. \tag{3.1}$$

The angle ϕ varies according to Eq. (3.1): in the impedance line model, it is used to compute the power factor ($p.f. = \cos(\phi)$) at the load or at the generator, and this power factor describes the amount of active power for a given apparent power. However, because of the capacitive currents $\mathbf{I_{C1}}$ and $\mathbf{I_{C2}}$, the input cable current $\mathbf{I_G}$ is not the same as the output one ($\mathbf{I_L}$): this angle can therefore not be used to compute power factors.

Let $\mathbf{Z_C} = Z_C\angle - 90° = j\frac{-1}{\omega C/2}$ be the complex impedance of the parallel elements, through which capacitive currents $\mathbf{I_{C1}}$ and $\mathbf{I_{C2}}$ flow. Generally speaking, the apparent power at a node i is computed as

$$\mathbf{S_i} = \mathbf{V_i}\mathbf{I}^* = P_i + jQ_i, \tag{3.2}$$

where $\mathbf{I}^*$ is the complex conjugate of $\mathbf{I}$, $P_i = \Re\{\mathbf{S_i}\}$ is the active power and $Q_i = \Im\{\mathbf{S_i}\}$ is the reactive power at that node. Using the current $\mathbf{I}$ computed in Eq. (3.1), the apparent power at the sending end per phase (generator) is computed as

$$\begin{aligned}\mathbf{S_G} =& \mathbf{V_G}(\mathbf{I_G}^*) = \mathbf{V_G}(\mathbf{I}^* + \mathbf{I_{C1}}^*)\\ =& \mathbf{V_G}\Big(\frac{\mathbf{V_G}^* - \mathbf{V_L}^*}{\mathbf{Z}^*} + \frac{\mathbf{V_G}^*}{\mathbf{Z_C}^*}\Big)\\ =& \frac{V_G^2 e^{j\theta}}{Z} - \frac{V_G V_L e^{j(\delta+\theta)}}{Z} + \frac{V_G^2 e^{-j90°}}{Z_C}.\end{aligned} \tag{3.3}$$

Active and reactive powers are then found by separating the real and imaginary parts:

$$\begin{cases} P_G = \dfrac{V_G^2}{Z}\cos(\theta) - \dfrac{V_G V_L}{Z}\cos(\theta+\delta)\\ Q_G = \dfrac{V_G^2}{Z}\sin(\theta) - \dfrac{V_G V_L}{Z}\sin(\theta+\delta) - V_G^2\dfrac{\omega C}{2}.\end{cases} \tag{3.4}$$

It can be noted that the additional term $V_G^2\frac{\omega C}{2}$ in the reactive power Q_G is the only difference between the complete π-section model and the impedance line model consisting in the complex impedance $\mathbf{Z}$, where the reactance associated to $C/2$ is regarded as being greater than Z.

However, since the values of capacitances in cables are much greater than in overhead lines, neglecting the capacitive part of the model would result in a false approximation of the reactive power produced in the cable. One would therefore get a wrong estimation of the reactive power to be compensated, *e.g.* via capacitor banks or shunt reactors, in case of a lack or an excess of reactive power respectively, or via other FACTS (Flexible AC Transmission Systems), such as a SVC (Static Var Compensator) or a STATCOM (Static Synchronous Compensator). In the case of the MOG II, shunt reactors are used.

Similarly, using Eq. (3.1) for the receiving end (load), the apparent power is computed as

$$\begin{aligned}\mathbf{S_L} =&\mathbf{V_L}\mathbf{I_L}^* = \mathbf{V_L}(\mathbf{I}^* - \mathbf{I_{C2}}^*)\\ =&\mathbf{V_L}\Big(\frac{\mathbf{V_G}^* - \mathbf{V_L}^*}{\mathbf{Z}^*} - \frac{\mathbf{V_L}^*}{\mathbf{Z_C}^*}\Big)\\ =&\frac{V_G V_L e^{j(\theta-\delta)}}{Z} - \frac{V_L^2 e^{j\theta}}{Z} - \frac{V_L^2 e^{-j90^\circ}}{Z_C},\end{aligned} \tag{3.5}$$

and the resulting active and reactive power per phase at the load end is defined as

$$\begin{cases} P_L =\dfrac{V_G V_L}{Z}\cos(\theta-\delta) - \dfrac{V_L^2}{Z}\cos(\theta) \\ Q_L =\dfrac{V_G V_L}{Z}\sin(\theta-\delta) - \dfrac{V_L^2}{Z}\sin(\theta) + V_L^2\dfrac{\omega C}{2}. \end{cases} \tag{3.6}$$

Again, the same observation can be done: the $V_L^2\frac{\omega C}{2}$ term is also the unique difference with the impedance line model, and neglecting the two capacitances - in presence of cables - also leads to an wrong estimation of the reactive power to be compensated, as this term is far from being negligible: in some situations, it can represent up to 50% (or more) of the reactive power Q_L.

One interesting variable is the active power received at the load side: it can be noticed that P_L is maximized when $\theta = \delta$, *i.e.* when the transmission angle matches the series impedance angle. This angle, however, cannot be set as it is the result of the spontaneously established loadflow.

At the end, by knowing the cable parameters, the rated voltage and the transmission angle, every other quantity can be approximated using Eqs. (3.4) and (3.6). This is valuable to foresight the active and reactive power generated, and to mitigate the latter.

3.1.2 Maximum Active Power Transmission

In Section 2.1, a key limitation of AC cables is introduced: the reduction of active power transmission with the rise of the cable length. This phenomenon is due to the active power losses, caused both by the increase of the magnitude of $\mathbf{I}$ in Figure 3.3 and the increase of the line resistance R of the pi-section in Figure 3.2: these active losses are computed as $3RI^2$ per cable.

The explanation of the increase of the cable transmission line resistance R is straightforward: if R_L is the resistance per unit of length, $R = LR_L$ increases linearly with the cable length L. By choosing R_L greater than the one corresponding to the conductor resistance, this resistance model represents the skin effect growing along with the cable length.

The evolution of the current magnitude is studied using a simulation of a cable model. In the remainder of this section, simulations are referred to as the simulation of three pi-sections per cable, using the *DIgSILENT PowerFactory* software: these pi-sections are identical to the one introduced previously. In contrast, the “model” means the use of the analytical model described in Section 3.1.1, and also based on the pi-section model. Since the simulation uses the same pi-section as the one used to derive the analytical model, equations of Section 3.1.1 can be used to interpret the simulation results.

The current magnitude evolves following Eq. (3.1): considering V_L as constant (set by the external grid), since θ is independent of the distance L, only the line impedance magnitude Z and $\mathbf{V_G}$ vary. The following Figures 3.4, 3.5, 3.6 and 3.7 show the evolution of the phasor quantities $\mathbf{V_G}, \mathbf{I}, \mathbf{I_{C1}}$ and $\mathbf{I_G}$ obtained from results of the simulation of the detailed model, when considering a constant, rated power P_G while increasing the cable length on a $220kV$ cable.

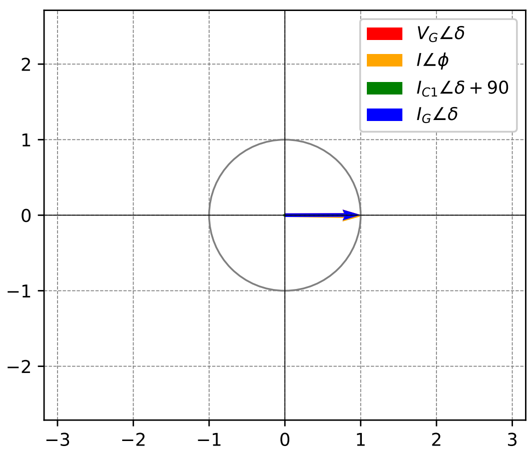

Figure 3.4: Phasor diagram of variables of a $220kV$ cable for $L = 5km$ and $P_L = 1pu$.

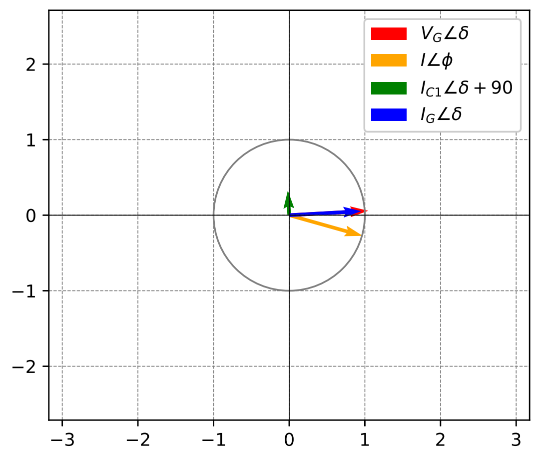

Figure 3.5: Phasor diagram of variables of a $220kV$ cable for $L = 80km$ and $P_L = 0.97pu$.

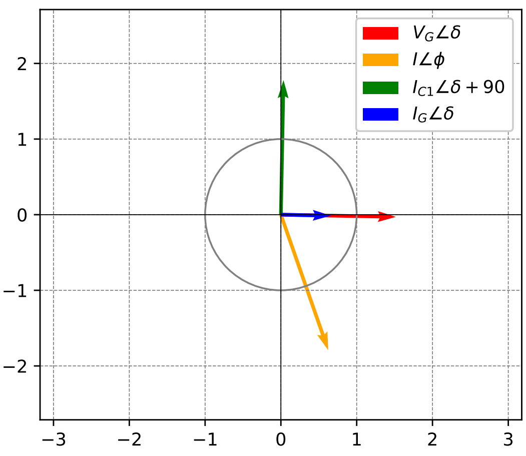

Figure 3.6: Phasor diagram of variables of a $220kV$ cable for $L = 300km$ and $P_L = 0.62pu$.

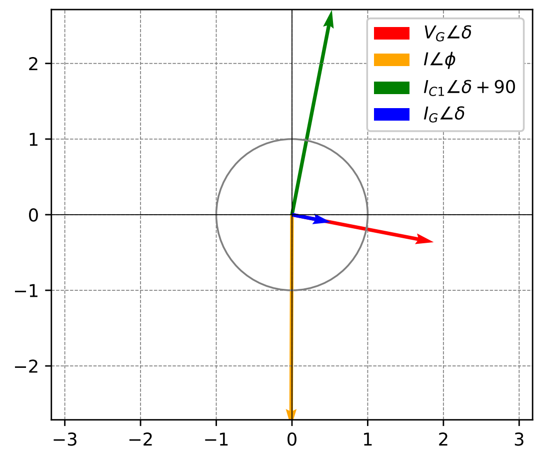

Figure 3.7: Phasor diagram of variables of a $220kV$ cable for $L = 370km$ and $P_L = 0pu$.

In these figures, it can be observed that V_G increases: it grows up to $2.0p.u.$. This is due to the increase of the cable line impedance and the reactive power produced by cables, which is to be related to the increase of the cable capacitances. Also, the phase ϕ and the magnitude of the current $\mathbf{I}$ rise. This can be explained graphically. At the generator side of the cable, $\mathbf{I_G}$ is in phase with $\mathbf{V_G}$. The capacitive current $\mathbf{I_{C1}}$ is leading $\mathbf{V_G}$ by $\pi/2$. This current is subtracted to $\mathbf{I_G}$ to obtain $\mathbf{I}$. As I_G decreases with the rise of V_G and as I_{C1} increases - both with the reduction of the shunt impedance linked to the increasing capacitance and with the increase of V_G -, the magnitude of the current $\mathbf{I}$ increases along with its phase ϕ. The increase of current magnitude I is thus explained by the increase of the capacitive current I_{C1}.

The explanation behind the maximum active power transmissible is thus based on the increasing Joule losses, caused by the increase of the series resistance and by the increase of the capacitive currents. In order to confirm this explanation, Figure 3.8 depicts the evolution of P_L according to the cable length, obtained by the simulation of the cable model. These simulation results are compared to an estimate of P_L when considering only Joule losses, *i.e.* by applying $1 - 3RI^2$ based on the per unit current I deduced from simulation results.

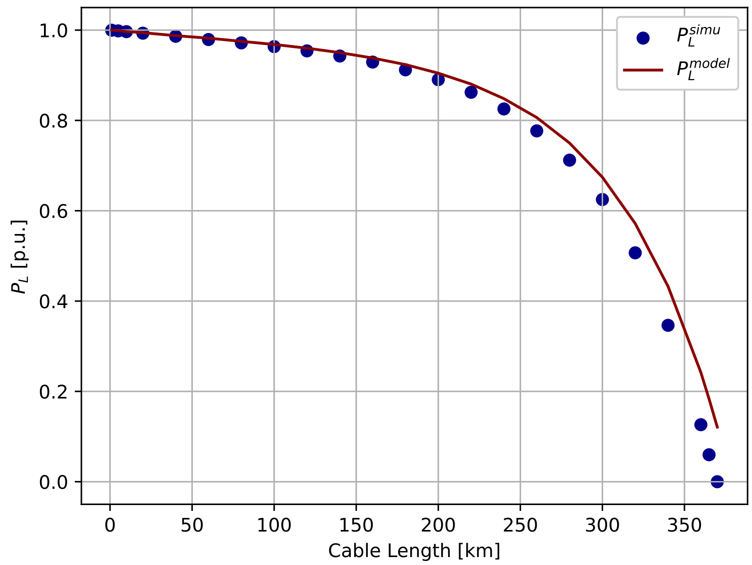

Figure 3.8: Comparison of P_L in function of the cable length. The blue dots illustrate the results of the simulated pi-section model using *DIgSILENT PowerFactory* and the red curve represents the estimated P_L, only based on the Joule losses model.

The estimated active power losses lead to a transmitted active power close to the expected P_L: the difference is smaller when the cable length gets smaller. The small difference between the simulation and the model might be caused by the transmission angle imprecision (tenths of a degree can make a great difference, see Section 4.1). However, the increasing trend of the error suggests that one - or more - additional effect is missing in order to completely explain the simulation results, more than only with the Joule losses model. As a result, the decreasing trend of P_L can largely - but not completely - be explained by the increase of the Joule losses, through the rise of the cable resistance and the rise of the line current I (the latter is caused by the increase of the capacitive currents because of the rise of V_G). This explanation answers the part of the research question about the explanation of the maximum active power transmissible by a cable.

Besides, it can be pointed out that the pi-section model is valid for small cable lengths ($<50km$). Beyond this distance, a distributed parameters model should be preferred: this might partially explain the distance at which $P_L = 0$, which is greater compared to the ones in Figure 2.5 (between $130km$ and $175km$).

3.1.3 Sizing of Shunt Reactors

As mentioned before, inductances can be placed in parallel to the capacitances (one per phase) in order to reduce the reactive power generated by AC export cables, so as to mitigate the generated reactive power. Computations below are valid to compensate the reactive power of one phase of one cable, but the model can be easily extended to three phases, and for more than one cable.

The connection configuration of the inductances described above is referred to as star connection, but shunts reactors could have also been placed in delta connection: in that configuration, inductances are placed between phases. In this case, the assumption of a star-connection is made. Because of the insertion of shunt reactors (inductances L_{sh}), the value of the parallel impedance needs to be updated as

$$\mathbf{Z_{eq}} = \left(\frac{1}{\mathbf{Z_C}} + \frac{1}{\mathbf{Z_L}}\right)^{-1} = \left(j\omega C/2 + \frac{1}{j\omega L_{sh}}\right)^{-1} = \frac{\omega L_{sh}}{1-\omega^2 L_{sh} C/2} \angle +90^\circ, \tag{3.7}$$

which puts in parallel the reactances linked to the capacitance and the reactances linked to the inductances. Reactive powers at generator and load side (Eqns. (3.4) and (3.6)) become

$$\begin{cases} Q_G = \dfrac{V_G^2}{Z}\sin(\theta) - \dfrac{V_G V_L}{Z}\sin(\theta+\delta) + V_G^2 \dfrac{(1-\omega^2 L_{sh,G} C/2)}{\omega L_{sh,G}} \\ Q_L = -\dfrac{V_L^2}{Z}\sin(\theta) + \dfrac{V_G V_L}{Z}\sin(\theta-\delta) - V_L^2 \dfrac{(1-\omega^2 L_{sh,L} C/2)}{\omega L_{sh,L}}. \end{cases} \tag{3.8}$$

The aim of this shunt reactor is, at least, to reduce, to consume reactive power, at best, to cancel it completely. It can be noticed that the reactive power produced by the cable capacitances can be entirely consumed if L_{sh} is chosen such that $50Hz$ is the resonance frequency, *i.e.* $1/(\omega^2 C/2)$.

One way to determine these inductances is to set $Q_G = 0$ and $Q_L = 0$. This results in

$$\begin{cases} L_{sh,G} = \dfrac{1}{\omega^2 C/2 - \left(\dfrac{\omega(V_G\sin(\theta) - V_L\sin(\theta+\delta))}{V_G Z}\right)} \\ L_{sh,L} = \dfrac{1}{\omega^2 C/2 - \left(\dfrac{\omega(V_L\sin(\theta) - V_G\sin(\theta-\delta))}{V_L Z}\right)}. \end{cases} \tag{3.9}$$

First, it has to be mentioned that L_{sh} should be close to the value that cancels the effect of the capacitance, at $50Hz$: it is increased a little by the additional reactive power to cancel (second term of the denominator in Eq. (3.9).) Also, it is worth noting that the value of the inductances depends on the transmission angle δ, itself depending on the level of active power at a node, and on the voltage levels V_G and V_L at cable ends. If the shunt reactors cannot be controlled (which is presumed in this case), those three variables must be set at design point, in a defined scenario, so as to find the value of inductances of the shunt reactor.

In practice, the reactive power to be compensated can be given as input, in $MVAr$, to compensators: for simulations introduced in Chapter 4, reactive powers, computed at $220kV$ busbars where AC export cables are connected, are specified in the reactive power compensators. The relation linking inductances of shunt reactors and reactive power to be compensated is

$$Q_{comp} = 3\frac{(V_r/\sqrt{3})^2}{\omega L_{sh}} = \frac{V_r^2}{100\pi L_{sh}}, \tag{3.10}$$

where V_r is the rated line-to-line voltage at the connection point of the shunt [44]. As L_{sh} is computed in case of a complete reactive power cancellation, the obtained reactive powers Q_L and Q_G should be exactly zero if only the reactive power due to $220kV$ cables is considered.

It can be noted that $220kV$ busbars connected to AC/DC converters do not need any compensators, as DC cables do not produce reactive power and, if needed, these converters have reactive power production and consumption capabilities, via dedicated controllers (see Section 3.2.1.2): as for compensators, reactive power reference (0 at best) can be given as a reference Q^* to the converter.

3.1.4 AC Cables Technical Parameters

The pi-section model in Figure 3.2 has three parameters. Depending on the apparent power to be transmitted in cables and on the rated voltage chosen, those three parameters are adapted. The maximum apparent power that can be transmitted by a three-phase cable or line can be computed via

$$S = 3V_{ph-gnd}I = \sqrt{3}V_{l-l}.I, \tag{3.11}$$

where V_{ph-gnd} is the phase-to-ground voltage, V_{l-l} is the line-to-line voltage and I is the per-phase current.

Two types of AC cables are used in the MOG II: about 50 inner cable connecting wind turbines to the energy island, and 6 export cables. These cables are supposed to be three-phase copper cables (see Figure 3.9).

Figure 3.9: Three-core cable section (with optic cable). Reproduced from [45].

The rated voltage chosen for inner cables is $66kV$ for several reasons [46]:

- *Elia* plans to connect wind turbines of $14MW$ to $18MW$ to the Princess Elisabeth Island via 50 strings: these are the expected rated power of wind turbines by 2027-2030. Since the wind power capacity to be installed is $3.5GW$, each cable carries about $70MW$. At this power, considering 4 or 5 wind turbine per string, the maximum current would locally reach close to $615A$, which is acceptable compared to datasheets of $66kV$ cables.

- Turbine manufacturers do not (yet) work in $132kV$ generators, which could have been an alternative voltage for inner cables, whereas $66kV$ generators already exist, which cancels the need of a step-up transformer. So, although reducing active power losses, higher voltages (*e.g.* $132kV$) would have increased the total cost of installation.

- The length of these cables varies between 4 and 19 km: lower voltage (*i.e.* $33kV$) would cause a bit more active power losses, although the reactive power produced is a bit increased in the $66kV$ scenario [47]. Another possibility would have been to divide by two the number of wind turbines per inner cable, which imposes to double the number of $33kV$ inner cables: this solution would have been more expensive than the $66kV$ solution.

For the 6 export cables, a $220kV$ technology was chosen. This link should carry up to $2.1GW$, which means $350MW$ per cable and a maximum current of $920A$ per phase.

Simulations of the AC system carried out in Chapter 4 are done under the assumption of a balanced system, such that zero sequence parameters are neglected (see

Section 3.1.1). The parameters chosen for both cable types are gathered in Table 3.1. Those values are on average the same as the ones given by cables manufacturers on their datasheets [45, 48], found by loss evaluation methods [49] or used in previous simulation reports [47].

Parameter	Unit	$66kV$ (inner cable)	$220kV$ (export cable)
Rated Power	$[MW]$	70	350
Maximum current per phase	$[A]$	615	920
Resistance	$[\Omega/km]$	0.034	0.048
Inductance	$[mH/km]$	0.34	0.37
Capacitance	$[\mu F/km]$	0.29	0.18
Cable cross-section	$[mm^2]$	500	1000

Table 3.1: AC cable parameters (positive and negative sequence).

3.2 HVDC Transmission system

In the Princess Elisabeth Island, a $\pm 525kV$ DC bipolar link is used (see Figure 3.1). Also, a ground cable is added to connect both junctions between power converters, so that the DC connection with the Belgian coast is physically done via 3 cables. This third cable plays a role under faulty conditions, so that the bipolar link can be operated asymmetrically, or used as a monopolar link (cf. Section 3.4). In normal conditions, this ground cable does not carry any current. The assumption of a symmetric use of the monopolar link is done in this work: this third cable is thus not modeled here.

3.2.1 Voltage Source Converter

3.2.1.1 Modeling of Voltage Source Converters

A VSC can be modeled as a controlled voltage source on the AC side and a controlled current source on the DC side. The AC model consists of one phase reactor, composed of a resistance R and an inductance L used to control the direct and quadrature currents, and therefore the active and reactive power as well. This phase reactor also acts as a low pass filter to prevent the propagation of high frequency components of the voltage in the grid.

In the DC model, one capacitor C is located in parallel to the output DC voltage: it acts as an energy buffer to smooth it. Once the current is smoothed, the DC model can be considered as a single, constant DC current source. The global model is depicted in Figure 3.10. This model is suitable to achieve steady state simulation (and also power transients simulations). However, it does not take into account high frequency phenomenons of some kilohertz - due to the opening and closing of IGBT submodules - for short-term simulations.

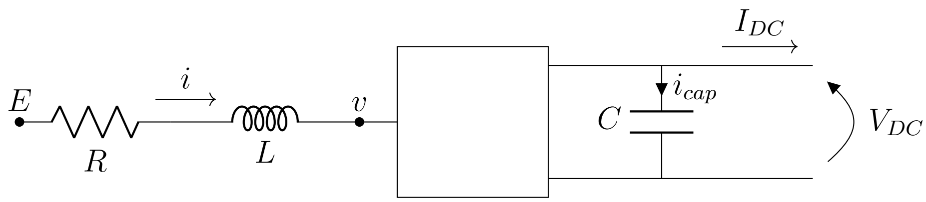

Figure 3.10: Single line diagram of a VSC model.

On the AC side, in the $<a,b,c>$ reference frame, this model is governed by

$$E_{abc} = v_{abc} + Ri_{abc} + L\frac{\partial i_{abc}}{\partial t}, \tag{3.12}$$

where E and v are the phase-to-ground voltages, respectively at the grid and at the converter terminal. The following variables are expressed in per unit.

By applying the *Concordia* and *Park* transforms and by neglecting the homopolar component - as explained earlier -, Eq. (3.12) is now expressed in the reference frame following the pulsation ω of the grid (known as the $<d,q>$ frame):

$$\begin{cases} E_d = Ri_d + L\dfrac{\partial i_d}{\partial t} + v_d - \omega L i_q \\ E_q = Ri_q + L\dfrac{\partial i_q}{\partial t} + v_q + \omega L i_d. \end{cases} \tag{3.13}$$

At node E, the per unit exchanged active and reactive power are described by

$$\begin{cases} P = E_d i_d + E_q i_q \\ Q = E_d i_q - E_q i_d. \end{cases} \tag{3.14}$$

A factor of 3/2 must be added to each term of Eq. (3.14) if conventional units are used.

3.2.1.2 Control of a Voltage Source Converter

The control of a VSC is achieved by four cascade controllers [50]:

1. An external controller with various roles possibles: it can choose the reference reactive power Q at both ends and either the desired DC voltage V_{DC} or the active power to be transferred on the DC link P. The AC voltage E_{abc} can also be controlled instead of the reactive power, but this option is not considered here.

   Typical external controllers are frequency controllers and voltage controllers: their goal is to keep these two quantities as stable as possible. In this work, this external controller is the active power dispatch controller, developed in Section 3.3.

2. An outer controller translates instructions from the external controller into reference currents.

3. An inner current controller controls the current through the phase reactor by adjusting v in Figure 3.10.

4. A close controller gives the right signal to open and close IGBT submodules of the VSC, for example via a Pulse Width Modulation, to obtain the desired v based on the instruction coming from the inner controller.

The overall cascade control is efficient as long as the $n^{th} - 1$ controller acts in a range of time smaller than the n^{th} controller, which is achieved by choosing proportional and integral constants of PI (Proportional-Integral) controllers. Typical values are tens of nanoseconds for the close controller, milliseconds for the inner current controller and tens of milliseconds for the outer controller. The external controller can act in seconds up to several minutes: it depends on the target sought.

Note: in this section, the notation x^* means the reference value of x.

Inner Controller

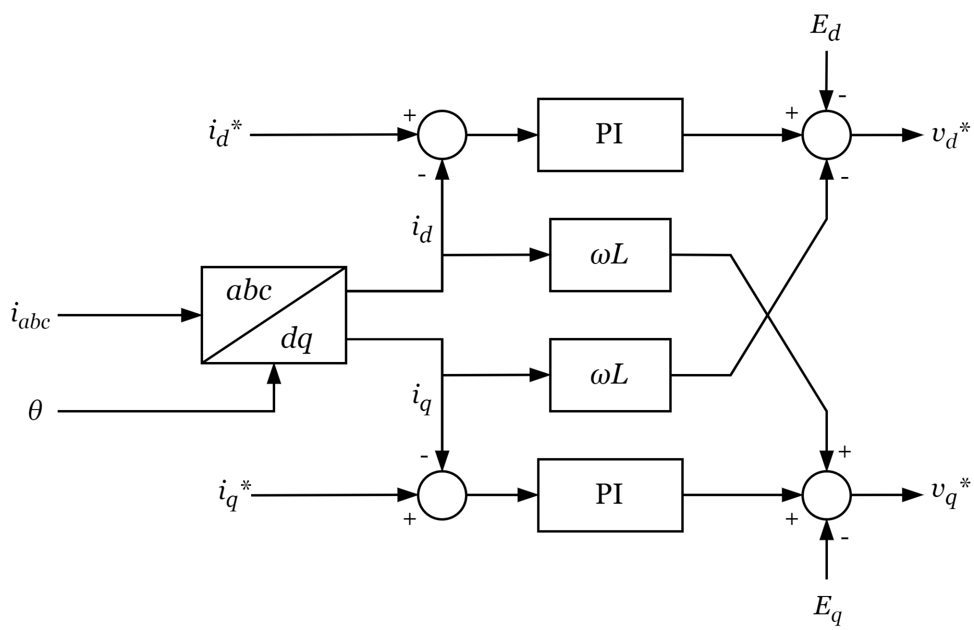

Figure 3.11: Inner current controller of a VSC.

Figure 3.11 shows the inner current controller [51]. Its role is to generate the reference voltages v_d^* and v_q^*. First, the measured current is expressed in the <*d,q*> reference frame, which is achieved using the angle θ. The latter tracks the position of the reference frame. This angle is obtained by a Phase-Locked Loop (PLL), a controller that minimizes the q-component of E such that the voltage is almost in the d-component and $E_q \approx 0$.

Once the measured currents are expressed in direct and quadrature components, they can be compared to their desired references. The error is then sent to a PI controller. Via a feed-forward action, d and q voltage components of Eq. (3.13) are decoupled. At the end, new voltage setpoints v_d^* and v_q^* are given to the close controller.

Outer Controller

The role of this controller is to give reference currents i_d^* and i_q^* to the inner controller. i_d^* is obtained either from a reference active power P or from a reference DC voltage V_{DC}^*, while i_q* comes either from a reference reactive voltage Q, or from a reference AC voltage E^*.

In order to avoid transmitting incoherent instructions to the inner current controller, the output current of any of the following controllers is limited between the acceptable ranges for i_d^* ([0,I_{max}]) and i_q^* ([0,$i_{q,max}^*$]), where I_{max} is the maximum available current under a voltage E, for a defined apparent power S, and $i_{q,max}^*$ is the quadratic current boundary, defined as

$$i_{q,max}^* = \sqrt{(I_{max})^2 - (i_{d,ref}^*)^2}. \tag{3.15}$$

Assuming that the PLL generates the right angle θ, $E_q = 0$ at any time and (3.14) is simplified as $P = E_d i_d$. Considering that E_d does not vary much since it is either maintained by one converter or set by the external grid, the active power only varies with i_d: a PI controller applied on the active power error thus outputs the reference current i_d^* (cf. Figure 3.12).

Similarly, as (3.14) is simplified as $Q = E_d i_q$, the reactive power can be set by tuning i_q. A PI controller applied on the reactive power error yields the reference current i_q^* (see 3.13).

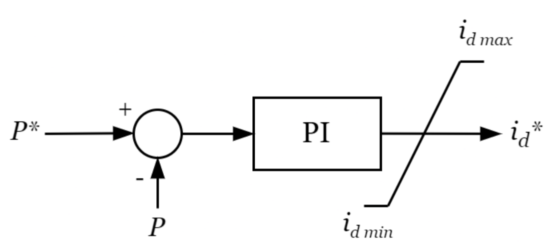

Figure 3.12: Outer controller of a VSC via active power reference.

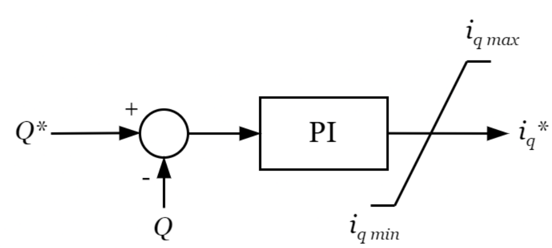

Figure 3.13: Outer controller of a VSC via reactive power reference.

Alternatively, V_{DC} can be set via the controller depicted in Figure 3.14. The power balance equation

$$P_{AC} + P_{cap} + P_{DC} = E_d i_d + V_{DC}(I_{DC} + i_{cap}) = 0 \tag{3.16}$$

links the active power available on the AC side ($P_{AC} = E_d i_d$) with the active power linked to the current i_{cap} absorbed or delivered by the capacitance at a given voltage ($P_{cap} = V_{DC} i_{cap}$), and with the active power to be transmitted via DC cables, $P_{DC} = V_{DC} I_{DC}$. Knowing the relation

$$i_{cap} = C\frac{\partial V_{DC}}{\partial t} \tag{3.17}$$

that describes the capacitance current i_{cap} in function of the DC voltage variation over time, the relation

$$C\frac{\partial V_{DC}}{\partial t} = -\Big(\frac{E_d i_d}{V_{DC}} + I_{DC}\Big) \tag{3.18}$$

is found. It represents the way V_{DC} is controlled by the active current i_d, along with a feed-forward action via I_{DC}. This relation is then linearized around $V_{DC} = V_{DC}^*$ and a feed-forward term $I_{DC}V_{DC}/E_d$ is finally subtracted: this term is obtained from (3.16) in case of no capacitor current, as wished for DC voltage stability [52].

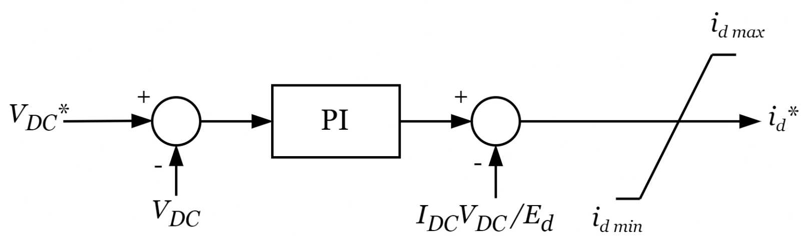

Figure 3.14: Outer controller of a VSC via DC voltage reference.

Finally, the AC voltage magnitude E_{abc} can also be set via the reactive power term Q^*, translated into i_q^*. As mentioned before, considering that the PLL generates an angle such that only E_d defines the magnitude of E_{abc}, the first equation of (3.13) can be used to find Q^*. Due to the active power controller or DC voltage controller, the two terms that depend on i_d are considered as constant. Thanks to the feed-forward terms $i_q\omega L$ and E_d in the inner controller of Figure 3.11, v_d is also constant. Therefore, E_d is proportional to the last term $\omega L i_q$. Since $Q = E_d i_q$, if the reference AC voltage is E_d^*, a PI controller can be applied on the voltage error to output the reference reactive power Q^*, ensuring that E_d reaches E_d^*. The equation

$$E_d^* - E_d \propto \omega L i_q = \frac{\omega L}{E_d} Q^* \tag{3.19}$$

describes these relations, and the resulting controller is depicted in Figure 3.15.

Instead of setting the reference reactive power only via E_{abc}^*, other strategies of control exist, in which the reference reactive power is set at both converters via external controllers, and the AC voltage reference is converted, via the same controller as in Figure 3.15, in an additional reactive power reference ΔQ^* given to the reactive power controller of the converter, where E_{abc}^* is controlled [6, 53].

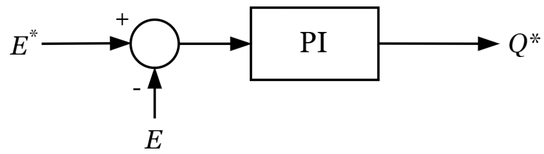

Figure 3.15: Outer controller of a VSC via AC voltage magnitude reference.

The controller in Figure 3.15 does not give the ability to be grid-former, since the frequency is not specified: the latter needs to be inserted as a reference to the PLL which, once integrated, gives the angle θ needed for the *Park* transform.

Since the AC part of the MOG II is always formed (voltage magnitude and frequency are defined) by the external Belgian grid through six cables, it can be considered that no converter with grid-forming capabilities is needed. Indeed, a scenario in which all the six lines are out of service has a probability of almost zero.

For information, a voltage controller with grid-forming capabilities is shown in Appendix A: in that case, both magnitude and frequency can be specified as reference to the controller.

3.2.1.3 Smooth Capacitance Design

The DC output voltage of a VSC contains ripples due to the imperfect nature of the rectifier, even more in case of a two or three-level VSC. Thanks to the smooth capacitance, ripples can be partially reduced: when the output voltage decreases quickly, the capacitance discharges itself so that the resulting voltage is kept more or less constant. Then, once the output voltage is greater than the capacitance voltage, the latter is recharged.

The value of the smooth capacitance can be found by various methods: two of them are presented here. The first is based on the acceptable level of ripples and the second is based on the energy stored in a capacitance.

Considering the DC side of the VSC, the capacitance C_{VSC} can be split in two capacitances in series, each worthing $2C_{VSC}$. Since both positive and negative polarity are smoothed, the analysis can be done on the upper part only.

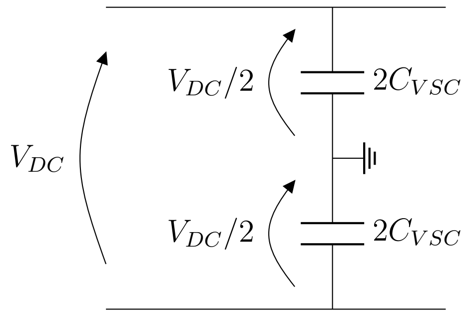

Figure 3.16: Illustration of the smooth capacitances at the DC side of a power converter.

For the ripple method, the capacitance $2C_{VSC}$ is computed based on the acceptable voltage ripple on each voltage polarity ($\Delta V_{DC}/2$), on the period of time during which the capacitance is discharged (Δt) and on the rated current that the capacitance must be able to provide during that period of time. The situation is illustrated in Figure 3.17.

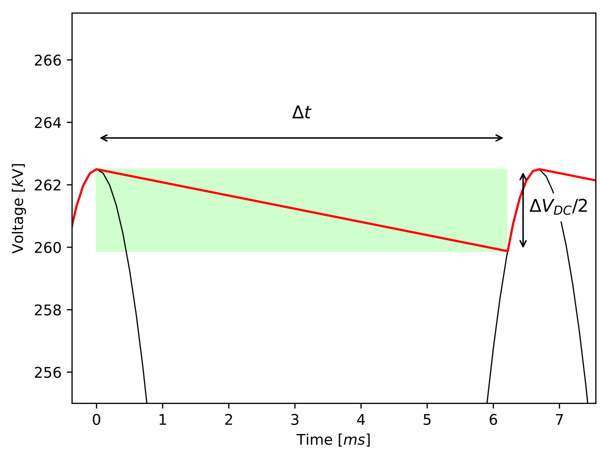

Figure 3.17: Illustration of the variables used to compute the smooth capacitance $2C_{VSC}$ for a ripple $\Delta V_{DC}/2 = 0.99(V_{DC}/2)$.

The equation that links the voltage variation of a capacitance over time with its current can be written as

$$2C_{VSC} = I_{DC}^{max} \frac{\Delta t}{\Delta V_{DC}/2}. \tag{3.20}$$

By making the assumption that Δt is replaced by the period of the rectified signal, *i.e.* the time taken to browse an angle of $\theta = 2\pi/3 \; rad$ at a pulsation of $\omega = 100\pi \; rad/s$, the value of the capacitor is slightly oversized. Also, the smaller the desired ripple, the larger the capacitance.

The rated power per cable is $1GW$: under the rated voltage $V_{DC} = 525kV$, $I_{DC}^{max} = 1.905kA$. By setting the voltage ripple to $\Delta V_{DC}/2 = 0.4\% V_{DC}/2 = 1050V$ during $\Delta t = \theta/\omega = 6.66ms$, the estimated value of the smooth capacitance is found: $C_{VSC} = 5.44mF$.

The second method sets the value of $2C_{VSC}$ based on the rated power P_N to be released and on the discharge time Δt: it is inspired from the thesis of *Georgios Stamatiou* [54]. Under a rated voltage of V_{DC}, the energy stored in a capacitance is $(C_{VSC}V_{DC}^2)/2$. The value can thus be estimated as

$$C_{VSC} = \frac{2P_N}{V_{DC}^2}\Delta t. \tag{3.21}$$

In order to deliver $1GW$ during $6.66ms$, $C_{VSC} = 64.5\mu F$. It must be pointed out that this method makes the assumption of a constant DC voltage with no ripples, which cannot be guaranteed. In a worst-case scenario in which V_{DC} stays at $0.6V_{DC}^*$ - the smallest voltage in absence of smooth capacitance -, this capacitance reaches $145.1\mu F$.

It can be decided that the first method is used to design the smooth capacitance of the VSC that sets V_{DC}^*, and the second is appropriate to set the value of the smooth capacitance of the VSC that sets P^*, since it can rely on a stable DC voltage. In practice, a VSC can switch its controller scheme with the opposite VSC on a DC link, but it cannot switch its capacitance: the $5.44mF$ smooth capacitance should thus be chosen for both VSCs.

3.2.1.4 Pre-Converter Transformers Voltages

Although a certain amount of information about the MOG II is publicly available, AC voltages right before converters are not specified. Knowing the rated DC voltage, it is therefore possible to approximate the pre and post converters AC voltages. The situation is depicted in Figure 3.18.

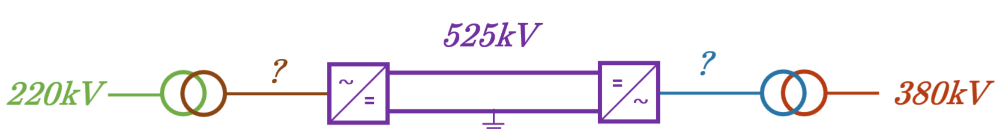

Figure 3.18: Illustration of the missing information about the pre-converter AC voltages The two different colors suggest that these voltages might not be the same in a general case.

For an inverter, the three equations

$$\begin{cases} E_a(t) = \frac{1}{2}V_{DC}(m\cos(\omega t + \delta)) \\ E_b(t) = \frac{1}{2}V_{DC}(m\cos(\omega t - \frac{2\pi}{3} + \delta)) \\ E_c(t) = \frac{1}{2}V_{DC}(m\cos(\omega t + \frac{2\pi}{3} + \delta)) \end{cases} \tag{3.22}$$

describe the relation between the DC voltage V_{DC}, the three phase-to-ground voltages E_a, E_b, E_c, the phase shift angle δ and the modulation index $m \in [0, 1]$ [55] at fundamental frequency. This modulation index can be dynamically adapted, depending on the desired voltage level. It also depends on the topology of VSC used (two or three levels, flying capacitor, type of MMC submodule, ...) and the modulation technique implemented.

There is a link between the modulation index m, the phase angle δ and the outer controllers detailed in Section 3.2.1.2: the reactive power and the AC voltage influence the reference current i_q^* and the active power and DC voltage impact the value of i_d^*. The active power transmitted is defined by the transmission angle δ and the AC peak voltage is limited by the modulation index m. To some extent, it can be shown that m also carries the reactive power reference information, and δ the DC reference voltage.

In order to find peak values, transients are neglected: this means that the *cos* term in (3.22) is neglected, and the DC voltage controller is supposed to keep $V_{DC} = 525kV$, regardless of which converter sets this DC voltage. So, whether the converter is in an inverter or in a rectifier configuration, the phase-to-phase voltage can be obtained via

$$E_{ref}^{RMS} = \sqrt{\frac{3}{2}}\frac{m}{2}V_{DC}, \tag{3.23}$$

where the peak, phase-to-ground voltage is converted to Root Mean Square (RMS) line-to-line voltage.

A modulation index $m = 0.85$ is chosen so that rated voltages can be found at the design point. Considering that the same modulation index is used in both offshore and onshore converters, the pre-converter voltage E_{ref}^{RMS} is $273.27kV$.

It should be noted that the voltage drop along the HVDC cable is neglected: according to the resistance of such a cable (see Table 3.2), at rated current and in steady-state condition, this voltage drop is worth $617V$. The AC voltage should be $272.95kV$ at one end of the HVDC link and $273.27kV$ at the other end: since those values are almost identical, the voltage drop is neglected.

To sum up, transformers in Figure 3.1 just before and after converters are both step-up transformers, considering that the active power flows from offshore to onshore:

the offshore transformer has voltage ratings of $220/273kV$ and the onshore one has voltage ratings of $273/380kV$. Obviously, the modulation index of offshore and onshore converters can be different for AC voltage and reactive power control, leading to other voltages in practice.

3.2.2 DC Transmission Link Model

Similarly to the AC cable, a DC cable can be modeled by a pi-section for power transmission modeling, with the three same lumped parameters per unit length and per polarity (Figure 3.2). Each polarity has its own cable such that two cables are needed to achieve the bipolar transmission link.

As mentioned in Section 3.2.1.2, each converter either specifies the active power to be transmitted or the DC voltage to define i_d^*, and specifies the reactive power or the AC voltage to generate the reference i_q^*. In the present scenario, it is assumed that offshore converters set the active power P^* and onshore converters ensure that V_{DC} is kept constant. Both of them adjust their reactive power according to Q^*. The chosen controller strategy is depicted in Figure 3.19.

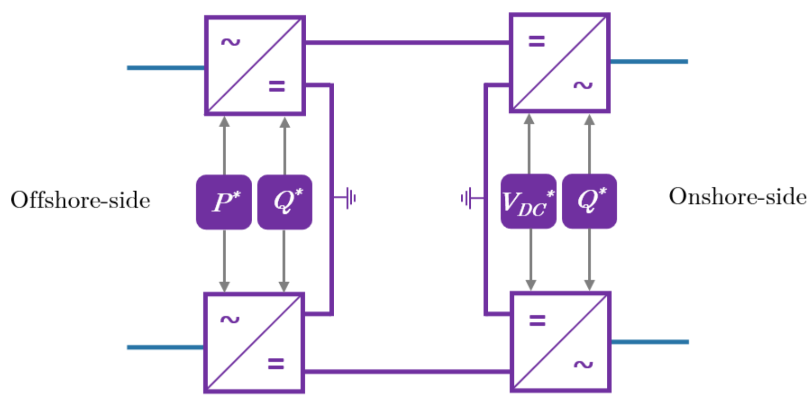

Figure 3.19: Controllers scenario for offshore and onshore converters of the bipolar HVDC link of the MOG II.

The resulting bipolar HVDC transmission system, with both cables and DC models of VSC (*i.e.* DC current sources), is depicted in Figure 3.20.

According to the aforementioned choices, offshore and onshore current sources are respectively controlled by the active power controller and the DC voltage controller detailed in Section 3.2.1.2. Neglecting the feed-forward action of the DC controller, the

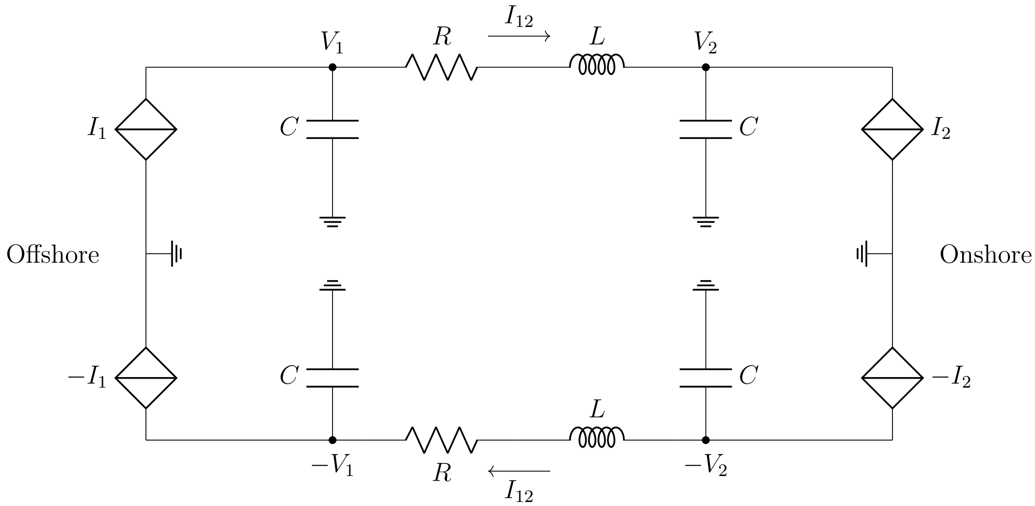

Figure 3.20: Simplified bipolar HVDC transmission model.

two relations

$$I_1(t) = \frac{P(t)}{V_{DC}(t)} \tag{3.24}$$

$$I_2(t) = K_p(V_{DC}^* - V_{DC}(t)) + K_i \int (V_{DC}^* - V_{DC}(t))dt \tag{3.25}$$

describe the action of these two controllers, where K_p and K_i are respectively the proportional and integral constants of the DC voltage PI controller.

As the DC link is meant to export up to $2GW$, thanks to the bipolar topology, the apparent voltage is doubled $(1050kV)$ such that the total power capacity of the link is worth twice the rated power of these cables: the positive polarity cable carries a current I_{12} flowing from the MOG II to the Belgian substation and the negative polarity cable carries a current flowing from the Belgian substation to the MOG II such that the product of both quantities is positive, and the total power is doubled.

3.2.3 HVDC Cables Technical Parameters

Parameters of the pi-section model of the HVDC cable in Figure 3.21, used in the simplified bipolar model, are specified in Table 3.2. These parameters directly come from a cable manufacturer [56]. They are used in simulations done in Chapter 4.

Figure 3.21: Section of a $525kV$ HVDC sea cable. Reproduced from [57].

Parameter	Unit	$525kV$ (export cable)
Rated Power	$[MW]$	1000
Maximum current	$[A]$	1905
Resistance	$[\Omega/km]$	0.0072
Inductance	$[mH/km]$	0.15
Capacitance	$[\mu F/km]$	0.22
Cable cross-section	$[mm^2]$	2500

Table 3.2: DC cable parameters for positive and negative polarity.

3.3 Active Power Dispatch Controller

Since active power can be exported in AC or in DC in the MOG II, the repartition of active power in the hybrid link is one of the challenges brought by this energy island when investigating power transmission. To achieve it, an external controller is developed in this section. Practically speaking, considering a produced power rising from 0 to the rated power of the wind farm, three scenarios exist:

> <u>Scenario 1</u>: Power can be first transmitted fully by DC cable. Once the rated power is reached, the additional power is exported through AC cables.
>
> <u>Scenario 2</u>: Similarly, power can be first transmitted via AC cables, then via DC ones.
>
> <u>Scenario 3</u>: The third scenario consists in exporting power via AC and DC cables as soon as power is produced by the wind farm.

In order to minimize the financial loss linked to the active power losses in the export cables, the criterion chosen to develop the external dispatch controller is to minimize the total active power losses, both in the AC and in the DC link. Under the assumption of a steady state, inductances and capacitances of the bipolar HVDC transmission link model in Figure 3.20 can be neglected: only two resistances R remain. According to the DC current I_{12} flowing in cables, active power losses in the DC link are expressed as

$$P^L_{DC} = 2R(I_{12})^2. \tag{3.26}$$

As depicted in Figure 3.20, each DC current source value is the ratio between the DC power of each offshore VSC, $P(t)$, and the DC voltages V_1 or $-V_1$. Making the hypothesis that the voltage drop across both resistances is identical, since this drop is in opposite direction, the value of $2V_1$ equals $2V_2 = V_{dc} = 1050kV$. Writing the total DC power exported as $P_{dc} = 2P(t)$ and the total active power to be exported as P_T, DC power losses can be expressed as

$$P^L_{dc} = 2R\Big(\frac{P_{dc}}{V_{dc}}\Big)^2 = 2R\frac{(P_T - P_g)^2}{V_{dc}^2}, \tag{3.27}$$

where P_g is the active power flowing through the offshore terminal of the AC link. At rated DC power ($2GW$), $I_{12} = 1.904kA$ and P^L_{dc} reaches $2.35MW$.

In a single-phase AC cable, active power losses can be found by computing the difference between P_G and P_L, the active powers on the offshore and onshore side. As a reminder, in the generator convention, those powers can be expressed as

$$\begin{cases} P_G = \dfrac{V_G^2}{Z}\cos(\theta) - \dfrac{V_G V_L}{Z}\cos(\theta + \delta) \\ P_L = \dfrac{V_L^2}{Z}\cos(\theta) - \dfrac{V_G V_L}{Z}\cos(\theta - \delta), \end{cases} \tag{3.28}$$

where $P_G > 0$ and $P_L < 0$.

Since six three-phase cables are used and busbars are all linked by tie breakers, terminal voltages are the same and total AC powers at both ends are $P_g = 18P_G$ and $P_l = 18P_L$. At the end, the problem can be formulated as

$$min\Big(P_g + P_l + 2R\frac{(P_T - P_g)^2}{V_{dc}^2}\Big). \tag{3.29}$$

The constraints associated with this problem are:

- $0.95 \leq V_G \leq 1.05$ pu: the offshore busbar voltage must stay within an acceptable range of values for operational and power quality reasons. V_G may decrease under $1p.u.$. Since V_L is set by the external grid, and V_G can only increase with the rise of power transmitted, the only scenario in which $V_G < 1p.u.$ is when power flows from the external grid towards the MOG II.

- $0 \leq \delta \leq \delta_{max}$: the transmission angle must also not exceed a certain value δ_{max} to prevent voltage stability issues.

- $0 \leq P_T \leq 3.5GW$: the wind farm produces active power, up to its nominal value.

In practice, δ rises along with V_G when the active power transmitted rises in the AC cable. In the following development, two hypotheses are made:

- δ follows a linear relation with V_G: thanks to data obtained by simulation when increasing the transmitted power in the six AC cables, $\delta(V_G)$ is obtained, as explained in Appendix B.

- V_L is considered as constant and equal to $220kV$, as the onshore busbar is connected to the external grid - that sets the operating AC voltage - through transformers. This hypothesis is even more true with the shunt reactors (cf. Section 4.1).

Figure 3.22 represents the active power losses modeled in the hybrid link, in function of the total exported power P_T and in function of the offshore busbar line-to-line voltage ($\sqrt{3}V_G = V_{GG}$). The two additional curves represent losses in case of a full AC (in green) or a full DC (in red) transmission (up to $2.1GW$ and $2.0GW$ respectively).

It can be observed that losses are the lowest when V_G equals V_L: this result could have also been found analytically, using *Lagrange* multiplier and *Karush-Kuhn-Tucker* techniques. In this situation, $P_l = P_g = 0$ and the transmission is only done in DC. At $2GW$, losses correspond to $2.33MW$, *i.e.* the one predicted by Eq. (3.27). Using only the AC link is apparently not a good idea for the first $2GW$ transmitted, seen AC losses rise higher than the DC ones: they reach $32.4MW$ under $222.37kV$, at $2.1GW$.

Scenario 1 is thus the most favorable in terms of active power losses: in that case, the additional AC losses should increase the total losses to $19.01MW$ at $P_T = 3.5GW$ and a voltage of $221.7kV$ on the offshore busbar.

The VSC could also help in reducing the rise of voltage through reactive power compensation, but this would suggest a reduction of active power (i_d^*) transmissible in DC in favor of a consumption of reactive power (i_q^*), and it is very likely that the reduction of active losses does not even compensate the converted active power into reactive one. So, in steady-state condition, it is advisable not to use the AC voltage controller, such that $i_q^* = 0$.

Finally, in view of the previous observations, the goal of the external controller is

1. to set $P_{dc}^* = P_T$ until $P_T \geq P_{dc}^{max}$
2. to maintain $P_{dc}^* = P_{dc}^{max}$ as long as $P_T \geq P_{dc}^{max}$,

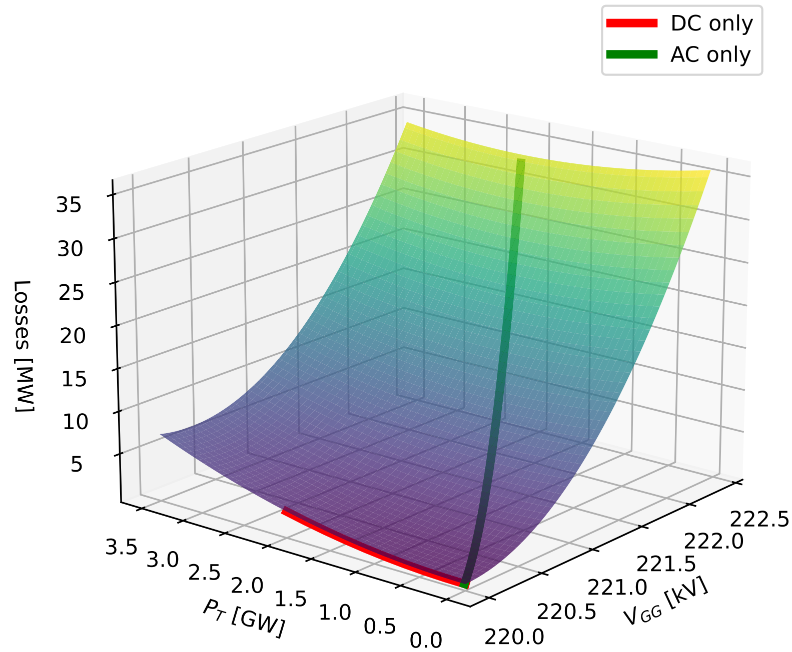

Figure 3.22: Active losses in the hybrid link in function of power exported P_T and offshore busbar voltage V_{GG}, obtained by the analytical losses model. Scenario 1 is thus the most favorable in terms of active power losses.

while keeping $Q^* = 0$.

Practically, the external controller could update its instruction every $15min$, or faster. Meanwhile, if the produced power has risen, AC cables spontaneously carry the additional active power. The controller diagram is depicted in Figure 3.23. It consists of three blocks: one computes the active power flowing in AC cables at the offshore terminal, one keeps in memory the value of active power flowing in AC and DC links, and a last one sets the reference DC power of the VSC.

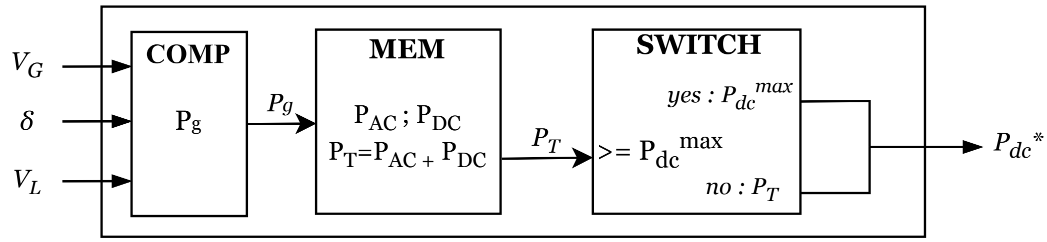

Figure 3.23: External active power dispatch controller diagram.

First, P_g is computed, using Eq. (3.28) and using measurements of V_G, V_L and δ. Then, the value of P_T is updated, through the update of variables P_{ac} and P_{dc} that keeps in memory the amount of power flowing in AC and DC cables. Finally, based on the loading of DC cables, the reference power P_{dc}^* given to the outer controller of the VSC (cf. P^* in Figure 3.12).

As mentioned before, after an increase of the wind power, P_g rises first such that the extra power produced can be detected via measurements. In the memory block, if $P_{dc} < P_{dc}^{max}$, P_{dc} is increased by P_g (or lower if it reaches its maximum). In case $P_{dc} = P_{dc}^{max}$, the memory block sets the value of P_{ac} to P_g.

If the produced power is reduced, P_g may become negative when $P_T \leq P_{dc}^{max}$: in this situation, a part of the exported power is brought back on the offshore side, which creates additional losses in the hybrid link. The faster the controller updates its memory, the shorter the power flows in reverse, the less avoidable losses there are.

3.4 Busbars Topologies and Fault Scenario Analysis

The Princess Elisabeth Island features a modular busbar topology, with various sub-elements and interconnections. It is the result of analysis of different faults and outcomes scenarios that may occur in real life events, with the goal of no - or minimum - power outage and minimal disturbances to other equipment.

This section aims to answer a part of the research question, regarding the robustness of the MOG II. The central rule to be applied to have a reliable, robust and fault tolerant network is the $N-1$ criterion: it states that, in a network consisting of N elements, if one element goes out of service due to a failure or a maintenance, the remaining $N-1$ elements have to accommodate to the change of power flow [58]. The same reasoning can be applied if two or three elements fail in a N-elements network: the rule then becomes a $N-2$ or $N-3$ criterion.

3.4.1 Busbar Types

Before diving into the different types of busbars, two electric components are defined [59]:

- Isolator: device used to isolate two circuits apart. It can only be opened and closed in no-load condition, that is to say when no current is flowing or is likely to flow through the isolator. It is used to protect technicians and equipment when a subcircuit needs to be isolated.

- Circuit breaker (abbr. breaker): safety device that protects a circuit from overloads and faults. Its role is to interrupt the current flow, automatically or manually. The principal component is a switch that can be left in atmospheric pressure or, if equipped with an arc extinguishing system, is immersed in oil, in vacuum, or in sulfur hexafluoride (SF_6). This helps to cool and quench the electric arc generated by the opening of the switch: it is referred to as gas-insulated switchgear (GIS) [60]. When the circuit breaker is automatically triggered, it also features a relay system that detects a current higher than a defined threshold and sends a signal to the switch.

<u>Note</u>: bearing in mind that the Global Warming Potential of SF_6 is 24,300 times greater than that of CO_2, as GIS installations are prone to gas leaks, it is likely that this gas will be used less and less, in favor of vacuum-based or clean air-based solutions, or even a combination of the two [61].

Three main types of busbars exist: the single busbar with single breaker (Figure 3.24), the double busbar with single breaker (Figure 3.25) and the double busbar with double breaker (Figure 3.26). For clarity, isolators are not shown in the figures below: only breakers are displayed, symbolized by a filled square (breaker closed) or an empty square (breaker open).

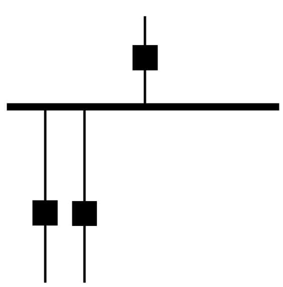

Figure 3.24: Single Busbar with single breaker.

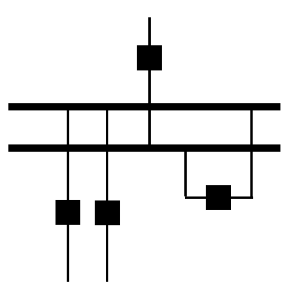

Figure 3.25: Double Busbar with single breaker.

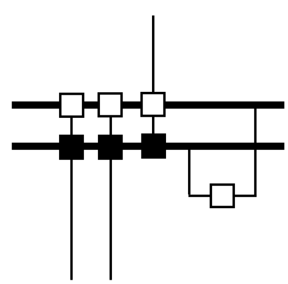

Figure 3.26: Double Busbar with double breaker.

According to the reliability sought, the fault tolerance and the ease of maintenance, one out of those three types is chosen [62]:

- Single Busbar with single breaker: only one busbar connects grid elements together (generators, export cables, subcircuits, transformers, converters, ...), each element with its own breaker and own isolator. It is used in small-scale grids. This is a very simple and low-cost device, but if an element experiences a fault, the lack of redundancy might result in a power outage. Also, if a maintenance is needed, all elements have to be disconnected from the busbar, which often leads to a power outage.

- Double Busbar with single breaker: one main busbar is in parallel with a transfer busbar. Each element is connected to both busbars, but there is still only one breaker per element. Also, there are two isolators per element: one for each busbar. A tie breaker (or busbar coupler) can synchronize both busbars, for smooth transitions from one to the other. In case of a fault on the main busbar, all the breakers are triggered. Then, after isolating the main busbar via isolators, breakers can be closed (except the tie breaker) and the power flow can still be ensured by the transfer bus. In case of maintenance, each breaker also needs to be triggered. In both situations, even if there is a path for the current at the end, a short period of power outage is experienced.

- Double Busbar with double breaker: two busbars A and B are in parallel and connected via a tie breaker. All elements are connected to both busbars, with two circuit breakers and two isolators for each element: one pair of each per busbar. This configuration offers an advanced flexibility, while providing an ease of maintenance. If a fault occurs on one element, its two associated relays detect it and trigger their respective switch: the rest of the circuit is (almost) not affected by the fault, and no power outage occurs. If the fault is located on one of the two busbars, every breakers connected to this line are triggered and the faulty busbar is quickly isolated, so that no power outage is experienced, as currents are redirected towards the other busbar. Finally, for maintenance, one busbar can be isolated the same way as if there was a fault on it. Thanks to redundancy, this topology is very reliable, making it ideal for high-power applications, but it is the most expensive busbar topology among the three covered here.

3.4.2 Modular Offshore Grid II Busbars Topology and Fault Scenarios Analysis

In the case of the Princess Elisabeth Island, double busbars with single breaker and double isolators are used [46]. Additionally, these busbars are divided into four sets of a defined maximum power, and these sets are again divided into smaller subsets of smaller maximum power. The global busbar topology that is to be used in the Princess Elisabeth Island is depicted in Figure 3.27: the orange legend refers to elements with a rated voltage of 66 kV while the green legend refers to elements with a rated voltage of 220 kV, and purple items symbolize DC elements of the HVDC transmission system.

Note: although Figure 3.27 depicts 40 $66kV$ feeders coming from wind parks, a precise cables plan [3] indicates that there should be 50 inner cables for the installed capacity ($3.5GW$), such that each inner cable should carry up to $70MW$, as developed earlier.

The goal of the following faults and outages analysis is to validate or disapprove the $N-1$ criterion of the MOG II. To this end, these scenarios are studied in worst-case conditions: it is considered that the wind farm produces its nominal power of $3.5GW$.

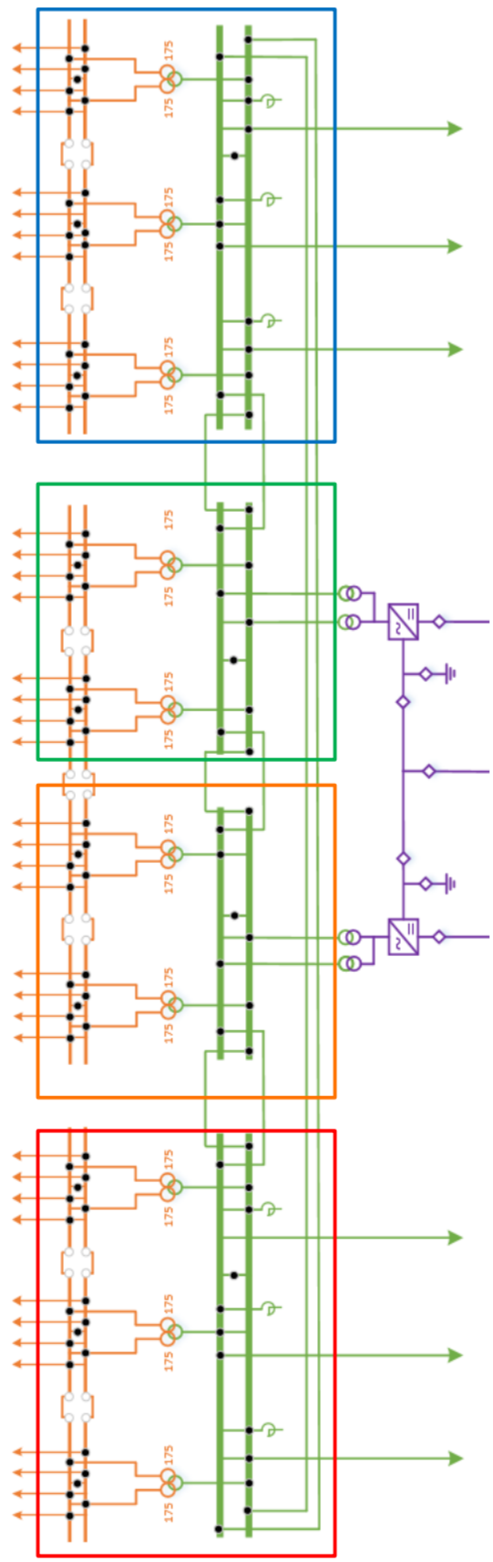

Figure 3.27: Busbars connection scheme of the MOG II. Reproduced from [3].

66kV AC Busbars

Three sets of $66kV$ busbars gather the produced power of the four wind parks. Their rated power are, from left to right, $1050MW$, $1400MW(2\text{x}700MW)$ and $1050MW$. One set consists in three or four double busbars with single breaker, connected together by parallel links, with breakers at each link end. Additionally, three-windings transformers of $400MVA$ [63], with two links per $66kV$ busbar, are connected to $220kV$ busbars, via one connection.

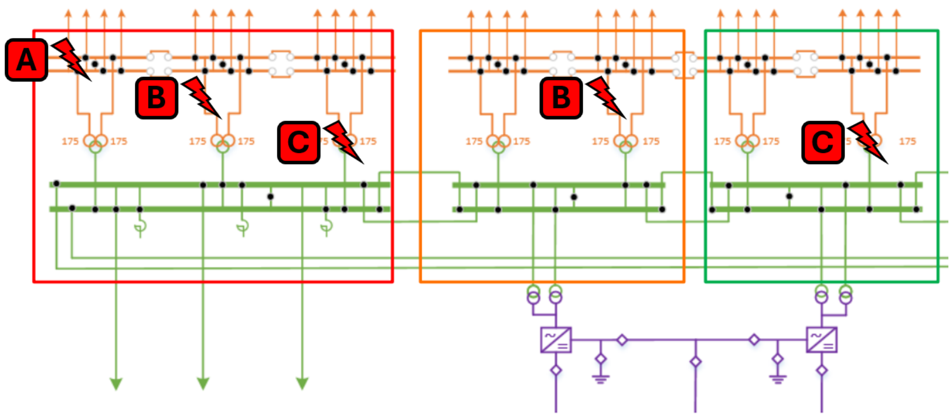

Figure 3.28: Location of faults analyzed on the 66kV part of the MOG II.
Adapted from [3].

Each individual $66kV$ busbar carries a rated power of $350MW$: thanks to the redundancy of this modular topology, the MOG II can overcome failures and the power outage is quite limited. The three faults are referenced in Figure 3.28 and below.

A: If a fault occurs on one busbar, in order to isolate the busbar, circuit breakers must be triggered first, before insulators can be. Then, breakers can be reclosed and power can flow on the parallel busbar. At the end, the loss of a double busbar ($350MW$) is experienced during a short amount of time, after the breakers are reclosed. This short-term outage could have been avoided if double breakers were used.

B: If the fault occurs on one of the two $66kV$ connection of the transformer, $175MW$ have to be redispatch. This can be explained as follows. A three-winding single-phase transformer, with resistances, leakage inductances and magnetizing inductances neglected, is displayed in Figure 3.29.

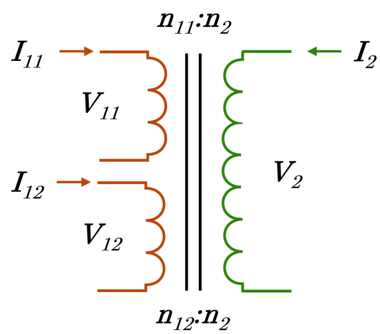

Figure 3.29: Simplified model of a three-winding single-phase transformer. The left side corresponds to the two $66kV$ windings, and the right side to the $220kV$ winding.

The Hopkinson's law, written as

$$\Phi = \frac{\mathcal{F}}{\mathcal{R}}, \tag{3.30}$$

describes the relation between the magnetomotive force $\mathcal{F}$, the magnetic reluctance of the transformer $\mathcal{R}$ and the magnetic flux flowing through the transformer Φ [64].

The magnetomotive force is generated by the two windings on the $66kV$ side. Before the fault, $\mathcal{F} = n_{11}I_{11}+n_{12}I_{12}$, with I_{xx} being the Root Mean Square value of the current. This force is then converted into a magnetic flux through the reluctance. This flux is captured by windings on the $220kV$ side. The link between primary and secondary side currents is

$$I_2 = \frac{n_{11}I_{11} + n_{12}I_{12}}{n_2} \tag{3.31}$$

and the active power on the $220kV$ side is

$$P_2 = V_2 I_2 = V_2 I_{11}\frac{n_{11}}{n_2} + V_2 I_{12}\frac{n_{12}}{n_2}. \tag{3.32}$$

After the fault, no more current flows in one of the two windings, say $I_{12} = 0$. If the two windings on the primary side are identical ($n_{11} = n_{12}$ and $I_{11} = I_{12}$), the available active power flowing through the $220kV$ connection to the busbar is halved. For the three-phase system, this gives $350MW/2 = 175MW$, and half of the transformer is considered as unavailable.

Since the rated power of the transformers used is $400MVA$, depending on the location of the fault, these $175MW$ are dispatched on two and a half or three and a half transformers: in the first case, $125MW$ can be dispatched, and the $50MW$ left will overload transformers up to 105% during the time of the fault clearance. In the second case, the $175MW$ can be easily dispatched without causing any overload.

C: A transformer outage can be experienced if steady-state currents are higher than rated values, which would indicate a degradation of the transformer materials. In that case, the power to redispatch is $350MW$, considering that the whole transformer is out of service. Other transformers will inevitably be overloaded: depending on the location of the outage, transformers will be loaded up to 116% or 132%. If these overloads cannot be withstood during the outage without severe degradations, $70MW$ feeders have to be disconnected.

220kVAC and 525kV DC Busbars

On the $220kV$ side, four double busbars (A's and B's) with single breaker are connected in parallel: busbars A are connected between them, and busbars B are connected between them. Each double busbar carries the power produced by one wind park. Six AC cables are connected to two busbars (three per busbar). The rated power of each cable is $350MW$, which represents a total of $2.1GW$. Each cable has its own shunt reactor connected onto the same busbar [63].

Two converters are connected to the two remaining busbars, via their step-up transformers (two per converter). The rated power of the DC link is $2GW$, which represents $1GW$ per converter maximum, and $500MW$ per transformer at most.

Three HVDC cables connects the Princess Elisabeth Island to the Belgian grid. In the following scenario analysis, the third return cable is assumed to be the same (same voltage rating and current rating) as the two other cables, to ensure an equivalent transmissible rated power in case of monopolar use of the bipolar link.

Neglecting the possibility that the power - flowing into the HVDC link - may have a different origin than the wind farm, the total export capacity ($4.1GW$) exceeds the rated power of the wind farm ($3.5GW$): seen this additional capacity, the redundancy and the interconnections between busbars, it is clear that this topology is designed to ensure the system's ability to re-route power flow in the event of a failure.

Various scenarios can also be analyzed to investigate the connection scheme resiliency. The three faults, referenced in Figure 3.30, are detailed below:

D: If a fault occurs on a busbar A, as for the $66kV$ busbar fault, breakers are first triggered to isolate that busbar. Then, after isolators are opened, breakers can be closed and the power flows on busbar B: there is a power outage of either $700MW$ or $1050MW$ during a short time (some milliseconds), depending on the faulty busbar location. But, in the end, no power outage is experienced.

E: If a fault occurs on an export cable, this latter is disconnected from the two busbars thanks to the automatic relay that triggers the single breaker, and $350MW$ (at most) need to be dispatched:

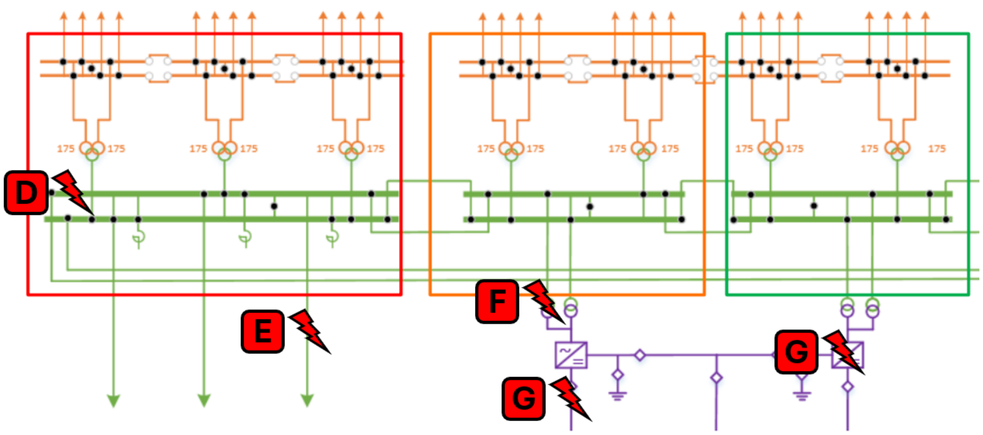

Figure 3.30: Location of faults analyzed on the 220kV and DC part of the MOG II. Adapted from [3].

1. if AC export cables are fully loaded, thanks to the parallel interconnection of busbars, these $350MW$ can reach the two converters, where the reference power P^* of both converters can be increased by $175MW$ each, which increase the transferred power from $700MW$, initially, to $875MW$ per cable: this new operating condition is acceptable, as the rated power is $1000MW$ per cable.

2. if the DC transmission link is already transferring its maximum power capacity, the initial $250MW$ of the faulty cable spontaneously spreads over the five remaining cables, which represents an additional power of $50MW$ and a total of $300MW$ per cable., which stays below the $350MW$ rated power.

3. in any in-between scenario, the solution is a combination of the two previous.

F: If one pre-converter transformer goes out of service ($500MW$ at most), the only solution is to operate the bipolar link asymmetrically:

1. If the DC link is loaded at 100% ($2GW$) and if the converter connected to the faulty transformer is put out of service, $1GW$ needs to be transported by AC cables, initially loaded at $1.5GW/2.1GW$, which would overload AC cables. If both converters keep running but at the same power level ($P^* = 500MW$), $1GW$ should also be carried by AC cables. In both scenarios, neglecting the possibility of a large overload in AC cables, there would be a power outage of $400MW$.

   Now, if the two converters do not have the same power reference ($500MW$ and $1000MW$), only $500MW$ need to be transported via AC cable, which would increase its exported power to $2.0GW/2.1GW$: this solution prevents from overloading AC cable by making use of the HVDC return cable. In this specific scenario, since the DC voltage is kept constant, one of the two offshore current sources of Figure 3.20 delivers half the current of the other one, and the return cable carries the other half.

2. In the case of fully loaded AC cables, the loss of one pre-converter transformer requires to re-route $350MW$. Since these transformers are limited to $500MW$, it is not possible to transfer the same power through both converters. One solution is to load the transformer next to the faulty one to its maximum, and to dispatch the remaining $200MW$ on the two other transformers: they are now loaded at $450MW/500MW$, which is acceptable. But, in any case, the solution ends up in an asymmetric use of the bipolar link.

G: If a fault occurs on a converter or a HVDC cable, a power outage of $400MW$ would occur, as AC export cables and the monopolar link (HVDC cable and return cable) cannot carry more than $3.1GW$. Here, the solution would be to overload AC cables: if not possible, a few $66kV$ feeders of $70MW$ should be disconnected, which results in a power outage.

With the topology chosen by *Elia*, if transformers and cables overloading is not possible, it cannot be concluded that the $N-1$ criterion is fulfilled, and more specifically due to the last scenario analyzed, in which there is an unavoidable power outage of $400MW$. This conclusion answers a part of the research question about the robustness assessment of the MOG II.

However, it has to be noted that this last event only happens on two types of elements, in the scenario of a rated wind power produced, and represents a power outage of a small part of the total exported power. The occurrence of such a scenario can be estimated as follows. It can be considered that the mean time between failure (MTBF) of a VSC is 0.5 per year (*i.e.* once every two years)[65], and that there is a power outage if the produced power is above $3.1GW$. If the estimated probability to reach a produced power between $3.1GW$ and $3.5GW$ power is 30% of the time (see Appendix C), and if the failure event of the VSC is uncorrelated with the produced power, over one year, the estimated probability of reaching a power outage between 0 and $0.4GW/3.5GW$ is

$$p = p_{rated\,power} * p_{converter\,fault} = 0.3.exp(-1yr/0.5) = 4\%. \tag{3.33}$$

Overall, expressed in MTBF, this outage due to a fault event might occur once every three years. As mentioned, this figure is obtained under the assumption of the independence between the failure rate and the level of produced power, which cannot be certified. Also, it is already established that the occurrence of a power outage due to the VSC will be more frequent, and the power outage will be more important, but it will be caused by the annual maintenances planned by *Elia* (8 days per year for maintenance of offshore and onshore converters [12]).

A way to fulfill the N-1 criterion would be to add either two AC export cables (to export $400MW$) - although it is shown in Section 2.4.3 that this is not feasible - or to add another $2GW$ HVDC transmission link, which is already planned by *Elia*. Also, the use of double busbars with double breakers would prevent very short power outages, caused by the switch between the main and the transfer busbar.

3.5 Wind Farm

In Chapter 2, a steady-state model of a wind turbine is introduced. This model is valid for a Type 3 or a Type 4 wind turbine.

In this section, a dynamic wind turbine model of Type 4 is introduced. This model can be used to simulate power transients: since it is not used in the frame of this work, the dynamic model is for guidance only. Also, the $3.5GW$ wind farm model (wind turbines and collect cables) is detailed: this model is then used in Chapter 4.

3.5.1 Wind Turbine Model in *DIgSILENT PowerFactory*

This section introduces a model of Type 4 offshore wind turbines, suitable for power transient simulations (from $100ms$ to tens of minutes), since Type 3 offshore wind turbines are less and less used.

As a matter of fact, in the last decade, the part of Type 4 wind turbines in the new offshore wind turbines installations seems quite greater than Type 3. This can be motivated by the advantages of PMSG (Type 4: no excitation system, no gearbox, low losses, reliability) compared to DFIG (Type 3) . Thus, for wind turbines with power ratings of several megawatts - like offshore wind turbines -, PMSG are preferred to DFIG [66, 67]. This trend can be suggested by the following examples. Each new offshore wind turbines of the Belgian North Sea are PMSG since 2013 [68]. In France, the recent 2022 Saint-Nazaire wind park consists in 80 $6MW$ *GE Haliade 150*, which are all PMSG [69]. Actually, no recent European wind parks using new Type 3 wind turbines was found.

In PMSG wind turbines, all the produced power is converted through a full-scale VSC: this allows the use of PI controllers to model the dynamic of the system. The idea is to apply the global controller in Figure 3.31 on a static generator so as to emulate the dynamic of a real wind turbine, with its inertia, its MPPT controller and its blade pitch angle controller. This model is highly inspired from an example available in the library of the *DIgSILENT PowerFactory* software [70].

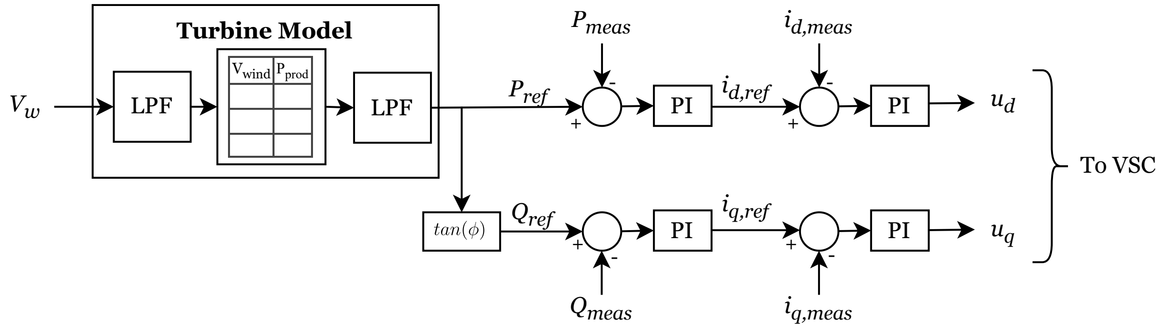

Figure 3.31: PMSG Controller used in the dynamic Type 4 wind turbine model. Inspired from [70].

First, the wind speed is filtered so as to only consider low frequencies variations: wind turbines act as low-pass filters for the wind speed, with a filter time constant T_w. Through a lookup table, the corresponding reference active power is outputs. In order to take into account the action of controllers (MPPT and blade pitch angle control), a low-pass filter block of time constant $T_{control}$ is added. The transfer function of these two low pass filters is

$$\frac{1}{1+sT}. \tag{3.34}$$

Then, based on a constant $cos(\phi)$ mode, the reference reactive power is obtained, based on the reference active power. Here, ϕ is considered as 0 such that no reactive power is produced.

Measurements of the active and reactive power at the wind turbine output allows to process the error through two PI controllers, with K_P and T_P as proportional gain and time constant for the active power controller, and K_Q and T_Q for the reactive power controller. The transfer function of such proportional-integral controllers is:

$$K\left(1+\frac{1}{sT}\right) = K + \frac{K/T}{s}. \tag{3.35}$$

These controllers output the direct and quadrature reference currents, as explained in Section 3.2.1.2. Measurements of currents on which *Park* and *Concordia* transforms are applied (via a PLL) are used to compute the error with the reference currents. Two PI blocks are used to compute the direct and quadrature voltages that the VSC has to generate: in this case, feed-forward and decoupling terms are not taken into account. Constants of these PI controllers are K_{id}, T_{id}, K_{iq} and T_{iq}. This outputs the final voltage that the VSC has to produce.

As mentioned before, this model is highly inspired from an example of DIgSILENT project of a $15MVA$ wind turbine [70]. Since wind turbines connected to the MOG II should have a power between $14MW$ and $18MW$ (see Section 3.1.4), time constants and gains of controllers used to model the latter are considered to be similar to the ones of this example, under the assumption of equivalent inertia and controller performances. They can be found in Table 3.3.

Variable	Value	Unit
T_w	1	s
$T_{control}$	3	s
K_P	0.5	/
T_P	40	ms
K_Q	0.5	/
T_Q	10	ms
K_{id}	1	/
T_{id}	2	ms
K_{iq}	1	/
T_{iq}	2	ms

Table 3.3: Parameters of the controller of the static generator for a Type 4 wind turbine.

3.5.2 Wind Farm Model

Based on the wind model developed in Section 2.5.1 and either the steady-state wind turbine model detailed in Section 2.5.2 or the dynamic one presented in Section 3.5.1, an aggregated model of a wind farm can be derived.

It is assumed that the wind model $v_w(t)$ is the same for each wind turbine, regardless of the spatial distribution of the wind speed above the sea. This means that a variation in the wind speed vector field reaches every wind turbine instantaneously, as if there was no distance in between. This hypothesis is made in order not to consider the impact of turbulences and other variations of the axial wind speed on a single wind turbine, caused by the presence of other wind turbines.

Simple wind farm connection schemes used in simulations can be string-like (cf. Figure 3.32) or star-like (cf. Figure 3.33).

On the other hand, real-life wind farms often connect their wind turbines in a hybrid star-of-strings way: each wind turbine is connected to an inner array cable (string) and several arrays of cables are connected to an offshore substation (star). Secondary arrays can also be connected to a main string, or even tertiary and quaternary arrays. For example, the 2015 *Gwynt y Môr* Welsh offshore wind farm uses that hybrid topology (see Figure 3.34). This star-string topology provides an efficient use of undersea cables regarding the trade-off between cable distance and power rating to be carried: a single string connecting all wind turbines would require an enormous power capacity but

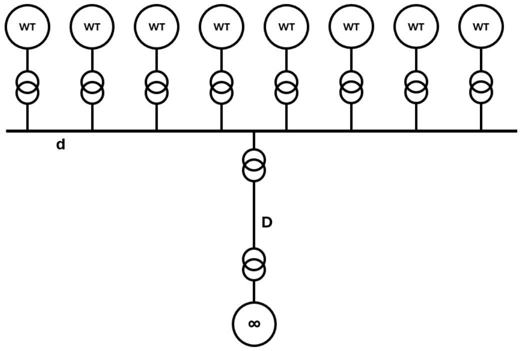

Figure 3.32: String connection topology.

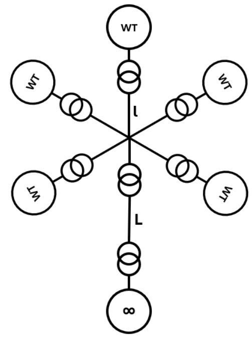

Figure 3.33: Star connection topology.

would be efficient in terms of distance, while many individual cables between each wind turbine and a central offshore substation would be inefficient in terms of distance, although the power to be carried would be very small.

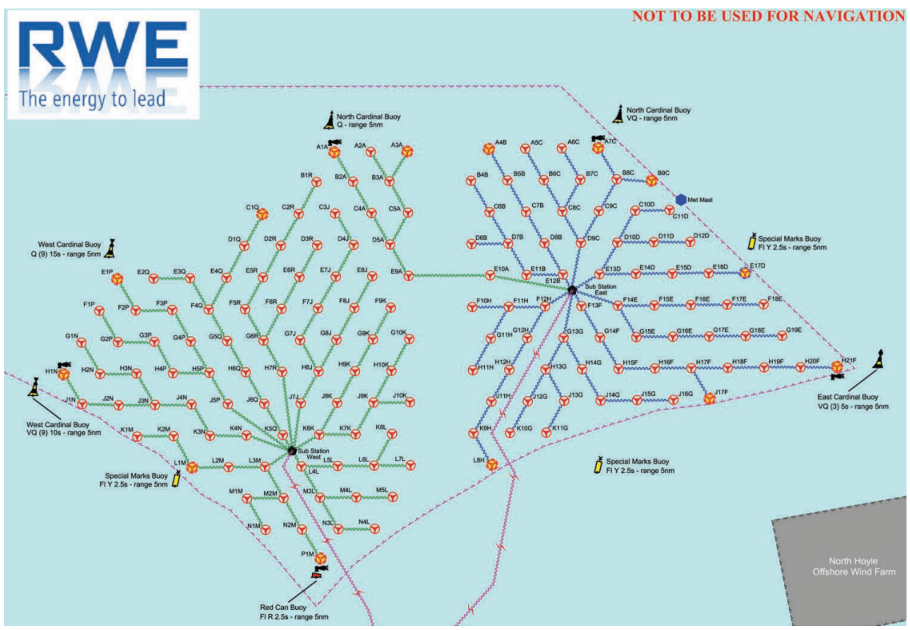

Figure 3.34: Star-string connection topology of the *Gwynt y Môr* wind farm. Reproduced from [71].

The wind farm model used in the global electrical system uses the star connection topology. It is mentioned, in Section 3.1.4, that four to five wind turbines are connected to one string, reaching a rated power of $70MW$ near the point of connection. These wind turbines are first gathered in one $70MW$ wind turbine, with the same dynamic behavior of each individual wind turbine.

Practically speaking, in the MOG II, the length l of an inner cable string ranges from $4km$ to $19km$, and the carried power increases while getting closer to the Princess

Elisabeth Island. Since only one $70MW$ generator is considered per inner cable, the latter must have a smaller length than the real one, in order not to overestimate active power losses and reactive power production.

Furthermore, sets of five cables of the same length are placed in parallel and modeled as one equivalent cable. The five $70MW$ identical generators - initially connected to each inner cable - are modeled as one big $350MW$ generator, connected to the equivalent cable.

At the end, ten $66kV$ cables of $350MW$ (each with an increasing length from $4km$ to $13km$) are connected to three $66kV$ busbars, as depicted in orange in Figure 3.35. The rest of the system is modeled according to the detailed information published by *Elia*, as detailed throughout this section: only three-windings transformers are considered as two-windings, which does not affect steady-state simulations.

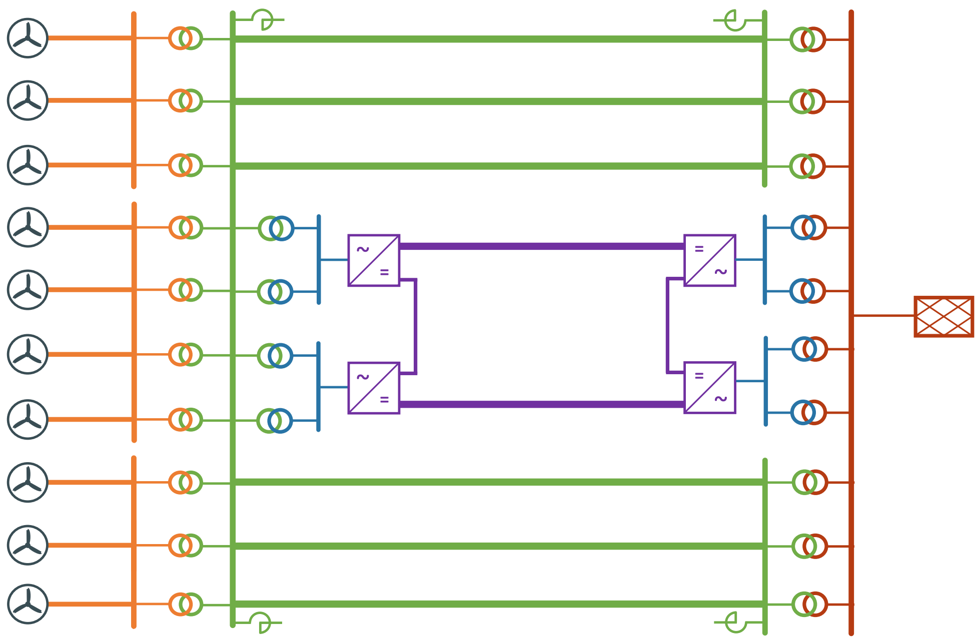

Figure 3.35: Wind farm model integrated into the MOG II.

3.6 Summary

In this section, the AC and DC transmission links are modeled (along with the shunt reactors), as well as the wind farm model. An active power dispatch controller is also developed, and fault scenarios analysis are made to assess the theoretical robustness of the MOG II.

From the three pi-sections used to model AC cables, equations of the active and reactive power at both cable ends are found. They are used to quantify and design the shunt reactors, based on a zero reactive power produced: these shunt reactors are tested under three scenarios in Section 4.1. Then, the maximum active power transmissible on an AC cable is studied: it is caused both by the increase of the cable resistance - due to the skin effect - and by the capacitive currents. Technical parameters of the pi-section are also given for both $66kV$ and $220kV$ cables.

In the DC transmission link, one cable is modeled by a pi-section: its corresponding parameters are given. The voltage source converter is also modeled, along with its controllers. Two ways of designing the smooth capacitance are introduced: the energy-based method - that gives more realistic results - and the ripples-based one. The pre-converter AC voltage is also found so as to specify it in the global model used in simulations.

The active power dispatch controller gives priority to the DC cable loading, with the aim of minimizing active power losses: this result is obtained based on the model of both AC and DC transmission links. It then gives an active power reference to the VSC, and updates this reference based on the voltage measurements at both ends of export cables, and based on the computation of the transmission angle. The effectiveness of this controller is assessed in Section 4.2.

The MOG II topology of *Elia* is evaluated from the robustness point of view. The $N-1$ criterion cannot be fulfilled because of two critical grid elements: the VSC and the DC export cables. In order not to overload AC cables too much, generation units must be taken out.

Finally, a model of a wind farm is presented. This model can be used in steady-state (which is the case in the scope of this work) or used for power transient simulations. It consists of a wind model with four components, a PMSG wind turbine model using VSC and PI controllers, and an aggregated model for all wind turbines and inner cables.

Chapter 4

Validation of the Shunt Reactors, the Active Power Dispatch Controller and the Wind Turbine Model

In the previous chapter, the global grid model is developed, through analytical models. Also, a shunt reactor is presented, as a solution to the reactive power issue. The robustness of the MOG II is assessed theoretically, and an active power dispatch is developed with the aim of minimizing Joule losses. Last, in Chapter 2, a simplified wind turbine model is proposed: the latter can be used in the wind farm model to represent the steady-state generation units connected to the MOG II.

This section focuses on the answers of two elements of the research question, which are the validation of the strategy of the active power dispatch controller - with the aim of a minimum global active power loss - and the verification of the solution brought to the capacitive effect issue of cables, *i.e.* the use of shunt reactors to mitigate the reactive power produced. Also, the accuracy of the steady-state, simplified model of a wind turbine is evaluated, via the comparison of its generated power with an existing wind turbine power curve.

For information, the HVDC transmission link, used in the following simulations, is based on a half-bridge MMC (cf. Figure 2.10). Parameters used in the MMC model are listed in Table 4.1: these are the per default values proposed by the *DIgSILENT PowerFactory* software.

Variable	Value	Unit
Number of submodules per arm	200	/
Submodule capacitance	1000	$[\mu F]$
Arm resistance	0.006	$[\Omega]$
Arm inductance	60	$[mH]$

Table 4.1: Parameters used in the MMC of the HVDC transmission system.

4.1 Impact of Shunt Reactors on the Modular Offshore Grid II

A method to approach the value of inductances of the shunt reactors is presented in Section 3.1.3, where the reactive power is completely canceled. In order to define shunt values at the design point, a base scenario and a defined network are needed: both are displayed in Figure 4.1. Three $220kV$ AC export cables (in green) are considered, with three wind parks of $350MW$ each: the total active power transferred is $1050MW$. The generated electrical power is carried via five $4km$, five $8km$ and five $12km$ $66kV$ AC inner cables (in orange): those lengths were arbitrarily chosen to take into account the real length variations. Finally, a wind speed of $17m/s$ is chosen such that the rated power of the wind park is produced.

Note: the design point scenario could have been chosen at a produced power smaller than the rated one, such that the reactive power to be compensated would have been smaller, and such that VSCs could have either produced or consumed reactive power around the value of the reactive power compensated by the shunt reactors.

The total reactive power to be compensated is the sum of the one at the generator side (Q_G) and the one at the load side (Q_L). This compensation should reduce the offshore busbar voltage and the line current, which would limit the active power losses. Three scenarios of repartition are tested:

- Scenario 1 considers a shunt only at the load side that consumes $Q_G + Q_L$ (0/100).
- Scenario 2 consists in the same reactive power consumed at the generator side only (100/0).
- Scenario 3 investigates an equal repartition of $(Q_G + Q_L)/2$ at each side (50/50).

In order to test these scenarios, the reduced grid in Figure 4.1 is implemented in *DIgSILENT PowerFactory*, in which cable models are exactly the same as the analytical model of the cable, introduced in Section 3.1.

The goal of the following simulation results is both to compute variables needed for

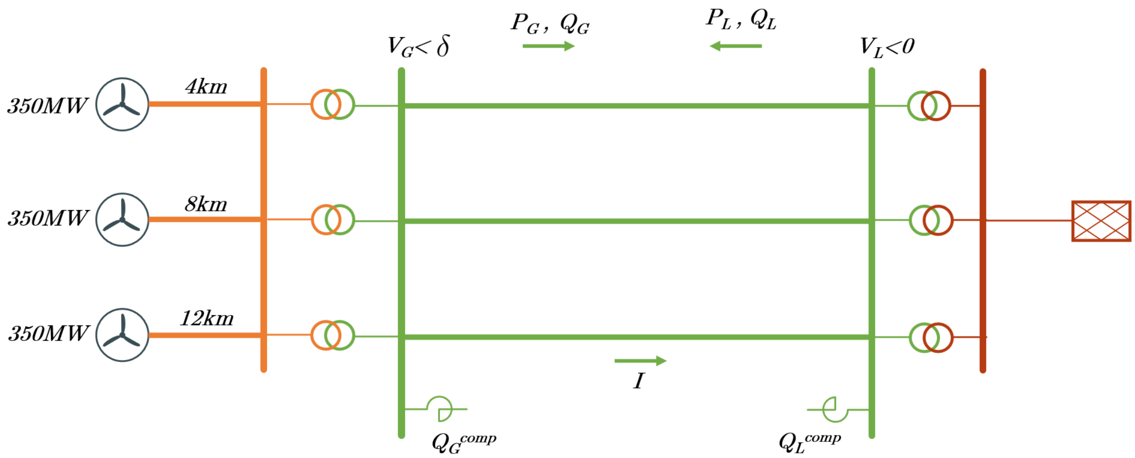

Figure 4.1: Part of the MOG II considered for the shunt reactors assessment, with measured variables. Orange cables are the 4, 8 and $12km$ $66kV$ inner cables, green cables are the $220kV$ export cables and the red busbar has a rated voltage of $380kV$.

the analytical model of the active and reactive power in a cable (Eqs. (3.4), (3.6) and (3.8)), and to validate this analytical model, using these computed variables. Active and reactive powers are estimated, based on the same voltages and transmission angles obtained by the simulations. Also, the same $220kV$ cable parameters are used. The obtained results are displayed in Table 4.2, in which line-to-line voltages V_{GG} and V_{LL} are specified instead of phase-to-ground voltages V_G and V_L. Also, "Sim." refers to the results obtained by the simulation of the analytical model, and "Model" refers to the results computed from the analytical model.

	Base scenario		Scenario 1		Scenario 2		Scenario 3	
Variable [Unit]	Sim.	Model	Sim.	Model	Sim.	Model	Sim.	Model
Q_G^{comp} [MVAR]	0		0		-351.6		-178.1	
Q_L^{comp} [MVAR]	0		-345.7		0		-172.8	
V_{GG} [kV]	226.8		224.7		221.8		223.2	
V_{LL} [kV]	222.0		219.9		219.8		219.9	
δ [°]	1.9		2.0		2.3		2.1	
Q_G [MVAR]	-8.1	-13.7	-6.3	-2.4	-3.9	-5.4	-5.1	-26.1
Q_L [MVAR]	354.1	359.7	-1.2	-12.6	-15.1	-14.42	-9.3	-35.4
P_G [MW]	-1045.8	-1043.5	-1045.5	-1068.9	-1045.5	-1056.3	-1045.5	-1036.8
P_L [MW]	1029.8	1027.7	1029.5	1052.1	1029.2	1039.65	1029.8	1021.3
I [A]	944	/	950	/	956	/	914	/

Table 4.2: Simulation and model results of reactive power compensation scenarios. Reactive powers effectively compensated at shunts slightly differ from the one given as instruction to the shunt compensators: this explains the values of Q_G^{comp} and Q_L^{comp}.

The goal of these shunt reactors is to consume the reactive power produced by capacitances of cables, such that the offshore busbar voltage is reduced, and to reduce the capacitive current in such a way that the line current is reduced, and the active power losses decrease. Eventually, thanks to the shunt reactors, the cable current should be below the rated current ($920A$). Also, as depicted in Figure 2.4, these shunt compensators should be able to extend the acceptable cable length through the reduction of the line current and the reduction of the active power losses. However, because of the small length of the export cables, the active power received P_L should not vary much with the line current variations.

The base scenario shows that both terminal voltages are higher than the rated one. Seen that the current flows from node G to node L, V_G is greater than V_L, and δ is positive. According to the reactive power equations in (3.4) and in (3.6), in Q_G, the V_G^2 term is almost compensated by the $sin(\theta + \delta)$ term and by the reactive power produced by the capacitance. At the opposite terminal, Q_L is far from being negligible: since the V_L^2 term is smaller than the $sin(\theta - \delta)$ term, the additional reactive power term linked to the capacitance increases the total reactive power. It can be noted that the reactive power generated by capacitances (*i.e.* the last term in Eqs.(3.4) and (3.6)) are almost the same at both cable ends. So, the fact that Q_L is greater than Q_G is explained both by the increase of voltage and the value of the transmission angle: at the generator side, the reactive power produced by capacitances helps to reduce the net reactive power Q_G, and at the load side, the same reactive power generated by cables worsens the net reactive power Q_L.

This explanation is confirmed both by the simulation and the computed model results. It can be supposed that the reactive power at node G is actually the result of the one produced by the $66kV$ inner cables, and partially consumed by transformers. Generators are controlled in such a way that their output reactive power is zero: if the export cables had directly been connected to generators (no inner cables), Q_G should have probably been zero.

The three scenarios show that, on one hand, voltages, transmission angles, currents and reactive power are all affected by the presence of shunts. Active powers, on the other hand, are almost identical in every scenario, whether obtained by the simulated model or by the manually computed analytical model.

Active power losses are indeed caused by the line current magnitude and by resistive elements of the cable line: both do not change much with the presence of a shunt reactor. The difference between active powers obtained by simulation and by the analytical model can be explained by the precision of the transmission angle: due to the active power losses in the $66kV$ cables, for the three scenarios, the available active power P_G should be limited to $-1045.5MW$. In Scenario 1, this power reaches $-1068.9MW$: it should be noted that the transmission angle given as input could have been more precise, such that computed powers might have been closer to the ones obtained by simulation.

For example, in this Scenario 1, if $\delta = 1.95°$ (the smallest angle that, once rounded at the top, gives $2.0°$), P_G and P_L are respectively $-1047.53MW$ and $1031.31MW$, which is more realistic. It can be deduced that the knowledge of cable parameters, voltages and transmission angle enables to precisely approximate active and reactive power, as long as model inputs (especially the transmission angle) are sufficiently accurate.

Scenario 1 shows that compensating reactive power at the node L, where the greatest reactive power is produced, is efficient only for the voltage at that node, and results in a minimum global reactive power. The loadflow establishes itself - with the new reactive powers - in such a way that the resulting voltage V_{GG} is still higher than the rated voltage, and is also higher than V_{GG} in other scenarios. Also, compared to the base scenario, the current is slightly higher: this can be explained by the variation of the transmission angle and, to a lesser degree, by the difference in voltage magnitude, as described by Eq. (3.1).

In terms of voltage level, Scenario 2 shows the best performances, but the line current I is the greatest of all scenarios. Thus, seeking that the voltage level is the closest to the rated one does not guarantee an acceptable current value.

A compromise between acceptable voltage levels, current values and global reactive power is Scenario 3, in which the current is below the rated one and the active power transmitted to the grid (P_L) is the same as in the base scenario. In such a scenario, the value of each phase inductance can be estimated via Eq. (3.10): it reaches $2.26H$, which is slightly greater than the inductance value that generates the resonance with the capacitance, *i.e.* $1.25H$. This observation was expected, as the additional reactive power to be compensated via the shunt reactors increases a little bit the corresponding value of the inductance L_{sh}, as shown in Eq. (3.9).

Since the best results are obtained via the 50/50 repartition, the part of the research question, related to the solution found to the capacitive effect issue of the cable, is now answered.

In the global model of the MOG II (see Figure 3.35), the system in Figure 4.1 is duplicated and $220kV$ onshore and offshore busbars are supposed to be interconnected. Additionally, there are four extra generation units, thus more inner cables. Due to the presence of these additional inner cables, the reactive power Q_G might increase a little in the global system, but in a reasonable range. Also, since the additional power is evacuated through DC cables, no reactive power is generated in these export cables such that Q_L should, at most, double.

4.2 Accuracy of the Active Power Dispatch Controller Strategy

In Section 3.3, the active power dispatch controller is developed, based on the analytical model. In order to minimize active power losses, it was shown that the controller needs to first load the DC cable up to its rated power, then to load the AC cable. In this section, losses obtained by the computed analytical models and by simulations of these models are compared to validate the fact that the DC link should be used first. The grid model used to obtain the following results is the one depicted in Figure 3.35, with the same shunt reactors compensation scheme as in Scenario 3, *i.e.* a 50/50 compensation (see Section 4.1).

Figure 4.2 is a comparison of line-to-line voltages V_{GG}, V_{LL} and AC losses P_{LOSS}^{AC}, between results obtained by the manually computed analytical model ("model") and obtained by the simulation of this model ("simu"), while increasing the transmitted power P_L in the AC link. The software used is *DIgSILENT PowerFactory*. This model estimates P_L and P_G based on a constant V_{LL}, on an increasing V_{GG} and on the $\delta(V_{GG})$ characteristic obtained from the simulation (see Appendix B). It is observed that active power losses obtained by the simulation match the ones obtained by the model, although voltages are not the same.

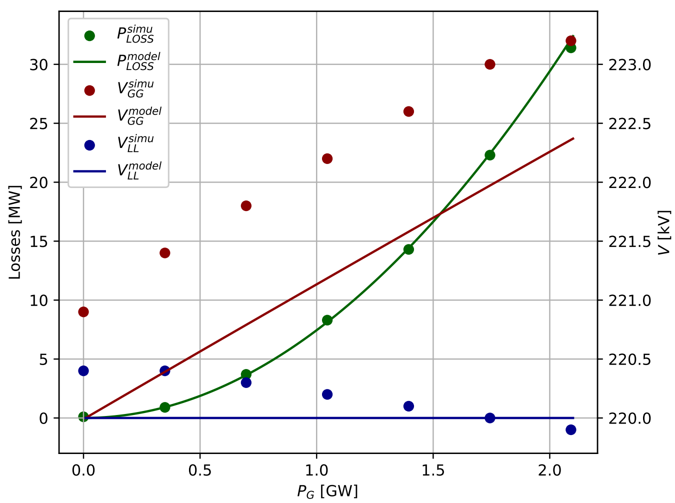

Figure 4.2: Comparison of P_{LOSS}^{AC}, V_{GG} and V_{LL} in function of P_G obtained by the manually computed analytical model (Eqs. (3.4) and (3.6)) (referenced as "model") and by the simulation of this model (Figure 3.2) (referenced as "simu").

It has to be noted that V_{GG} used in the analytical model and in the simulation have the same slope but differ by an offset of $0.8kV$. This can be explained by the fact that $\delta(V_{GG})$ used in the model is a linearization of the data obtained by simulation, when increasing P_G. In these data, at $P_G = 0$, a zero transmission angle δ corresponds to $V_{GG} = 220.8kV$, which is greater than the rated voltage. In order to match the equations of the analytical model, $\delta = 0$ and $P_G = 0$ has to correspond to $V_{GG} = 220kV$ (see Eqs.(3.4) and (3.6)).

When developing the controller, the hypothesis of a constant voltage V_{LL} is made. According to the results obtained by the simulation of the model with shunt reactors, this variable fluctuates around the rated voltage. This behavior could be explained by the fact that shunt reactors are designed to match a voltage close to the rated one, at rated P_G. Below this power, the reactive power is unbalanced at both ends, which could result in higher voltages. At $P_G = 2.1GW$, the reactive power is balanced, and it can be noticed that variables in Figure 4.2 are identical to the one in the Scenario 3 in Table 4.2.

Although there is a difference between voltages obtained by the computed analytical model and simulated one, AC losses can be considered as well estimated by the analytical model, which was expected. Now, these AC losses can be compared to DC losses using the DC losses model in Eq. (3.27). This comparison is shown in Figure 4.3, where the same green curve as in Figure 4.2 is compared to DC losses obtained by the DC losses analytical model, and obtained by the simulation of the bipolar transmission link model in Figure 3.20.

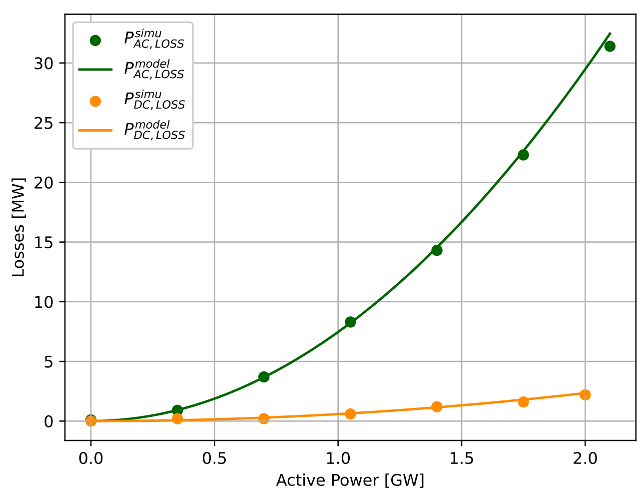

Figure 4.3: Comparison of P^{AC}_{LOSS} and P^{DC}_{LOSS} obtained by the manually computed analytical models of AC and DC losses (Eqs. (3.4), (3.6) and (3.27)) (referenced as "model") and obtained by the simulation of the DC bipolar transmission link (Figure 3.20) and of the AC transmission link (Figure 3.2) (referenced as "simu").

Based on this figure, it can also be concluded that the DC losses model provides results similar to the one obtained by simulation. Furthermore, as suggested by the losses model in Figure 3.22, DC losses are more than ten times smaller than the AC ones: the controller strategy is therefore effective and justified.

It must be pointed out that converter losses are neglected in the DC losses model. A first improvement would be to estimate the current flowing in the phase resistance R in the VSC model in Figure 3.10. To go further, arm resistances of the MMC could have also been considered. Nevertheless, estimated DC active losses are quite similar to the ones obtained by simulation - which takes into account these converter losses. In light of this, it can still be concluded that the DC transmission link generates less active power than the AC one, considering a length of $45km$.

Figure 4.4 shows the steady-state results of the controller. As the active power generated is increased, the AC link instantaneously carries the additional power at first. The controller measures the two voltages and the transmission angle, computes active losses, then updates P_{DC}^{*}. This steady-state comparison shows very close results between the ones obtained via losses models and the ones obtained via the software. In Section 3.3, active power losses, at $P_T = 3.5GW$, were estimated at $19.01MW$ with analytical models. At the same power, the simulation outputs active power losses of $18.78MW$, which is very close.

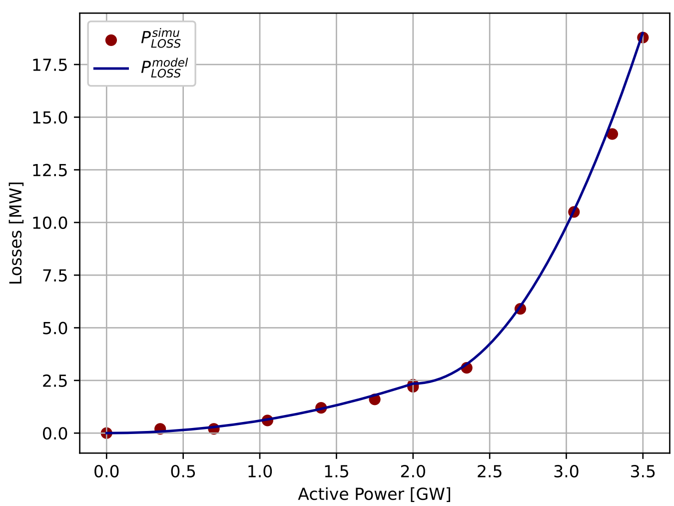

Figure 4.4: Comparison of the total active power losses between results obtained by manually computed analytical models of AC and DC losses (Eqs. (3.4), (3.6) and (3.27)) (referenced as “model”) and obtained by the simulation of the DC bipolar transmission link (Figure 3.20) and of the AC transmission link (Figure 3.2) (referenced as “simu”) using the active power dispatch controller.

At the end, these maximum active power losses represent a loss of 0.54% of the total transmitted active power, in steady state. The slow dynamic of the controller is such that the AC link is temporarily used after a rise or decrease of produced power, which affects the active power losses.

The validation of the strategy of this active power dispatch controller answers the last part of the research question, related to the dynamic repartition of the active power in the hybrid link.

4.3 Simple Wind Turbine Model Assessment

In Section 2.5.2, a reduced model of a wind turbine is introduced. This model can be used for steady-state simulations, in which the wind turbine dynamics are not considered.

This section aims to compare the output power of this model to the characteristic curve of a *Vestas V164 8MW*: this wind turbine model is chosen for its publicly available parameters. The only parameter that is estimated is the moment of inertia of the rotor: it was obtained by a previous work on this wind turbine model [72, 73]. Parameters used for the steady-state comparison are gathered in Table 4.3. As a reminder, the wind filter time constant is chosen such that wind variations higher than $10Hz$ are neglected, which corresponds to $\tau > 0.1s$.

Parameter	Description	Value	Units
τ	Wind filter time constant	1	$[s]$
P_{rated}	Wind turbine rated power	8	$[MW]$
$c_{p,max}$	Maximal performance coefficient	0.44	$[/]$
R	Turbine radius	82	$[m]$
J	Total moment of inertia (blades, hub and rotor of generator)	$37.4\ 10^6$	$[kg.m^2]$
H	Inertia time constant	2.83	$[s]$
ω_{min}	Minimum rotational speed	4.8	$[rpm]$
ω_{max}	Maximal rotational speed	12.1	$[rpm]$
ω_B	Nominal rotational speed	10.5	$[rpm]$

Table 4.3: Parameters used in the simplified wind turbine model.

Figure 4.5 depicts the comparison of the steady-state active power output obtained with the simplified wind turbine model in Figure 2.15 and the expected output power of the *Vestas V164*. The transfer functions of the simplified model are implemented and simulated in the *MATLAB Simulink* software.

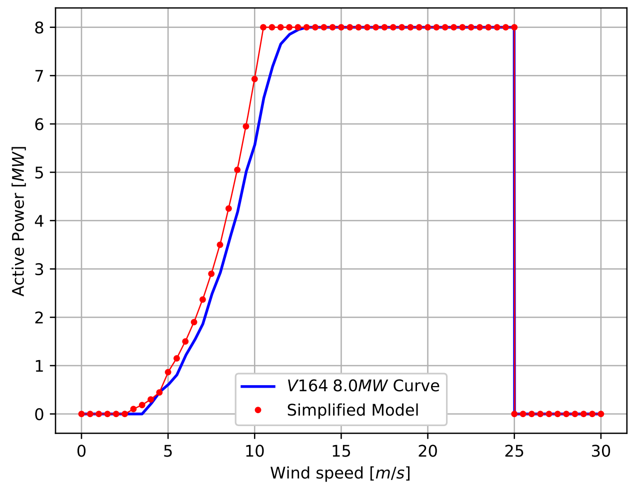

Figure 4.5: Comparison of the active power produced in function of wind speed between the *Vestas V164* and the simplified model, simulated in *MATLAB Simulink*. Adapted from [73].

Characteristic curves are nearly the same. The greatest error between the model and the expected curve is located in the range of 7 to $12m/s$, where the performance coefficient is supposed to decrease in the model, but it is kept at its maximum. Due to this performance coefficient, the rated power is reached at $10.5m/s$ instead of $13m/s$.

Also, the cut-in wind speed should be $3.5m/s$. In the simplified model, this speed is $2.5m/s$: since the minimum rotational speed of the model is the same as the one of the *Vestas V164*, this observation can also be explained by the fact that the performance coefficient is supposed to increase from zero, at the cut-in wind speed, whereas it is already at its maximum when the wind speed is $0m/s$. As a result, the wind turbine starts to generate power at a smaller wind speed than the real one.

Even if results obtained by the model differs a bit from the exact power characteristic curve, this fast-computed model can still provide an acceptable steady-state output power.

4.4 Summary

The goal of this chapter is to assess the analytical AC and DC transmission link models through their power equations, to test the effect of different scenarios using shunt reactors, to validate the strategy of the active power dispatch controller, and to evaluate the accuracy of the simplified model of the wind turbine, through comparisons of results obtained via these models - developed in Chapter 3 - and via simulations of these models, using *DIgSILENT PowerFactory* and *MATLAB Simulink*.

Generally speaking, cable models generate accurate active and reactive powers, based on the knowledge of voltages at cable ends and on the transmission angle. It is shown that the value of the transmission angle must be precisely known so that the model outputs accurate results.

Among the three scenarios of reactive power compensation tested, the one that provides a tradeoff between small current and low voltages is the 50/50 repartition. It is shown that compensating all the reactive power at the node where it is generated leads to the worse scenario in terms of voltage level. Conversely, compensating all the reactive power generated at the node having the initial highest voltage does lead to small voltages, but increases the cable current: the only scenario in which both voltages remains low and the cable current stays below the rated one is the equal repartition of the reactive power to be compensated, at both cable ends.

The strategy of the dispatch controller is validated by active power losses comparisons: both AC and DC losses obtained by the model are confirmed by the simulation. Through measurements of AC voltages at cable ends and of the transmission angle, power converters can adapt the power sent onto HVDC cables. Once these cables are fully loaded, AC export cables carry the rest of the power produced by the wind farm.

A steady-state comparison of the active power generated by the simplified wind turbine model is done, with the characteristic power curve of an existing wind turbine: it can be noticed that the approximation of a constant, maximum performance coefficient leads to cut-in and rated wind speeds smaller than the exact ones. The generated power is slightly higher than the exact one: this model can thus be used to achieve a fast estimation of the steady-state, rough, electrical output power of a wind turbine and, to some extent, of a wind farm.

Chapter 5

Conclusions and Outlooks

Recent political plans regarding the need of renewable energy production led to the development of a new wind farm in the Belgian part of the North Sea. To this end, *Elia* designed a second modular offshore grid, integrating an energy island. This grid has the ability of exporting electricity both in AC and DC. Among all the field of study brought by this future grid, this thesis focuses on the way the power produced by wind turbines is exported by cables to the Belgian grid. Four challenges linked to this topic are raised.

The first one is the study of the maximum active power transmissible in an AC cable. It has been shown that this limitation comes from the active power losses that rise along with the length of the cable. These losses are explained both by the skin effect - the reduction of the effective cross-section of a conductor that increases the series resistance of a line - and by the capacitive effect. The latter is caused by the presence of capacitances in the cable: since the voltage, at one cable end, increases with the cable length - due to the increasing series impedance -, capacitive currents increase as well. It can be shown, in a phasor diagram, that this capacitive current increases the magnitude of the line current. Since both the line current and the resistance increase, active power losses are more important: this explains the reason why, after a certain distance, the entire power exported is dissipated in heat, such that no power can be received from a cable. In the specific case of the MOG II, the cable length is $45km$: this distance is small enough such that the active power received ($3481MW$) is still very close to the one exported at the offshore side ($3500MW$).

The second challenge is linked to a solution to the growing capacitive currents of a cable. This solution consists in the use of reactive power compensators, through shunt reactors. The idea is to place inductances in parallel to capacitances such that the capacitive effect is mitigated. In practice, it has been shown that shunt reactors are able to consume almost all reactive power produced by capacitances of a cable. Three scenarios of shunt reactors are tested: the total reactive power to be compensated is consumed either at the onshore busbar, or at the offshore busbar, or consumed equally at both cable ends. It has been proved that the configuration, leading to a tradeoff between a small voltage increase and a line current bellow the rated one, is the equal reactive power compensation. In that scenario, the phase-to-ground inductance is $2.26H$.

One objective brought by the hybrid link is the comparison of active power losses between the $45km$ AC and DC transmission links. To this end, two analytical models of AC and DC active power losses are developed, based on AC and DC transmission link models. By testing them both, it has been found that, under respective active powers of $2.0GW$ for DC and $2.1GW$ for AC, the DC link model lead to active power losses more than ten times smaller ($2.33MW$) than the ones obtained by the AC link model ($32.4MW$). These estimated losses are confirmed by the simulation of the same AC and DC transmission link models. In light of this observation, an active power dispatch controller is developed: its role is to detect variations of the generated power and to load the DC link in priority. It has been pointed out that power could flow from the onshore side to the offshore side when the produced power suddenly drops, generating additional losses. If the range of time of this controller is small enough, this event only last a few seconds. At the end, thanks to the dispatch controller, the total active power losses reach $18.78MW$ when exporting $3.5GW$, which is very close to the $19.01MW$ expected from the analytical model: this represents a loss of 0.54%.

The last objective sought is the assessment of the modular offshore grid robustness. The idea is to evaluate the $N-1$ criterion, which certifies that a grid with N elements is able to re-route the power flow in case of one network element is out of service, due to a fault or a maintenance. The analysis of several fault scenarios on the AC part of the grid showed that, under rated power, transformers could be overloaded up to 132%, which cannot be withstood. On the DC side, a failure on a HVDC cable or a power converter inevitably leads to a power outage of $400MW$ if AC cables cannot be overloaded. The occurrence of a power outage due to a fault on a DC element has been estimated to once every three years. A way to fulfill the $N-1$ criterion is to add another $2GW$ HVDC transmission link, which is planned by *Elia*. In this configuration, no power outage would be experienced in case of a fault on any of the N elements.

In addition to the challenges addressed in this work, future research questions linked to the dynamic of the grid could be covered. Regarding the use of the dispatch controller, the impact of frequent variations of the produced power P_G on the MOG II could be analyzed. In terms of balance between demand and production and of ancillary services, controllable loads or generators - such as electrolyzers for hydrogen production, hydro-pneumatic energy storage [74] or batteries - could be studied to analyze the impact on the grid frequency. From a power quality perspective, cable models could be completed by other pi-sections and power converter models could be enhanced to take into account the generation of harmonics, and solutions to mitigate those harmonics could be found. Finally, power exchanges between countries - through the future DC interconnections - could be analyzed, along with power generation forecasts, to estimate the need of energy storage.

Appendix A

Voltage Source Converter Controller with Grid-Forming Capabilities

A VSC in "standalone" mode (grid forming) is depicted in Figure A.1 [75]. Its associated voltage controller is shown in Figure A.2.

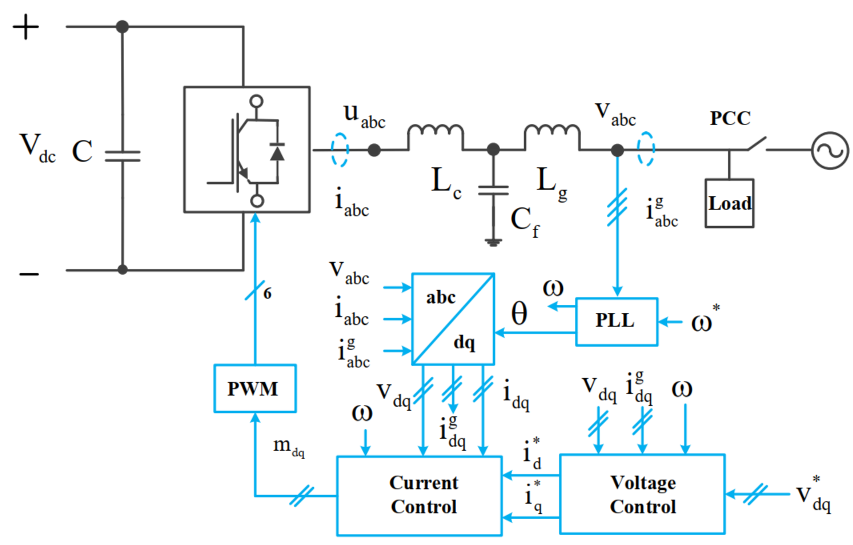

Figure A.1: Schematic diagram of a voltage controller of a VSC in grid-forming mode. Reproduced from [75].

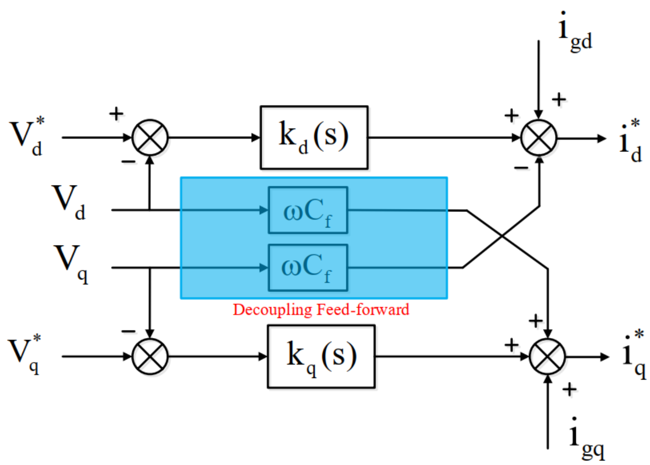

Figure A.2: Inner structure of the voltage controller of a VSC. Reproduced from [75].

Appendix B

Approximation of the Transmission Angle Based on Grid Variables

In the active and reactive power equations (3.4) and (3.6) obtained from the pi-section model in Figure 3.3, the transmission angle δ appears. In order to use this model and to estimate active and reactive power in function of the voltages at cable ends (V_G and V_L, a function $\delta(V_G, V_L)$ needs to be found.

As mentioned earlier, in the model, the assumption of a constant, rated voltage V_L is made, as it is directly set by the external grid, through a transformer: $V_L = 220kV/\sqrt{3} = 127.02kV$.

In Figure B.1, the blue dots represent the V_G voltage variation along with δ obtained by simulation, when increasing the transmitted power on the six $220kV$ cables, from zero to rated power. Shunt reactors with a 50/50 repartition are also connected to the two end-line busbars (see Section 4.1). A linear relation between V_G and δ can be deduced: the function $\delta(V_G)$ is a first order polynomial.

A voltage offset can be noticed: at zero power transmitted, $V_G = 127.53kV$, which is greater than its expected value ($127.02kV$): this might be caused by the quadrature currents flowing in the cable, due to its capacitances, that generates a voltage drop across the complex line impedance. In Eqns. (3.4), if $\delta = 0$, the only solution to $P_G = 0$ is $V_G = V_L$: the linear function is therefore translated so as to match the model.

At the end, the transmission angle is obtained as

$$\delta(V_G) = aV_G + b, \tag{B.1}$$

where $a = 1.58\ ^\circ/V$ and $b = -202.30^\circ$. The resulting characteristic is represented in red in Figure B.1.

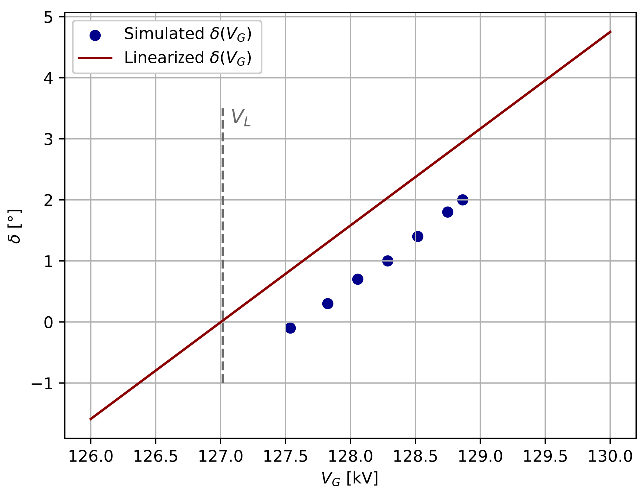

Figure B.1: Transmission angle δ in function of V_G obtained from the simulation of the AC transmission link (in blue) and obtained from the linearized results of the simulation (in red).

Appendix C

Estimation of the Wind Speed Distribution

The Weibull curve, written as

$$f(v_w, k, \lambda) = \frac{k}{\lambda}\left(\frac{v_w}{\lambda}\right)^{k-1} e^{-(\frac{v_w}{\lambda})^k} \text{ for } v_w \geq 0 \text{ and } \lambda > 0, \tag{C.1}$$

is a probability density function used to describe the probability of wind speeds. It contains two parameters: the shape parameter k and the scale parameter λ.

The Netherland Organization for Applied Scientific research [76] made measurements on their Europlatform, located $50km$ away from the Netherland coast, and $70km$ away from the Princess Elisabeth Island (see Figure C.1). Wind speeds were measured between 2016 and 2022, with intervals of 10 minutes and heights between $63m$ and $291m$.

Under the assumption of a height of $166m$ for a $15MW$ wind turbine [77], the report computed the two parameters of the Weibull distribution: $k = 2.025$ and $\lambda = 11.083m/s$. Figure C.2 shows the distribution with these parameters. A power outage occurs if the total active power is greater than $3.1GW$ over $3.5GW$, which means a produced power between 88.6% and 100% of the rated power of a wind turbine. Considering that the wind speed - at which the produced power is 88.6% of the rated power - is $12m/s$, and setting a cut-out wind speed of $25m/s$, the obtained probability of generating 88.6% to 100% of the rated power is 30.3%.

This probability is used as an approximation for the case of the Princess Elisabeth Island wind farm: although it is not the exact distribution - since it is not the same location -, it gives an order of magnitude used to compute the probability of experiencing the studied power outage that disproves the $N-1$ criterion, in Section 3.4.2.

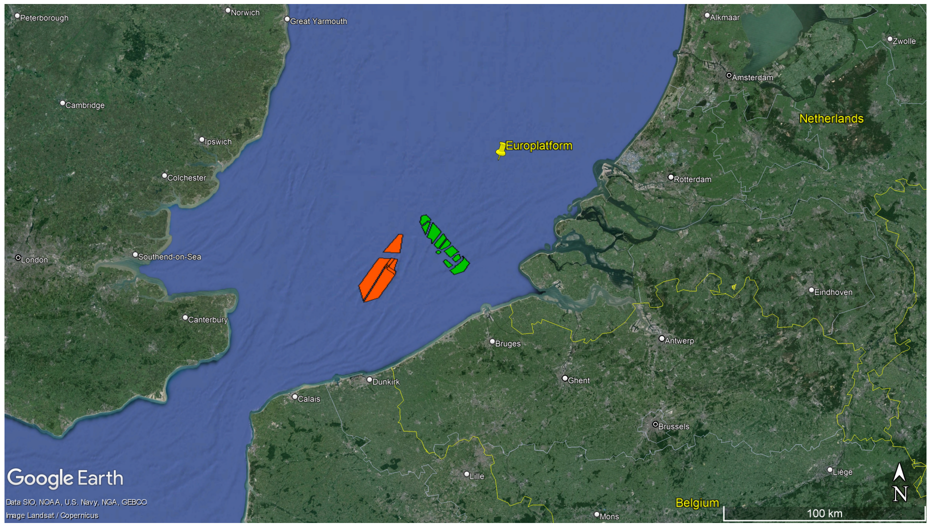

Figure C.1: Relative position of the MOG I (in green), the MOG II (in orange) and the Europlatform (yellow pin) in the North Sea.

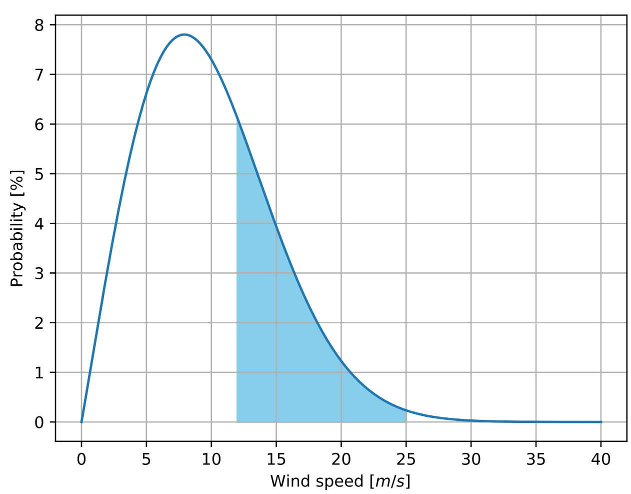

Figure C.2: Weibull distribution for $k = 2.025$ and $\lambda = 11.083$, at a height of $166m$. The blue area highlights the zone where a wind turbine produces between 88.6% and 100% of its rated power.

References

[1] United Nations Framework Convention on Climate Change. *Accord de Paris*. Accessed: 2024-06-06. 2015. URL: https://unfccc.int/sites/default/files/french_paris_agreement.pdf.

[2] Wikipedia contributors. *European Green Deal — Wikipedia, The Free Encyclopedia*. [Online; accessed 6-June-2024]. 2024. URL: https://en.wikipedia.org/w/index.php?title=European_Green_Deal&oldid=1225267014.

[3] Valérie Daloze. "Presentation of the Princess Elisabeth Island". In: Elia - CIGRE. 6/10/2023.

[4] Wikipedia contributors. *War of the currents — Wikipedia, The Free Encyclopedia*. [Online; accessed 1-June-2024]. 2024. URL: https://en.wikipedia.org/w/index.php?title=War_of_the_currents&oldid=1224611098.

[5] Emmanuel De Jaeger. *LELEC2753 - Electrical Power Systems: Advanced topics & Smart Grids*. Lecture: Flexible AC Transmission Systems. Mar. 2023.

[6] Gil Galand and Duc Huy Nguyen. "Impact of HVDC interconnectors on the transient stability performance of power systems". PhD thesis. UCL - Ecole polytechnique de Louvain, 2022. URL: http://hdl.handle.net/2078.1/thesis:35583.

[7] Wind Energy Ireland. *Building the European SuperGrid - Breakthroughs in Technology and Grid Design*. Tech. rep. Accessed: 2024-06-01. Wind Energy Ireland, Mar. 2023. URL: https://windenergyireland.com/images/files/building-the-european-supergrid-final-report-march23.pdf.

[8] ENTSO-E. *Offshore Transmission Technology*. Accessed: 2024-06-01. 2011. URL: https://eepublicdownloads.entsoe.eu/clean-documents/pre2015/publications/entsoe/SDC/European_offshore_grid_-_Offshore_Technology_-_FINALversion.pdf.

[9] Wikipedia contributors. *Skin effect — Wikipedia, The Free Encyclopedia*. [Online; accessed 13-August-2024]. 2024. URL: https://en.wikipedia.org/w/index.php?title=Skin_effect&oldid=1238866793.

[10] Epameinondas (Minos) Kontos et al. "Multi-terminal network options for the interconnection of offshore wind farms: A case study between Britain and The Netherlands". In: Dec. 2014, pp. 1222–1227. DOI: 10.1109/EPEPEMC.2014.6980678.

[11] Hualei Wang and Miles Redfern. "The advantages and disadvantages of using HVDC to interconnect AC networks". In: (Oct. 2010), pp. 1–5.
[12] Elia. *MODULAR OFFSHORE GRID Fase 2 : Project voor de uitbreiding van het transmissienet op zee*. Accessed 06-06-2024. Oct. 2021. URL: https://www.elia.be/-/media/project/elia/elia-site/infra-and-projects/projects/energy-island/2023/20230823_proposition-grid-design-mog2.pdf.
[13] Huangqing Xiao et al. "Review of hybrid HVDC systems combining line communicated converter and voltage source converter". In: *International Journal of Electrical Power & Energy Systems* 129 (2021). DOI: https://doi.org/10.1016/j.ijepes.2020.106713. URL: https://www.sciencedirect.com/science/article/pii/S0142061520342587.
[14] Hitachi Energy. *HVDC Light® Back to Back*. Online. Accessed on 02-06-2024. URL: https://www.hitachienergy.com/products-and-solutions/hvdc/back-to-back.
[15] Wikipedia contributors. *McNeill HVDC Back-to-back station — Wikipedia, The Free Encyclopedia*. [Online; accessed 2-June-2024]. 2024. URL: https://en.wikipedia.org/w/index.php?title=McNeill_HVDC_Back-to-back_station&oldid=1198090992.
[16] Elia. *Elia and Amprion launch ALEGrO, the first interconnector between Belgium and Germany*. Press Release. Accessed on 02-06-2024. URL: https://www.elia.be/en/news/press-releases/2020/11/20201109_cp-alegro-inauguration.
[17] V.K. Sood. *HVDC and FACTS Controllers: Applications of Static Converters in Power Systems*. Power Electronics and Power Systems. Springer, 2006. Chap. 1.3. ISBN: 9781402078910.
[18] ENTSO-E. *HVDC Links in System Operations - Technical paper*. Dec. 2019. URL: https://eepublicdownloads.entsoe.eu/clean-documents/SOC%20documents/20191203_HVDC%20links%20in%20system%20operations.pdf.
[19] ENTSO-E. *Line-Commutated Converters - Current Source Converters*. https://www.entsoe.eu/Technopedia/techsheets/line-commutated-converters-current-source-converters. Accessed: 2024-05-31.
[20] Sixing Du et al. *Modular Multilevel Converters: Analysis, Control, and Applications*. Wiley-IEEE Press, 2018. ISBN: 9781119366300. URL: https://ieeexplore.ieee.org/book/8292871.
[21] PÖYRY. *WESTERN HVDC FINAL FUNDING REVIEW - A report to Ofgem*. Apr. 2012. URL: https://afry.com/sites/default/files/2020-11/whvdc_funding_review_0.pdf.
[22] British Power International. *Consultancy support for the NEMO Interconnector - Cost assessment report*. Nov. 2013. URL: https://www.ofgem.gov.uk/sites/default/files/docs/2014/03/bpi_nemo_cost_report.pdf.
[23] ENTSO-E. *Voltage Source Converters*. Accessed: 2024-05-31. URL: https://www.entsoe.eu/Technopedia/techsheets/voltage-source-converters.
[24] Anil Choubey and Rohit Gupta. "VOLTAGE SOURCE CONVERTER BASED HVDC TRANSMISSION". In: *International Journal For Technological Research*

In Engineering 4.1 (Sept. 2016). URL: https://www.academia.edu/33044307/VOLTAGE_SOURCE_CONVERTER_BASED_HVDC_TRANSMISSIO.

[25] Eduardo Prieto-Araujo et al. “Control design of Modular Multilevel Converters in normal and AC fault conditions for HVDC grids”. In: *Electric Power Systems Research* 152 (Nov. 2017), pp. 424–437. DOI: 10.1016/j.epsr.2017.06.020.

[26] Marcus Haeusler. *HVDC Solutions for Integration of the Renewable Energy Resources*. 2017. URL: https://regridintegrationindia.org/wp-content/uploads/sites/3/2017/09/5C_5_GIZ17_081_presentation_Marcus_Haeusler.pdf.

[27] Siemens. *HVDC PLUS - A new approach for new challenges*. Accessed: 2024-06-01. URL: https://www.siemens-energy.com/global/en/home/products-services/product/hvdc-plus.html.

[28] Power Technology. *Nemo Link Interconnector*. Accessed: 2024-06-01. June 2015. URL: https://www.power-technology.com/projects/nemo-link-interconnector/?cf-view.

[29] E. Uhlmann. “Stabilization of an AC link by a parallel DC link”. In: *Direct Current* (Aug. 1964), pp. 89–94.

[30] T. Machida. “Improving Transient Stability of AC System by Joint Usage of DC System”. In: *IEEE Transactions on Power Apparatus and Systems* PAS-85.3 (Mar. 1966), pp. 226–232. ISSN: 0018-9510. DOI: 10.1109/TPAS.1966.291661.

[31] Li Wang, Ching-Huei Lee, and Yung-Shan Wang. “Steady-state stability analysis of a parallel AC-DC power system containing a static VAr compensator”. In: *Proceedings of TENCON ’93. IEEE Region 10 International Conference on Computers, Communications and Automation*. Vol. 5. 1993, 267–270 vol.5. DOI: 10.1109/TENCON.1993.320634.

[32] Urban Axelsson et al. “GOTLAND HVDC LIGHT TRANSMISSION - WORLD’S FIRST COMMERCIAL SMALL SCALE DC TRANSMISSION”. In: (May 1999). URL: http://www.cired.net/publications/cired1999/papers/1/1_4.pdf.

[33] Ana Diez Castro et al. “CO-ORDINATION OF PARALLEL AC-DC SYSTEMS FOR OPTIMUM PERFORMANCE”. In: (Sept. 1999). URL: https://library.e.abb.com/public/a57a352adc30b474c1256fda004c8ca7/powdelco.pdf.

[34] NS ENERGY. *HVDC fifty years on*. Accessed 03-06-2024. 2004. URL: https://www.nsenergybusiness.com/analysis/featurehvdc-fifty-years-on/?cf-view.

[35] J.G. Slootweg and W.L. Kling. “Aggregated modelling of wind parks in power system dynamics simulations”. In: July 2003, 6 pp. Vol.3. ISBN: 0-7803-7967-5. DOI: 10.1109/PTC.2003.1304458.

[36] Kenneth Okedu. *Performance of DFIG and PMSG wind turbines*. Apr. 2023. DOI: 10.1201/9781003350910.

[37] Jeroen Kooning et al. “Digital Twins for Wind Energy Conversion Systems: A Literature Review of Potential Modelling Techniques Focused on Model Fidelity and Computational Load”. In: *Processes* 9 (Dec. 2021). DOI: 10.3390/pr9122224.

[38] *The Wind Power -Manufacturers and turbines - Vestas V164/9500*. [Online; accessed 22-April-2024]. June 2023. URL: https://www.thewindpower.net/turbine_en_1476_mhi-vestas-offshore_v164-9500.php.

[39] P. Kundur, N.J. Balu, and M.G. Lauby. *Power System Stability and Control*. McGraw-Hill Education, 1994. ISBN: 9780070359581.

[40] Mohammad Shahidehpour and Mircea Eremia. "Wind Power Generation". In: *Handbook of Electrical Power System Dynamics*. John Wiley & Sons, Ltd, 2013. Chap. 4, pp. 179–228. ISBN: 9781118516072. DOI: https://doi.org/10.1002/9781118516072.ch4.

[41] Anca Daniela Hansen and Ioannis D. Margaris. *Type IV Wind Turbine Model*. English. Denmark: DTU Wind Energy, 2014. URL: https://orbit.dtu.dk/en/publications/type-iv-wind-turbine-model.

[42] Emmanuel De Jaeger. "LELEC2520 - Electrical Power Systems - Lecture 5 : Transmission and Distribution Power Lines". Accessed 12-10-2021.

[43] Emmanuel De Jaeger. *LELEC2595 - Electrical power systems dynamics and quality of supply, Lecture CM2 - Unbalance (v2021-2022)*. Lecture date: 1st February 2022. Feb. 2022.

[44] DIgSILENT GmbH. *Technical Reference - Filter/Shunt (ElmShn)*. Jan. 2023.

[45] ABB. *XLPE Submarine Cable Systems Attachment to XLPE Land Cable Systems - User's Guide*. [Online; accessed 13-May-2024]. URL: https://new.abb.com/docs/default-source/ewea-doc/xlpe-submarine-cable-systems-2gm5007.pdf.

[46] Elia. "Task Force MOG 2". In: 24/06/2022. URL: https://www.elia.be/-/media/project/elia/elia-site/users-group/ug/workshop/2022/20220624/20220624_tf_mog_ii_presentation_en.pdf.

[47] Anne THYSSEN. *Wind power plants internal distribution system and grid connection A technical and economical comparison between a 33 kV and a 66 kV*. July 2015. URL: https://orbit.dtu.dk/files/138710206/Thesis_Anne_Thyssen_final_and_revised.pdf.

[48] CBI electric african cables. *HV XPLE Cable Data Sheet - Copper 66kV*. [Online; accessed 20-May-2024]. URL: https://www.africancables.com/cmsb/uploads/products/technical-documents/66kv-copper-xlpe-csa-pe-hs-cables.pdf.

[49] N. Barberis Negra, J. Todorovic, and T. Ackermann. "Loss evaluation of HVAC and HVDC transmission solutions for large offshore wind farms". In: *Electric Power Systems Research* 76.11 (2006), pp. 916–927. URL: https://www.sciencedirect.com/science/article/pii/S0378779605002609.

[50] Stijn Cole. *Steady-State and Dynamic Modelling of VSC HVDC Systems for Power System Simulation.* 2010-09-22. URL: http://lirias.kuleuven.be/1730815.

[51] Tatjana Kalitjuka. "Control of Voltage Source Converters for Power System Applications". Chapter 3. MA thesis. Norwegian University of Science and Technology, Department of Electric Power Engineering, 2011. URL: https://ntnuopen.ntnu.no/ntnu-xmlui/handle/11250/257163.

[52] Dalia Rabie et al. "Study and analysis of voltage source converter control stability for HVDC system using different control techniques". In: *Ain Shams Engineering Journal* 12.3 (2021), pp. 2763–2779. URL: https://www.sciencedirect.com/science/article/pii/S2090447921000927.

[53] Shaista Parveen et al. "The Possibility of Enhanced Power Transfer in a Multi-Terminal Power System through Simultaneous AC–DC Power Transmission". In: *Electronics* 11.1 (2022). DOI: 10.3390/electronics11010108. URL: https://www.mdpi.com/2079-9292/11/1/108.

[54] Georgios Stamatiou. "Converter interactions in VSC-based HVDC systems". PhD thesis. May 2015. URL: https://core.ac.uk/download/pdf/70611772.pdf.

[55] Mohamed M. Z. Moustafa and S. Filizadeh. "A VSC-HVDC model with reduced computational intensity". In: *2012 IEEE Power and Energy Society General Meeting*. 2012, pp. 1–6. DOI: 10.1109/PESGM.2012.6345135.

[56] Prysmian Group. *525 kV HVDC NEW CABLE SYSTEMS FOR THE ENERGY TRANSITION*. [Online; accessed 17-May-2024]. URL: https://www.prysmian.com/staticres/525-kV-HVDC/index.html.

[57] INSIGHT Prysmian Magazine. *The role of 525 kV in the energy transition*. [Online; accessed 17-May-2024]. URL: https://www.prysmian.com/en/insight/projects/integrated-525-kv-solutions-to-enable-the-energy-transition.

[58] ENTSO-E (formerly UCTE). *Glossary*. Consulted: 30-05-2024. June 2004. URL: https://eepublicdownloads.entsoe.eu/clean-documents/pre2015/publications/entsoe/Operation_Handbook/glossary_v22.pdf.

[59] Schneider Electric. *DIFFERENCE BETWEEN CIRCUIT BREAKER AND ISOLATOR / DISCONNECTOR*. Accessed: 2024-05-28. 2024. URL: https://eshop.se.com/in/blog/post/difference-between-circuit-breaker-and-isolator-disconnector.html.

[60] Wikipedia contributors. *Sulfur hexafluoride circuit breaker — Wikipedia, The Free Encyclopedia*. https://en.wikipedia.org/w/index.php?title=Sulfur_hexafluoride_circuit_breaker&oldid=1195846649. [Online; accessed 29-May-2024]. 2024.

[61] Siemens Energy. *Bringing Zero closer: Gas-insulated switchgear and busduct*. Online. Accessed on 02-06-2024. URL: https://www.siemens-energy.com/global/en/home/products-services/product-offerings/gas-insulated-switchgear.html.

[62] Aslam Qureshi. *Various Busbar Schemes in Electrical Grid Stations*. Accessed: 2024-05-29. July 2023. URL: https://www.gridstationhub.com/2023/07/Various-Busbar-Schemes-in-Electrical-Grid-Stations.html.

[63] Tomas Impens et al. *Modular Offshore Grid 2 - Technical Workshop Windfarms*. Consulted: 21-11-23. Sept. 2022. URL: https://www.elia.be/-/media/project/elia/elia-site/users-group/ug/workshop/2022/20220916/20220916_ad-hoc_technical-workshop_mog_2.pdf.

[64] Bruno Dehez. *LELEC1310 - Convertisseurs électromécaniques : Transformateurs Monophasés*. Feb. 2021.

[65] Sinclair Knight Merz. *Calculating Target Availability Figures for HVDC Interconnectors*. Tech. rep. Accessed on 2024-05-31. Sinclair Knight Merz, 2012. URL: https://www.ofgem.gov.uk/sites/default/files/docs/2013/03/skm-report---calculating-target-availability-figures-for-hvdc-interconnectors_0.pdf.

[66] Henk Polinder et al. "Trends in Wind Turbine Generator Systems". In: *IEEE Journal of Emerging and Selected Topics in Power Electronics* 1.3 (2013), pp. 174–185. DOI: 10.1109/JESTPE.2013.2280428.

[67] Nityanand and Ashok Kumar Pandey. "Electrical Engineering Aspects and Future Trends for PMSG Turbines and Power Converters: A Present Market Survey". In: *2018 International Conference on Power Energy, Environment and Intelligent Control (PEEIC)*. 2018, pp. 683–688. DOI: 10.1109/PEEIC.2018.8665427.

[68] *Belgian Offshore Platform*. Accessed: 2024-07-10. URL: https://www.belgianoffshoreplatform.be/en/projects.

[69] Industry & Energy. *GE Installs First Saint-Nazaire Offshore Wind Turbine in France*. Accessed: 2024-07-10. Apr. 2022. URL: https://www.industryandenergy.eu/renewables/ge-installs-first-saint-nazaire-offshore-wind-turbine-in-france/.

[70] DIgSILENT PowerFactory. *Application Example: Wind Farm - Park Controller Simulation*. 2023.

[71] RWE. *Gwynt y Môr Offshore Wind Farm - Construction Activities*. Tech. rep. [Online; accessed 28-April-2024]. 2012. URL: https://www.awjmarine.co.uk/wp-content/uploads/2012/03/Gwynt_y_Mor_OWF_LRes.pdf.

[72] Cian Desmond et al. "Description of an 8 MW reference wind turbine". In: *Journal of Physics: Conference Series* 753.9 (Sept. 2016), p. 092013. DOI: 10.1088/1742-6596/753/9/092013. URL: https://dx.doi.org/10.1088/1742-6596/753/9/092013.

[73] Vestas. *Offshore V164-8.0 MW®/V112-3.3 MW™*. PDF Catalog. 2013. URL: https://pdf.archiexpo.com/pdf/vestas/offshore-v164-80-mw-v112-33-mw/88087-243525.html.

[74] Pieter Jan Jordaens. *Stockage de l'énergie éolienne offshore dans un réservoir sous-marin*. Accessed: 26/07/2024. 2024. URL: https://www.sirris.be/fr/inspiration/stockage-de-lenergie-eolienne-offshore-dans-un-reservoir-sous-marin (visited on 07/26/2024).

[75] Yang Wu. "Control Strategy in Parallel AC-DC Re-configurable Links System". MA thesis. Delft University of Technology, Aug. 2022. URL: http://resolver.tudelft.nl/uuid:60e57237-f840-4b17-8be0-26e789f52f0a.

[76] J. A. Vitulli et al. *Offshore wind energy deployment in the North Sea by 2030: long-term measurement campaign*. Tech. rep. Accessed 31/05/2024. TNO, June 2023. URL: https://repository.tno.nl/SingleDoc?docId=55850.

[77] NREL and IEA WIND. *Definition of the IEA 15-Megawatt Offshore Reference Wind Turbine*. Tech. rep. Accessed: 2024-06-12. National Renewable Energy Laboratory (NREL), Mar. 2020. URL: https://www.nrel.gov/docs/fy20osti/75698.pdf.

UNIVERSITÉ CATHOLIQUE DE LOUVAIN
École polytechnique de Louvain
Rue Archimède, 1 bte L6.11.01, 1348 Louvain-la-Neuve, Belgique | **www.uclouvain.be/epl**